

Background and motivation

Advances in electron sources technology potentially have a profound impact on a whole range of applications, extending from flat panel displays to telecommunications and electric-propulsion systems for spacecraft. Presently, the most widely employed electron source is the “bulky” thermionic cathode which is used in television cathode-ray tubes and high power microwave amplifiers. In our never ending quest for miniaturization, recent requirements for electron sources in applications such as flat panel displays, parallel electron beam microscopy and nanolithography, compact microwave amplifiers and portable X-ray tubes have motivated worldwide research into alternative smaller, more efficient source technologies.

Field emission (FE) electron sources are candidates for such applications. In contrast to the commonly used thermionic emission based on a hot filament, field emission from an unheated “cold” cathode occurs by electron tunneling through a field-thinned barrier at room temperature. It is immediately apparent that a field emitter could be more power efficient than a thermionic emitter which requires heating. In addition, field emission sources also offer several attractive characteristics such as instantaneous response to field variation, resistance to temperature fluctuations and radiation, high degree of focusability in electron optics, good on/off ratio, ballistic transport and a nonlinear current-voltage relationship in which a small change in voltage results in a large change in emission current. Field emission, however, requires a very large local field of a few V/nm to obtain useful currents for applications, so that practical cold cathodes utilize the local field enhancement at the apex of a tip or protrusion and/or a low-work function material to lower the threshold voltage enabling emission.

Serious investigation took off in the late 1960s and early 1970s, when Spindt-type cathodes also known as Spindt-type field-emitter arrays (Spindt FEAs) were

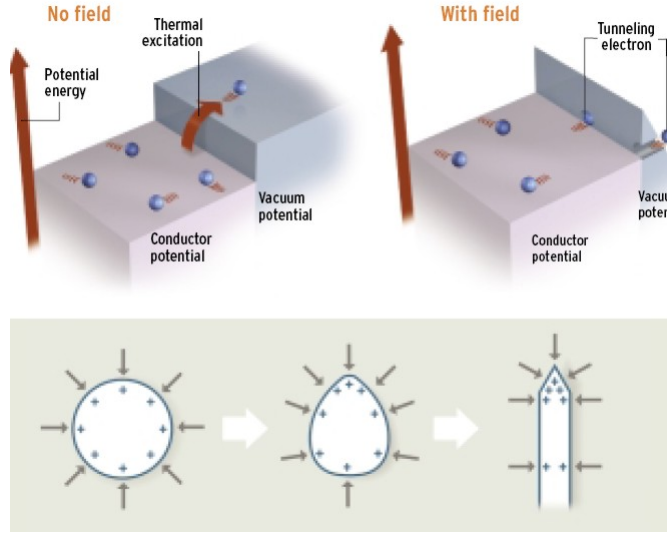


Figure 1: Schematic image illustrating the field emission process (upper figure) and the field enhancement effect of tips (lower figures)

developed [1, 2]. These are basically microfabricated Molybdenum tips in gated configuration. Subsequently, Silicon microtips arrays were fabricated, and silicon vacuum microtriodes were introduced. This development led to the creation of a new area of research called “vacuum microelectronics” [3]. The Mo and Si microtip

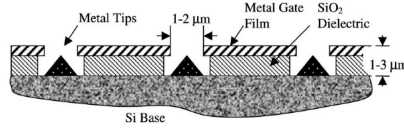


Figure 2: Scheme of Spindt-type field emission arrays (FEAs) in a gated structure

FEAs were then developed for large-area addressable electron emitters, for prototype field emission displays (FEDs). High resolution displays based on this novel technology were being produced by various commercial organizations and demonstrated since the beginning of the 1990s. Although they have not been successfully made to become popular household, research on cold cathode has become a main stream activity in solid state chemistry and physics.

In seeking for an appropriate material, a range of possible candidate materials

have been investigated. Carbon based structures gained at once a leading role: diamond, amorphous carbon, diamond-like carbon films and covered tips have been shown to have electron emission properties and robustness much superior to Mo and Si micro/nanotip arrays [4]. Moreover, the latest members of the ever increasing family of carbon materials -carbon nanotubes- have been welcomed as ideal one-dimensional emitters, owing to their unrivaled aspect ratio. In fact, carbon nanotubes (CNTs) exhibit diameters in the range of nanometers, lengths in the range of microns and strong, covalent bonds among adjacent carbon atoms responsible for their robustness. In the last 15 years, research on field emissions has been mainly focusing on such structures: hundreds papers on the argument testify the worldwide effort in measuring, understanding field emission from CNTs, as well as in the realization of CNT-based, field emission devices.

Last but not least, field emission is a powerful characterizing tool in material science. For example, field ion microscopy has been the first experimental technique enabling us to view metallic surfaces up to the atomic scale. Moreover, the spectrum of the total energy distribution of the emitted electrons gives inestimable information about surface states, adsorbate states, workfunction, electrical resistance etc... Even the simple recording of emitted current versus applied field, when carried out within an accurate measurement methodology, can allow a significant comparison among different samples or kinds of samples.

Anyway, conclusions about the usefulness of new emitters should be based both on practical considerations and emission measurement data. Nowadays, to find a new source is in itself no great advance unless it be less expensive, offers superior performances and/or gave new physical insights.

Many reports about field emission from cathodes of different designs and materials can be found in literature; however, it is difficult to compare data reported by the various authors since their measurements depend upon a variety of different experimental conditions and different definitions of the emission parameters are used. A standardization of field emission measurements has been strongly recommended

Contents

1	Introduction to field emission	9
1.1	Early developments	9
1.2	Deriving Fowler Nordheim law	11
1.2.1	Approximate derivation of transmission coefficient	13
1.2.2	The Fowler Nordheim law	14
1.2.3	Image charge effect	15
1.3	Experimental form of the Fowler-Nordheim law	16
1.4	What can we learn from field emission I-V measurements? (Detailed discussion of the experimental parameters)	18
1.4.1	β enhancement factor	19
1.4.1.1	Theoretical estimation of β for single emitters	19
1.4.1.2	Shielding and screening effects	21
1.4.2	Workfunction	21
1.4.3	Emission area	22
1.4.3.1	Charbonnier-Martin method [36]	24
1.4.3.2	Spindt method [37]	25
1.4.4	Anode-cathode distance	27
1.4.4.1	Approach curve method of Mammana et al. [40]	28
1.5	Field emission energy distribution (FEED)	28
1.6	Field Emission from adsorbates	31
1.6.1	Model of tunnel-resonant emission [41]	31
1.7	Vacuum requirements and cathode stability	32
1.7.1	Vacuum requirement	32
1.7.2	Cathode stability and failure	33

2	Field emission from carbon materials	37
2.1	Carbon nanotubes	38
2.1.1	Carbon nanotube synthesis and characterization	41
2.1.2	Field emission from carbon nanotubes	44
2.1.2.1	Is CNT turn-on field more favorable than that of Spindt-type emitters?	46
2.1.2.2	Are CNTs able to provide stable high currents? Are they metallic emitters?	46
2.1.2.3	Potential for devices and prototypes	50
2.2	Diamond films	52
2.2.1	Properties	52
2.2.2	HFCVD synthesis	53
2.2.3	Electronic structure	54
2.2.4	Field emission	56
3	Experimental: growth of CNT-based materials	61
3.1	HFCVD experimental set-up	61
3.2	Characterization: experimental set-ups	63
3.2.1	Field emission gun scanning electron microscope (FEG-SEM)	63
3.2.2	Raman spectrometer	63
3.2.3	Reflection High Energy Electron diffraction (RHEED)	63
3.3	Carbon nanotube growth	64
3.3.1	Carbon precursors	65
3.3.2	Experimental conditions of HFCVD synthesis of CNT and diamond-covered CNTs	67
3.3.3	CNT growth from different catalyst concentration and dif- ferent solid carbon feedstocks: results and discussion	70
3.3.4	Diamond-covered SWNT bundles	73
3.3.4.1	Material characterization: results	74
3.3.4.2	Proposal of a growth mechanism: discussion	78
3.3.5	Selected area growth	79
3.3.5.1	CNT selected area growth on Fe sputtered films	79
3.3.5.2	CNT selected area growth on a purpose-designed multilayer structure	80
3.3.5.3	Selected area growth of nanodiamond-covered CNTs	81

4	Experimental: field emission I-V characterization	85
4.1	Field emission apparatus at Tor Vergata	85
4.2	Setting up of a reliable measurement methodology	88
4.2.1	Anode-Cathode distance evaluation	88
4.2.2	Emitting area evaluation	92
4.3	Field emission I-V investigation on SWNT-based samples	99
4.3.1	Role of vacuum	99
4.3.2	Role of conditioning process	100
4.3.3	Measurement procedure	105
4.3.4	Morphologically different SWNT samples: results and discussion	106
4.3.5	I-V characterization of diamond-covered SWNT bundles	109
5	Field emission energy distribution from diamond-covered SWNT bundles	113
5.1	Experimental set-up	114
5.2	Preliminaries and experimental conditions	116
5.3	$I(V)$ and $I(t)$ characterization	119
5.4	$i(V, \varepsilon)$ characterization	121
5.5	$i(x, \varepsilon)$ characterization	124
5.6	Conclusions	126
6	Proposal of two SWNT-based field emission devices	131
7	Conclusions	133
8	List of publications	137

Chapter 1

Introduction to field emission

1.1 Early developments

Electron emission from solids can be obtained via:

- photoemission
- thermionic emission
- field emission.

In the first two cases the electrons overcome the surface barrier by absorbing the needed energy in the form of a photon or heat: A. Einstein [5] and O. W. Richardson [6], for photoemission and thermionic emission respectively, supplied the physical insights and mathematical descriptions of the phenomena which earned both of them the Nobel Prize.

Electron emission can occur also by means of tunneling through the barrier: the phenomenon is assisted by an intense electric field, so it is named field emission.

Being observed for the first time at the end of the 19th century, it was in the first decades of the 20th century that field emission attracted the attention of several physicists who tried both to describe experimentally and explain theoretically the phenomenon. In the 20s more than 50 relevant articles concerning cold electron emission from metals were published. Among those it is worth mentioning the

articles by Millikan and Lauritsen [7] who found out the experimental relation between current I and voltage V :

$$I = Ce^{-A/V} \quad (1.1)$$

Contemporarily Schottky [8] made the first attempt to explain that the classical potential barrier would be lowered in the presence of high fields through the electron image force sufficiently to permit conduction electrons to surmount the barrier. Although this effect was verified for thermionic emission at relatively low field (Schottky effect), in the case of field emission it failed to justify the observed relationship between applied field and current density and called for a more rapid increase of emission with temperature at high field than what was measured. No refinement of classical theory proved capable of resolving such difficulties, but the development of wave mechanics opened the way to other points of view.

The efforts in understanding the phenomenon concentrated in 1928 when at least 21 papers concerning field emission appeared. In 1928 G. Gamow [8] applied the new theories of quantum mechanics in explaining the radioactive alpha decay with the tunnel effect; R. J. Oppenheimer [9] suggested that hydrogen in an electric field has a finite probability to be ionized by tunneling and soon after that R. H. Fowler and L. W. Nordheim recognized in field emission another example of barrier penetration [10]. In Fowler Nordheim law the key was finally found and after that any work couldn't do but referring to that paper.

In the same year Nordheim refined the original model by introducing the image potential [11] and many others devoted themselves to studying the effect of temperature maybe wishing to link field emission with thermionic emission [12, 13, 14] (interestingly, Fowler Nordheim law shows the same dependence on field that Richardson equation of thermionic emission show on temperature). It was only in 1956 that thermionic emission and field emission were finally treated from a unified point of view [15] in order to establish the ranges of temperature and field for the two kinds of emission.

Handling of extremely large fields became a possibility with the introduction of the field emission microscope by Muller in 1936 [16] (beside Muller, field emission microscopy was pioneered by Gomer[19], too) and soon with the discovery of field desorption [17], the field range beyond 100 million volts per centimeter, in which all effects of interest here take place, was entered for the first time. The field emission

microscope is simply made up by a tip -the emitter- and an anode consisting of a screen coated with phosphors where the electrons impact forming a pattern: the emission pattern is a kind of magnification of the morphological details of the emitter. The realization that the resolution of the field electron microscope is inextricably limited by the lateral velocity of the electrons led Muller to his successful attempt to image the emitter surface with positive ions of hydrogen rather than electrons: with the field ion microscope [18] atomic resolution was for the first time achieved.

1.2 Deriving Fowler Nordheim law

The formal derivation of the Fowler-Nordheim law is conceptually simple but mathematically tiring. Here, in aiming to explain the physical basis behind the so well known formula, it will be shown how to derive it in an approximate but instructive way.

The physical assumptions behind the theory are:

1. the solid is a free-electron band metal;
2. the electrons are in thermodynamical equilibrium and obey the Fermi Dirac statistics;
3. the surface is atomically flat;
4. the workfunction is field-independent and constant;
5. the temperature is 0 K.

The current density from the surface of the metal when subjected to an external electric field is then expressed by:

$$J = \frac{2e}{m} \int_0^\infty p_x N(p_x) D(E_x) dp_x \quad (1.2)$$

where, $N(p_x)dp_x$ is the number of electrons per unit volume in the range of momentum concerning the direction normal to the surface. $D(E_x)$ is the transmis-

sion probability through the surface potential barrier of the solid subjected to the external electric field.

As shown in Fig. 1.1, the barrier can be simply triangular:

$$V(x) = \Phi + E_F - eFx \quad (1.3)$$

or can, more reasonably, include the contribution of the image charge potential:

$$V(x) = \Phi + E_F - eFx - \frac{1}{4\pi\epsilon_0} \frac{e^2}{4x} \quad (1.4)$$

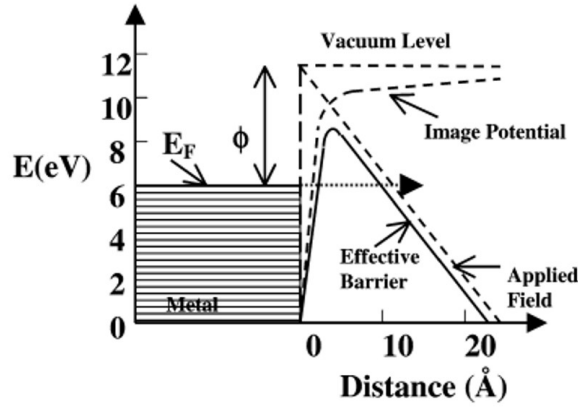


Figure 1.1: Energy levels in field emission

Fowler and Nordheim solved analytically the Schrodinger equation with a simple triangular barrier (eq. 1.4) [10]; soon after that a refined solution which took into account the effect of the image potential was performed by Nordheim [11] and will be reported later.

As for the simple triangular potential profile, Fowler and Nordheim approach consisted in solving the Schrodinger equation for the electrons inside and outside the solid and imposing the continuity of both the wavefunction and its derivative at the surface of the metal. The solutions of the differential equations were obtained by making use of Airy's functions.

Here the alternative and approximated but instructive approach -developed by Gomer [19]- will be followed.

1.2.1 Approximate derivation of transmission coefficient

To begin from the very beginning, in order to derive tunnel probability, one has to solve the time independent Schrodinger equation where $V(x)$ represent the potential barrier

$$-\frac{\hbar^2}{2m} \frac{d^2\Psi(x)}{dx^2} + V(x)\Psi(x) = \varepsilon\Psi(x) \quad (1.5)$$

which can be conveniently rewritten as follows

$$-\frac{\hbar^2}{2m} \frac{d^2\Psi(x)}{dx^2} = \frac{2m(V - \varepsilon)}{\hbar^2} \Psi(x) \quad (1.6)$$

Over distances small enough to make V seem constant (slowly varying potential), the solution $\Psi(x)$ of eq. 1.6 can be well approximated by e^{ikx} where the wave vector k is directly proportional to the momentum p

$$k = p/\hbar = [(\varepsilon - V) 2m/\hbar^2]^{1/2} \quad (1.7)$$

As tunnel theory says, in the barrier region $-E - V < 0$ - the wavefunction becomes a decaying exponential

$$\Psi = \exp \left[- (2m/\hbar^2)^{1/2} (V - \varepsilon)^{1/2} x \right] \quad (1.8)$$

By means of eq.1.8, one can evaluate the value of the wavefunction at the distance l from the beginning of the barrier as

$$\Psi(l) = \Psi(0) \exp \left[- (2m/\hbar^2)^{1/2} \int_0^l (V - \varepsilon)^{1/2} dx \right] \quad (1.9)$$

being $\Psi(l)$ and $\Psi(0)$ the electron wavefunctions at $x = l$ and $x = 0$, where l is the width of the barrier. After eq. 1.9, the tunnel probability can be calculated as

$$D \cong |\Psi(l) / \Psi(0)|^2 \quad (1.10)$$

Substituting eq 1.9, eq. 1.10 results to be

$$D(E) = \exp \left[-2 (2m/\hbar^2)^{1/2} \int_0^l (V - \varepsilon)^{1/2} dx \right] \quad (1.11)$$

Taking the potential barrier expression of eq. 1.3, the integral of eq.1.11 can be

easily solved

$$\int_0^l (V - \varepsilon)^{1/2} dx = \int_0^l (\Phi + \varepsilon_F - eFx - \varepsilon)^{1/2} dx = -\frac{2}{3eF} \left[(\Phi + \varepsilon_F - eFl - \varepsilon)^{3/2} - (\Phi + E_F - \varepsilon)^{3/2} \right] \quad (1.12)$$

and by considering the condition

$$\Phi + E_F - eFl - \varepsilon = 0 \Rightarrow l = \frac{\Phi + E_F - \varepsilon}{eF} \quad (1.13)$$

one obtains

$$D(\varepsilon) = \exp \left[-\frac{4}{3} \left(\frac{2m}{\hbar} \right)^{1/2} (\Phi + E_F - \varepsilon)^{3/2} \right] \quad (1.14)$$

This approximated penetration coefficient differs only in the pre-exponential part by the one analytically derived by Fowler and Nordheim [10]:

$$D(E) = \frac{4 [E(\Phi + \varepsilon_F - \varepsilon)]}{(\Phi + \varepsilon_F)} \exp \left[-\frac{4}{3} \left(\frac{2m}{\hbar} \right)^{1/2} (\Phi + \varepsilon_F - \varepsilon)^{3/2} \right] \quad (1.15)$$

1.2.2 The Fowler Nordheim law

Time has come now for evaluating the initial integral:

$$J = \frac{2e}{m} \int_0^\infty p_x N(p_x) D(\varepsilon_x) dp_x \quad (1.16)$$

which, by substituting eq.1.15, becomes

$$J = \frac{2e}{m} \int_0^\infty p_x N(p_x) \frac{4 [E(\Phi + \varepsilon_F - \varepsilon)]}{(\Phi + \varepsilon_F)} e \left[-\frac{4}{3} \left(\frac{2m}{\hbar} \right)^{1/2} (\Phi + \varepsilon_F - \varepsilon)^{3/2} \right] dp_x \quad (1.17)$$

Now, $N(p_x)dp_x$ can be evaluated by integrating over all allowed values of p_x and p_y

$$N(p_x)dp_x = \frac{2}{h^3} dp_x \int_0^\infty \int_0^\infty \frac{dp_y dp_z}{\exp \left[\left(\frac{1}{2m} (p_x^2 + p_y^2 + p_z^2) - \mu \right) / kT \right] + 1} \quad (1.18)$$

When all integration is complete, the result is the Fowler-Nordheim equation (uncorrected for the image potential) which links current density to electric field F (in V/Å) and workfunction ϕ (in eV)

$$J(F) = 6,2 \cdot 10^6 \frac{(\mu/\phi)^{1/2}}{(\mu + \phi)} F^2 \exp \left[-6,8 \cdot 10^7 \frac{\phi^{3/2}}{F} \right] A/cm^2 \quad (1.19)$$

The strong exponential dependence of current density upon electric field -and therefore upon voltage- confirms the early experimental findings by Millikan and Lauritsen [7], see eq. 1.1.

1.2.3 Image charge effect

The charge cloud at the surface of the solid does not terminate so abruptly as eq. 1.3 would suggest. Since a more realistic description of the potential profile just outside the solid must be taken into account, one usually start with eq. 1.3 and add a classical image term as done in eq. 1.4. The resolution of the corresponding Schrodinger equation shown in eq.1.5 is no more analytical but makes use of the Wentzel-Kramer-Brillouin (WKB) approximation [20]. The result of the calculation, carried out in ref. [21], under the approximation of low (room) temperature, expressed in term of current density, using the same units of measurement of sec.1.2.2, is:

$$J(F) = \frac{1,537 \cdot 10^{10}}{2 \left(\frac{3,79 \cdot F^{1/2}}{\phi} \right)} F^2 \exp \left[-\frac{3/2}{F} v \left(\frac{3,79 \cdot F^{1/2}}{\phi} \right) \right] A/cm^2 \quad (1.20)$$

In the above equation t and v are tabulated functions (known as Nordheim elliptical functions); a sample of their possible values is shown in 1.1 (taken from [21]):

Table 1.1: tabulated values

$y = \frac{3.79 \cdot F^{1/2}}{\phi}$	$v(y)$	$t(y)$
0.00	1.0000	1.0000
0.10	0.9817	1.0036
<i>0.20</i>	<i>0.9370</i>	<i>1.0111</i>
<i>0.30</i>	<i>0.8718</i>	<i>1.0207</i>
0.40	0.7888	1.0319
0.50	0.6900	1.0439
0.60	0.5768	1.0565
0.70	0.4504	1.0697
0.80	0.3317	1.0832
0.90	0.1613	1.0969

y values bigger than 1 are not shown because correspond to unrealistic electron energies higher than the barrier height. Under most of the conditions encountered in practice, y is 0.2-0.35 so that reduction in applied field of the order of 10-20 % results from the image effect. Since both functions are slowly varying with F , it is reasonable to treat them as constant in a given application of the law.

1.3 Experimental form of the Fowler-Nordheim law

Overall, eq. 1.20 and 1.19 show the same strong exponential dependence of current density upon the local electric field which by far overwhelm the pre-exponential factor. As for the numerical evaluable constants in the equations, their values have been known to vary depending on the approximation used for the Nordheim elliptical functions. Moreover, what literature contains is various analyses that lead to various related equations for the magnitude of concretely measured I of the field-emitted current as a function of local work function ϕ and external applied (macroscopic) electric field. They shares the same exponential feature and differ in the pre-exponential term. Forbes [23] recently denounced the lack of a recent, wide-ranging reviews of Fowler Nordheim theory since the work of Gadzuk and Plummer [24] and Modinos [21] and the persistence of errors due also to the use of non-updated values of the universal physical constants. This point will not be deepened in this thesis because too much theoretical in its interest, but some words will be spent in pointing out some “principle” difficulties in applying eq. 1.20 or eq. 1.19 to practical cases.

- First, to get a detectable current from a metal with a workfunction of 3-4 eV, one can easily calculate through eq. 1.20 and 1.19 a needed field of some V/nm. As already said in the “Background and motivation” initial paragraph, this huge value of electric field can be currently achieved only by using tips and protrusions able to concentrate the field lines. A crucial distinction must therefore be made between applied and local field: what is shown in the above equations is always the local field while the known quantity is usually the applied field. Therefore, the field at the apex of the tip is usually written as:

$$F = \beta E \quad (1.21)$$

where the factor β , which reflects the aptitude of the emitter to amplify the applied field E and is accordingly termed the field enhancement (or field amplification) factor, is completely determined by the geometrical shape of the emitter.

- Secondly, the physical measurable quantity in a field emission experiment is a current rather than the current density required by eq. 1.20 and 1.19. Therefore one writes that:

$$I = AJ \quad (1.22)$$

where A has the dimension of an area and represents in first approximation the emitting area.

- Last but not least, the electric field is applied by imposing a potential difference to a couple of counterfacing electrodes. For two perfectly flat, endless metallic electrodes, given V , the voltage difference and d their distance, the electric field is simply obtained by:

$$E = V/d \quad (1.23)$$

but even in the real case the border effects may affect the distribution of the field lines. Moreover, in this flat electrodes configuration, when the planes approach each other to reduce the border effects, no negligible misalignments may occur. This inconvenience has been partially solved by the introduction of spacers made by dielectric material (making it impossible to vary d during the measurement session) or by the use of a sphere to plane electrostatic con-

figuration. In this latter case, a more complex evaluation of the electric field must be carried out to take into account its lateral dispersion. In any case, the precise evaluation of the distance d is essential to estimate the value of the applied field and to process the data through the following equations. When using a spacer, a precise estimation of d can be easily achieved; otherwise, mechanical/electrical contact methods has been commonly used.

Given the difficulties discussed above, the practical form of Fowler-Nordheim law used in this work will be the one proposed by Bonard [25]

$$I \prec (F^2/\Phi) \exp\left(B\Phi^{3/2}/F\right) \quad (1.24)$$

with $B = 6,83 \cdot 10^9 \text{ V} \cdot \text{m}^{-3/2}$.

F is evaluated through eq. 1.23 and eq. 1.21, so that eq. 1.24 becomes

$$I \prec (\beta^2 V^2 / d^2 \Phi) \exp\left(B\Phi^{3/2} d / \beta V\right) \quad (1.25)$$

The linearization of eq. 1.25 is carried out by simply taking $\ln(I/V^2)$ as it is shown below

$$\ln(I/V^2) \prec \left(B\Phi^{3/2} d / \beta\right) (1/V) \quad (1.26)$$

Experimental basic field emission investigations are carried out by simply making I-V measurements and analyzing the obtained data with eq. 1.25 and eq. 1.26 which is called Fowler-Nordheim plot (FN plot).

1.4 What can we learn from field emission I-V measurements? (Detailed discussion of the experimental parameters)

The goal of technological research on field emission is basically the fabrication of a cathode capable of supplying uniformly high current at low voltages for the longest achievable period of time. I-V characterization, therefore, must provide

proofs of such characteristics e.i. obedience to Fowler Nordheim law, turn-on voltage, current density.

Obedience to the Fowler Nordheim law can be roughly checked by plotting $\ln(I/V^2)$ vs. $(1/V)$: if the emitter is metallic (i.e. Fowler Nordheim-type), one should obtain a straight line with a slope $B\Phi^{3/2}d/\beta$. Truly obedience to the proposed model can be investigated more rigorously through the measurement of the energy distribution of the emitted electrons (see sec.).

Sharpening of the tip to enhance β and/or lowering Φ have always been key tasks in searching for efficient emitters. Given eq. 1.25 and eq. 1.26, since d is given by the experimental configuration, the determination of Φ or β can be carried out once known the slope of the straight line, provided that one of the two other parameters is known. As we will see below, it is very difficult to estimate β from the (purported) shape of the emitter (and especially its radius of curvature), so it is usually regarded as the unknown parameter.

As for turn-on voltage and current density, the evaluation of the interelectrode distance d and the emission area A turn out to be essential data to be known with a certain precision.

As a consequence, β , Φ , A , d will be described in details in the following subsections.

1.4.1 β enhancement factor

The β enhancement factor quantifies the aptitude of the emitter to capture field lines, so it relies only upon its geometrical characteristics. The following paragraphs deal with its theoretical evaluation for single emitters and arrays of emitters and will demonstrate why it is generally regarded as an unknown experimental parameter.

1.4.1.1 Theoretical estimation of β for single emitters

Different theoretical studies have been carried out with the purpose of estimating β and of determining which shape is the most effective in concentrating the electric field.

As for the former approach, the most basic approximation for an infinitely long emitter with a radius at the apex r is to design it as a sphere of the same radius. As $F = V/r$, $\beta = d/r$. This approximation is far too drastic to be meaningful and an empirical correction factor k is introduced so that $F = V/(kr)$, or $\beta = d/(kr)$. k is taken usually as $k \approx 5$ for a hemisphere on a cylinder [26]. Even with this correction, the obtained values are of little practical use because, though the model is quite

reliable for single emitters, it has proved to be less adapted for emitters deposited on flat substrates [25].

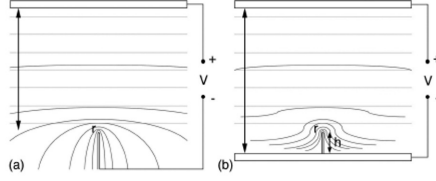


Figure 1.2: Standard plane to plane configuration in field emission measurements: (a) the infinitely long emitter (b) the emitter on a surface.

The models for field enhancement factor of protrusions on flat surfaces have been recently reviewed, and only the most important results will be here presented. Three different configurations have been selected from [27].

The first one is the simplest and corresponds to a hemisphere of radius r on a surface. In that case, $\beta = 3$ and is independent of r and the relative position of the counter electrode, which implies that any protrusion on a surface should produce a field enhancement of at least 3.

The second one is a sphere of radius r floating at a distance L of the planar surface. Its only interest is that it can be resolved semi-analytically, with

$$\beta = 2.5 + L/r \quad (1.27)$$

but is of limited practical use as the values are very .

The third one corresponds most closely to the situation encountered in field emission and it is the hemisphere-on-cylinder model, which cannot be resolved analytically. So far, the most popular formula has been

$$\beta = 3 + h/r \quad (1.28)$$

but its origin (and scientific justification) has proved difficult to assess.

Recent studies based on numerical simulations have challenged this “historical” expression [27]. The most accurate expression to date is the one proposed by Edgcombe and Valdrè [28]:

$$\beta \approx 1, 2(2, 15 + h/r)^{0,9} \quad (1.29)$$

which is valid for $4 < h/r < 3000$. Eq.1.29 does not make any predictions on the influence of the shape or position of the counter electrode.

The above models assume that the counter electrode is flat. This is not the case in most experimental setups, and the measured value is therefore not only due to the emitter, but also to the anode where the field will be greater than V/d .

As for nanotubes, simulations showed that there is a decrease of only 10 % in the field at the tip of the nanotube for an anode of 45° opening angle as compared to a flat one. The shape of the anode does therefore not have a significant influence on the obtained value of β , which comes probably from the fact that the radius of curvature of the nanotube is much smaller than that of the anode.

1.4.1.2 Shielding and screening effects

So far, we have considered only one emitter on a surface. As soon as several emitters are assembled to form an array, influences between the emitters have to be taken into account as electrostatic screening become significant even for large distances between the emitters l . Several studies, both theoretical and experimental, revealed that the electric field at the apex of the emitters will decrease with decreasing spacing. In fact, the effective field amplification drops rapidly for spacings $l < 2h$. This effect influences critically the field emission properties of individual emitters and of arrays of emitters [29, 30, 32]. Other effects have to be taken into account, such as the fact that not all emitters will show the same β when not of the same dimensions: indeed, this distribution of can be estimated by measuring the field emission locally with a sharp tip and has been shown to be exponential for typical array of emitters such as a CNT films [31].

It should be evident, now, that the theoretical evaluation of β enhancement factor is hardly reliable even knowing the geometrical details of the single emitter and quite impossible for an array of emitters.

1.4.2 Workfunction

Workfunction is the energy difference between the Fermi level of a solid and the vacuum level of the surface. Workfunction is a local parameter whose value depends on the kind of material and on the state of the surface. In a crystal, even different crystallographic orientations of the surface lead to different workfunction values [33].

Even if the procedure is rather controversial, workfunction can be independently evaluated by measuring the energy distribution of the field emitted electrons (FEED) [34], field/photoemission spectroscopy or by the use of the Kelvin probe with the aid of a reference material.

As for field emission data processing through the FN plot (eq. 1.26), workfunction -even if it is usually taken as an averaged value among the values of different crystallographic orientations- is a better known parameter than the β enhancement factor and, in eq. 1.25 and eq. 1.26, it is usually treated as the known parameter.

The actual workfunction is about 5 eV for most available materials, like those used in field emission -i.e. refractory metals such as W and Mo- which is rather high. Coverage of W and Mo emitters with low-workfunction materials such as those behaving to alkaline and earth-alkaline metals has been investigated but gave no encouraging results [4].

1.4.3 Emission area

The potential for high emission current densities has always been an attractive feature of field emitter. Since current density cannot be evaluated without an estimation of the emission area, any claim for high current density rely upon the methodology of quoting that parameter.

The basic Fowler-Nordheim equation has been obtained for the local current density J and considers uniform emission from an arbitrary planar area: that one can be therefore called the *theoretical current density*. In practical cases the determination of the emission area to get the *practical current density* has to overcome, first, non negligible difficulties even in the definition of the *emission area* itself.

We can call emission area:

1. the one got by using the intercept of the Fowler-Nordheim equation called here *FN emission area*;
2. the observed area of the emitter tip;
3. the area of the emitter at its base, called here area of the emission site;
4. the area of the entire cathode (in the parallel plane geometry).

As regard the above definitions, the following figure, taken from Zhirnov [35], is illuminating. Note that the total current of $10\mu A$ can result in both very high and

very low current density, depending upon the choice of emission area. However, the question to be answered is: “What will the current be when the anode diameter is increased 2, 10, 20 times?”. If the evaluated value of the emission area does make sense, the current should be respectively 2, 10, 20 times higher.

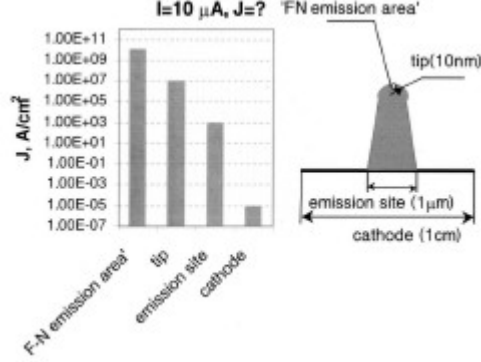


Figure 1.3: Current, current density and emission area. After [35].

Three main different methods for evaluating the *FN emission area* are currently known: two of them will be briefly presented in the following paragraphs. The third one, developed by Forbes [27, 38], involves a numerical and iterative approach and will not be described here.

An alternative approach derived by the macroscopic geometrical features of the anode-cathode system has been cited by Zhu [39]. With a probe ball as anode and a plane as cathode, under the condition $d \ll 2R$ where d is the anode-cathode distance and R the ball radius, the emission area A has been expressed as

$$A = 2\pi R d \left(2^{1/n} - 1 \right) \quad (1.30)$$

where n equals

$$n = \frac{V}{I} \left(\frac{dI}{dV} \right) \quad (1.31)$$

and is approximated to 2. No other details about the basis of the calculation were therein given.

1.4.3.1 Charbonnier-Martin method [36]

The following version of the Fowler-Nordheim equation was considered by Charbonnier and Martin

$$J = a \frac{F^2}{\phi t^2(y)} F^2 \exp \left[-\frac{b\phi^{3/2}}{F} v(y) \right] \quad (1.32)$$

where $t(y)$ and $v(y)$ are the same equations introduced by Nordheim to take into account the image charge effect (see sec. 1.2.3) and the values of the constants a and b are, respectively, $1,541 \cdot 10^{-6} A \cdot eV \cdot V^{-2}$ and $6,831 \cdot 10^9 eV^{-3/2} \cdot V \cdot m^{-1}$. Introducing $F = \beta V$ and $I = A \cdot J$, eq. 1.32 becomes:

$$I = Aa \frac{\beta^2 V^2}{\phi t^2(y)} F^2 \exp \left[-\frac{b\phi^{3/2}}{\beta V} v(y) \right] \quad (1.33)$$

The slope m of the FN plot (see eq. 1.20) can be calculated as follows:

$$m = -\frac{d \left(\ln \frac{I}{V^2} \right)}{d \left(\frac{I}{V} \right)} = \frac{b\Phi^{3/2}}{\beta} \left[v(y) - \frac{y}{2} \frac{d(v(y))}{dy} \right] = \frac{b\Phi^{3/2}}{\beta} [s(y)] \quad (1.34)$$

where $s(y)$ is defined as the quantity in squared brackets. After combining eq. 1.33 and eq. 1.34 and substituting the proper values of the constants, one gets:

$$J = 7,219 \cdot 10^{13} \frac{e^{-m/V}}{(m/V)^2} \Phi^2 \exp \left[-\frac{10,45}{\Phi^{1/2}} \right] = 7,219 \cdot 10^{13} \frac{e^{-m/V}}{(m/V)^2} G(\Phi) \quad (1.35)$$

where the Φ -dependent part on the left is called $G(\Phi)$ on the right. Charbonnier and Martin approximated $G(\Phi)$ to a constant:

$$G(\Phi) = 2700 \pm 200 \text{ for } 4eV < \Phi < 12eV \quad (1.36)$$

so that, after substituting its value, the current density occurs to be:

$$J = 1,992 \cdot 10^{17} \frac{e^{-m/V}}{(m/V)^2} \quad (1.37)$$

and the emission area can be evaluated by the ratio I/J .

To summarize, the method involves the following steps:

- m is evaluated from the slope of the FN plot of the experimental data;
- chosen a value of V_{meas} among the I-V measuring couples, J is calculated from eq. 1.37;
- from the ratio I_{meas}/J the emission area is estimated.

The recommended current density range for the application of the method is $10 < J < 10^4 A/cm^2$.

1.4.3.2 Spindt method [37]

Spindt started from:

$$I = R_V V^2 \exp \left[-\frac{S_V}{V} \right] \quad (1.38)$$

where R_V and S_V are defined by:

$$R_V = \frac{Aa\beta^2}{1,1\Phi} \exp \left[1,44 \cdot 10^{-9} \frac{b}{\Phi^{1/2}} \right] \quad (1.39)$$

$$S_V = \frac{0,95b\Phi^{3/2}}{\beta} \quad (1.40)$$

and a and b have the same values as in eq. 1.32 and eq. 1.33. The Nordheim elliptic functions are quoted as follows:

$$v(y) \cong 0,95 - y^2 \quad (1.41)$$

$$t(y) \cong 1,1 \quad (1.42)$$

$$y = \frac{3,79 \cdot F^{1/2}}{\phi} \quad (1.43)$$

By considering the product

$$R_V S_V^2 \cong 5,96 \cdot 10^{13} A \phi^2 \exp \left[\frac{9,89}{\phi^{1/2}} \right] = 5,96 \cdot 10^{13} A \cdot g(\phi) \quad (1.44)$$

which also defines a function, $g(\phi)$, perfectly corresponding to $G(\phi)$ of eq. 1.35, one notes that the emission area is easily evaluable as

$$^{-14}R_V S_V^2 g(\phi) \quad (1.45)$$

Spindt neglected the dependence of g from Φ and approximated the function to a constant

$$g(\Phi) = 2250 \pm 250 \text{ for } 3,4eV < \Phi < 11,6eV \quad (1.46)$$

obtaining

$$^{-18}R_V S_V^2 m^2 \quad (1.47)$$

Once known how to derive A from S_V and R_V , we need to know how to link the experimental data with these parameters.

Deriving eq. 1.38, one gets

$$\frac{dI}{dV} = \frac{I}{V} \left(2 - \frac{S_V}{V} \right) \quad (1.48)$$

so that

$$\frac{S_V}{V} = 2 - \frac{V}{I} \frac{dI}{dV} \quad (1.49)$$

and, by substituting it into eq. 1.38, R_V is evaluated

$$R_V = \frac{I}{V} \exp \left[\frac{V}{I} \frac{dI}{dV} - 2 \right] \quad (1.50)$$

Therefore, to get to get both R_V and S_V , the measurement of I , V , and dI/dV is required.

To summarize, one practically proceeds as follows:

1. independent measurements of $I(V)$ curve and dI/dV are carried out;
2. R_V and S_V are calculated through eq.1.50 and eq. 1.49 for each point of the $I(V)$ curve;
3. eq. 1.47 can then be applied and the emission area evaluated.

Requiring two independent measurements, this method is more accurate than the Charbonnier one; nevertheless it suffers from the approximation of eq. 1.46 and the need of the experimental measurement of a derivative.

1.4.4 Anode-cathode distance

Compared with the discussion about the other parameters, anode-cathode distance quoting is a more practical problem. What makes it essential for data processing is its role in the electric field evaluation and therefore in the number of claims for low-threshold field emitters.

Many experimental set-ups consisting of two counterfacing plates utilize rigid spacers both to avoid electrode misalignments as much as possible and to eliminate the problem of quoting the distance. In this case the emission area is easily evaluated as the entire cathodic area but, beside introducing border effects in the distribution of field lines, this configuration does not enable

1. scanning of the cathode surface: relying field emission exponentially upon the morphological features of the surface, local investigations can provide interesting insights into the investigated sample
2. varying of anode-cathode distance, which can be useful in case of discharges.

Moreover, the presence of dielectric spacers may cause electrostatic disturbances due to charging and worsening of the vacuum (degassing) eventually leading to discharges.

The second most common set-up makes use of a small probe ball as anode and a planar cathode. Beside introducing some difficulties in electric field - and consequently emission area- evaluation because of the spherical symmetry of the anode, it does enable scanning of the surface and interelectrode distance adjustment with the help of micromanipulators. Within this geometry, in most cases distance is evaluated at the end of the measurement session by a mechanical contact of the electrodes; the touch is confirmed by measuring an electrical short. This methodology introduces modifications/damages to the cathode surface making it impossible to carry out further measurements. Moreover, in such a way the distance can be

easily underestimated because arcing may occur as the electrodes approach; the arc current can be so high to be resistance-limited so as to appear as a short.

1.4.4.1 Approach curve method of Mammana et al. [40]

A non contact-method for the evaluation of the applied electric field has been recently proposed. It is an approach curve method with a truncated cone as anode with its symmetry axis normal to the sample surface (the cathode) and its smaller cap facing the cathode. The anode diameter is typically about one tenth of the cathode size so that several different points can be measured and eventual problems of misalignments minimized.

The goal of the procedure is to get an $I(E)$ curve by making $I(V)$ measurements at different interelectrode distances. The procedure is carried out as follows: at each -unknown- interelectrode distance a certain voltage is required to extract a fixed current; these voltage values are then plotted against a roughly arbitrarily estimated distance producing a $V(d)$ curve. The slope of $V(d)$ is the needed field to produce that amount of current.

The validity of the model must be carefully checked by taking also into account the relative values of sampled distances and the area of the small cap of the truncated cone facing the cathode. In particular, the idealized plane capacitor behavior, developed on the image of two metallic flat electrodes, is expected to break down at large interelectrode distances because the meaning of “large” do depends on the length scale of surface protrusions of the cathode and their spatial distribution.

1.5 Field emission energy distribution (FEED)

The Fowler-Nordheim equation 1.20 gives the total emitted current density as a function of the applied field. It is also useful to consider the repartition of this current as a function of the energy of the emitted electrons

$$J(\varepsilon) = \int_0^\varepsilon N(\varepsilon, W) D(\varepsilon, W) dW \quad (1.51)$$

$N(\varepsilon, W) d\varepsilon dW$ is the number of electrons passing through a unit surface normal to the z direction per unit of time having energy comprised between ε and $\varepsilon + d\varepsilon$ and a z component of energy comprised to W and $W + dW$.

$$N(\varepsilon, W)d\varepsilon dW = \frac{2f(\varepsilon)}{(2\pi)^3} \int \int \int_{(\varepsilon, W)} v_z d^3k \quad (1.52)$$

$f(\varepsilon)$ is the Fermi-Dirac energy distribution and v_z is the electron velocity along the z direction evaluated according to the free-electron model.

$D(\varepsilon, W)$ is the penetration coefficient at the base of the barrier.

The evaluation of the integral is long and tiring, so here it will be given only the result. To follow the entire calculation, the reader is addressed to ref. [21, 24, 19].

The energy distribution of current density extracted from a free- electron metal is

$$J(\varepsilon) = \frac{J_0}{ed_0} \frac{\exp[(\varepsilon - \varepsilon_F)/d_0]}{1 + \exp[(\varepsilon - \varepsilon_F)/pd_0]} \quad (1.53)$$

where ε_F is the Fermi energy, J_0 the current density of the Fowler Nordheim law and

$$p = kT/d_0 \quad (1.54)$$

$$1/d_0 = 2 \left(\frac{2m}{\hbar^2} \right)^{1/2} \frac{\Phi^{1/2}}{eF} t(y_0) \quad (1.55)$$

According to eq. 1.53, the energy distribution of field emitted electrons - $J(\varepsilon)$ - results to be an asymmetric single peak with a maximum centered on the Fermi level.

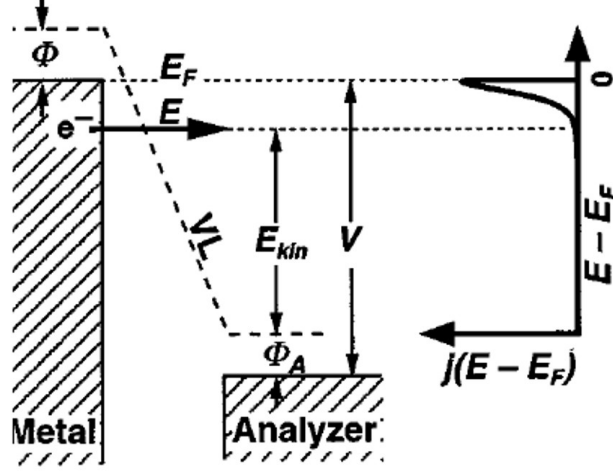


Figure 1.4: Simplified band diagram and theoretical FEED spectrum of a metallic field emitter. A negative voltage V is applied to the emitter with respect to the analyzer. Electrons are emitted from energy levels E below the Fermi-level E_F , which serves as a reference energy in the FEED spectrum. E_{kin} : measured kinetic energy of field-emitted electrons; Φ_A : analyzer work function; Φ : emitter work function; VL: vacuum level. After [96].

Eq. 1.53 has been obtained by considering only the energy region nearby the Fermi energy but the approximation is effective because the emitted electrons do come out only from the vicinity of Fermi level.

It is interesting to note that $J(\varepsilon)$ depend both on local field F and temperature T . The energy distribution is such that if the local field F increases, the peak width increases at the low energy side. This is fully explainable looking at Fig. 1.1: as the field increases, the slope of the barrier gets steeper and the barrier thinner so that electrons in deeper energy levels have a significant probability of tunneling.

If the temperature increases, the peak width also increases but at the high energy side. Again, looking at Fig. 1.1, one can easily realize that, since with temperature the levels higher than the Fermi one get populated, many electrons having higher energy will tunnel the barrier.

The simple free-electron model used to derive eq. 1.53 succeeds to predict FEEDs from most of the systems encountered in practice; however it sometimes fails for a number of reasons e.i. band structure effects, many-body interaction

effects, inadequacy of eq. 1.4 in describing the real potential barrier, occurrence of surface states, adsorbate effects [41].

1.6 Field Emission from adsorbates

The discussions above are based on the free-electron model of a solid, that is from metals.

There is another kind of emission showing drastically different features: it is mainly the emission from molecular adsorbates on metal surfaces. In this case the FEED presents, compared with pure metallic emission, unexpected features (see [42] for a more complete description of the entire phenomenon): it consists of multiple peaks with the following characteristics:

1. the peaks shift linearly with voltage;
2. compared to pure metallic FEED, the peak width increases very few on the low energy side;
3. more peaks can appear at the Fermi level when increasing the applied field;
4. the peak shape cannot be satisfactorily fitted with eq. 1.53;
5. the peaks may be reproducible or may change from time to time.

Moreover, in this kind of emission, the FN plot I-V curve may be roughly linear or present kinks; again, the curve may be reproducible or not. As for current stability as a function of time, current often proves to be very stable in the range of nA; at higher levels of current a degradation of stability is observed.

1.6.1 Model of tunnel-resonant emission [41]

This model has been developed to explain the multiple-peak appearance of some FEEDs due to the emission from adsorbates on metallic tips. According to this model, the molecular adsorbates cause the appearance of localized, discrete energy states behaving like “windows” for emission. These states are responsible for the appearance of the peaks in the FEEDs; they shift linearly with voltage because of the field penetration, thus shifting the corresponding peaks. Moreover, those

localized states above the Fermi level, when increasing the applied field, may cross the Fermi energy, become populated and suddenly appear as new peaks in the FEEDs. This can be evident in the FN plot, too: when a new “window” for the emission opens, a kink in the curve -positively deviating- appears.

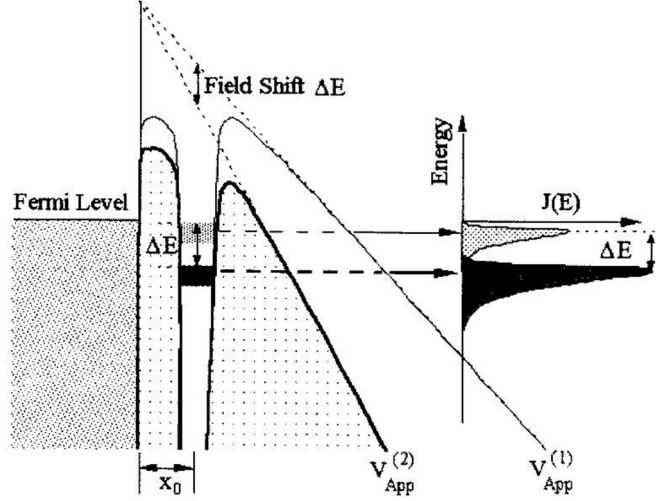


Figure 1.5: Schematic representation of tunnel resonant emission

This systems are also subjected to important heating due to Nottingham effect: when an electron is emitted from a lower level than the Fermi level, an electron in a filled, higher level will occupy that empty place dissipating thermal energy. A net heating of the system occurs and, due to the increase of the diffusion coefficient with temperature, the adsorbates move across the surface giving place to current instabilities and non-reproducibilities of both FEED and I-V. More details on adsorption will be given in the following section.

1.7 Vacuum requirements and cathode stability

1.7.1 Vacuum requirement

Field emission measurements heavily rely on the vacuum level of the system.

In general, when applying high voltage to a couple of metallic electrodes, if the pressure is not particularly low, a gas discharge occurs i.e. gas molecules get ionized and provide current transport from one electrode to the other making it

possible to measure a current. Many kinds of gas discharges are known, the most apparent -and most useful- of which is the glow discharge. Glow discharges and Townsend discharges consist of electron avalanches started by chance ionization events and are regenerated by secondary processes; the distinction between the two types is the quantity of created charge (enough to alter the applied field for the glow, not enough for the Townsend discharges). Arc-discharges are made up of electron avalanches and charges able to completely determine the field; they usually require tens of Volts and supply up to kiloamps current. They are widely known and exploited in physics. It is almost impossible to clearly distinguish from one kind of discharge to the other when varying the experimental conditions; nevertheless, it is evident that the lower the pressure, the harder to get the region between the electrodes conductive, the higher the voltage required to switch on the discharge.

Vacuum discharges are also possible as their occurrence depends on the level and quality of the vacuum. At the beginning of the investigation on field emission -in the early XX century- the bibliography on vacuum discharges almost coincides with the bibliography on field emission and now it appears miraculous the success of Millikan [12] in extracting a plausible experimental relation between current and voltage using the poor vacuum technology of that period.

Field emission measurements are generally carried out with working pressure ranging from 10^{-5} to 10^{-11} mbar. Chemisorption occurs at low-medium vacuum level: even with a sticking coefficient of 0,1, the deposition of a monolayer takes 1s at 10^{-6} mbar [19]: it is really difficult to get thoroughly clean surfaces and really easy to observe the phenomena described in sec. 1.6. Moreover, residual gas molecules in between the electrodes may get ionized by the electron flux, start complex collision/ionization processes which involves neighboring molecules that are at last attracted by the cathode. Therefore, in a field emission experiment, a wide range of phenomena going from adsorption to ion bombardment may occur at the expense of the cathode.

1.7.2 Cathode stability and failure

Inhibiting the full realization of field electron emitters as electron source for commercial application has been the stringent vacuum and environmental requirements necessary for stable, long-lived cathode performances. For most applications,

a time-independent I-V relationship is required. According to the Fowler-Nordheim law -see eqs. 1.19, 1.20, 1.25- the exponential factor $\phi^{3/2}\beta$ contains the sensitive parameters which control both short term and long term current stability. Failure mechanisms are exhaustively investigated by Dyke and Dolan [43] and Swanson [44]. When such mechanisms are minimized, the resulting improvement in performance and life of the cold cathode in steady-state operation will be noted; a list of them, which affects cathode stability and life, are listed below. They are strongly interrelated, so it is difficult to describe one of them without referring to another.

1. Emitters are subjected to non negligible tensile stress so that materials of low tensile strength are soon driven to irreversible failure due to electrostatic forces.
2. The emitters are subjected to Joule heating, especially those ones endowed with little radii of curvature and consequently high current density. Swanson ([44] and ref. therein) related the temperature of a W conically shaped emitter to the extracted current density: it occurred to be that if the radius of the emitter is $1 < r < 0,1 \mu m$, the maximum attainable current density before melting -for steady state operation- is $10^7 - 10^8 A/cm^2$ (calculated by using the actual area of the tip)
3. Before melting, however, thermal build-up starts to occur. Temperature encourages diffusion which, in pure metals, could be surface or volume diffusion. Therefore, at high level of current density, an emitter may change its shape. If the tensile stress due to the electric field is not high enough, the theory [44] predicts that the emitter will shorten. If the field is high enough that electrostatic tensile stress exceed surface tension stress, the net migration reverses and the emitter material flows towards the emitter apex. This process is known as thermal-field build up. Sharpening of the tip will switch a positive feedback (increase of current density, then increased diffusion rate concurring to the buildup process, increase of β and so on) which ends up with a arc-discharge-driven disruption.
4. Energetic ions incident on the emitter due to the poor vacuum level of to field-driven desorption processes at the anode may cause local roughness at which β increase. Again, the same positive feedback of point 2 takes place.

5. Residual gases, after adsorption, may alter the workfunction, thereby changing the I-V characteristic in an undesired fashion. Increase/decrease of current has been observed, depending this positive/negative effect of adsorption on both the nature of the emitter material and on the adsorbate nature. Increase of current may lead to a positive feedback that switches on buildup and then, at last, disruption.

In general, a good vacuum level and a heating treatment of the cathode prior operation are the only way to improve cathode life. Moreover, taking care of desorption means reducing the flicker noise as well. Accurate cleanliness of the anode is useful, as well.

Chapter 2

Field emission from carbon materials

Carbon materials have recently gained an outstanding role in the field of cold cathode materials.

The limits of the “conventional” metallic or silicon-based Spindt FEAs are due to the intrinsic nature of the materials: the metallic delocalized bond among the atoms provide a continuum of states in the energy bands and therefore a high mobility of the electrons, but, at the same time, this kind of bond is responsible for the observed high self-diffusivity and for the increase of electrical resistance with temperature (what makes temperature increase again and so on...).

The failure mechanisms described in the previous chapter are typical of metallic emitters and may be of a much lesser interest for a covalent solid endowed with strong bonds. As a consequence, low threshold emission from diamond films, reported in the early 80s, has stimulated much interest both from a technological and scientific point of view. In particular, the emission mechanism for a large bandgap material in the form of film is still matter of controversial debates. Research has been widened also to diamond-like and amorphous carbon but, as soon as carbon nanotubes were discovered and fully characterized, this new carbon material catalyzed the full interest of the scientific community involved in field emission.

2.1 Carbon nanotubes

Carbon nanotubes are a unique form of carbon filament whose structure is usually described by the rolling up of one or more graphene sheets. In the first case we are in presence of a Single Wall Carbon Nanotube (SWNT), the second case of a Multi Wall Carbon Nanotube (MWNT)

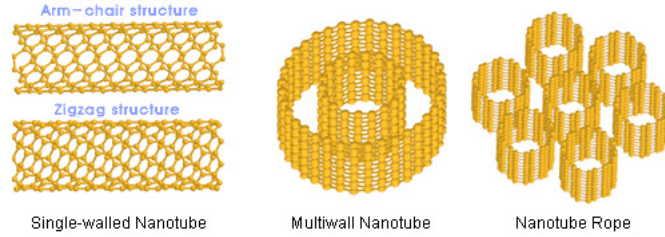


Figure 2.1: Examples of nanotube structures.

The most apparent feature of these structures is their high aspect ratio: their diameter ranges from 0,7 to 4-5 nm (SWNT) and it reaches some tens of nanometers in the case of MWNTs. Their length may reach the tens of microns. This ideal 1D structure has stimulated scientists to predict extraordinary physical properties.

The list of the unusual physical and chemical properties of carbon nanotubes is too long to be fully displayed here, so only a very brief report of them will be presented. Ref. [45] can be regarded as a good theoretical introduction to the world of carbon nanotubes.

To begin from the very beginning, a number of different nanotube structures can be thought by varying the orientation of the 2D lattice of the graphene sheet with respect to the axis of the tube; each structure is univocally described by a couple of integer indexes, named n and m , as illustrated in Fig.2.2. They represent the two coefficients of the linear combination of graphite primitive vectors describing the so called chiral vectors.

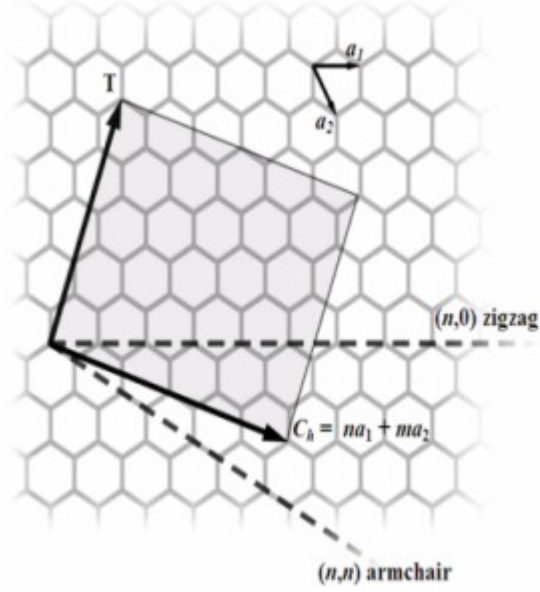


Figure 2.2: Nanotube chiral vector (C_h) on the 2D hexagonal graphene lattice. The nanotube is obtained by rolling up the lattice so that the one end of the vector is put on the other. a_1 and a_2 are the primitive vectors of the 2D hexagonal lattice. The integers n and m are called chiral indexes. Two particular cases (zigzag and armchair nanotube which are the most symmetrical structures) are also shown.

Each different couple of indexes leads, in the energy space, to a different electronic band arrangement; overall, the periodic boundary condition in the radial direction forces the density of states to a series of 1D Van Hove singularities.

The relative energy position of such singularities differs from structure to structure. The value of the bandgap varies as a function of the indexes, as well, thus making the electrical behavior of the corresponding tubes ranging from semimetallic to semiconducting. In particular, when $n - m$ is divisible by 3, the resulting nanotube is metallic; when $n - m$ is not divisible by 3, the corresponding tube is semiconducting.

Ballistic conduction in certain conditions [45] has been predicted, thus making nanotubes ideal 1D conducting wires in the nanometric version of a number of electronic devices.

The strong “planar” carbon-carbon bond inherited from graphite is basically

responsible for

- an incredibly high Young modulus
- low self-diffusivity even at high temperatures
- chemical inertness in relatively aggressive conditions
- low thermal resistance

Quantification of the above features and references for details are provided in the following table. The most popular applications of carbon nanotubes are listed in tab. 2.3; for each of them, one significant reference is given.

Optical properties		
Gap for SWNT whose n-m is divisible by 3 (metallic)	$0eV$	[46]
Gap for SWNT whose n-m is not divisible by 3 (semiconducting)	$0,4 - 0,7eV$	[47]
Gap for MWNT	$\approx 0eV$	[48]
Electrical properties		
Resistivity for SWNTs and MWNTs	$-4\Omega cm$	[46, 50]
Quantized conductance theoretical/measured	$(6,5k\Omega)^{-1}/(12,9k\Omega)^{-1}$	[46, 49]
Maximum current density	$7 - 9 A/cm^2$	[51, 52]
Thermal properties at room temperature		
Thermal conductivity for SWNTs	$1750 - 5800W/mK$	[53]
Thermal conductivity for MWNT bundle	$\approx 30W/mK$	[54]
Mechanical properties		
Young's modulus for arc-MWNTs/CVD MWNTs/SWNT bundles	$\approx 800GPa / \approx 27GPa / \approx 1000GPa$	[55, 56]
Tensile strength for SWNT bundles	$\approx 30GPa$	[56]

Table 2.1: Properties of carbon nanotubes

The list of the above features, together with the high aspect ratio of such structures, makes nanotubes the ideal material for field emission.

In particular,

- their aspect ratio directly determines their ability to amplify the applied electric field: this implies that CNT length should be maximized and the diameter minimized;
- their chemical inertness make them robust against ion bombardment;
- they can face the high tensile stress due to the high applied field;

Application	Properties utilized	Ref.
Transistor	Semiconducting nature of SWNTs	[57]
Energy storage	Intercalation of small ions/molecules inside NTs or in between the bundles	[58]
Scanning probe tips	High aspect ratio, small tip diameter, high elastic moduli	[59]
Supercapacitors	High surface area	[60]
Nanoelectromechanics	High elastic moduli, actuation through electric charging	[61]
Nano enclosures	High chemical stability, confined space within the tube	[62]
Spintronics	Spin transport with long coherence length	[63]
Chemical sensors	Influence of adsorption on electrical properties	[64]
Composites	High electrical conductance, elastic moduli	[65]

Table 2.3: Some applications of carbon nanotubes

- because of their high thermal conductivity, they can sustain higher current than metallic emitters because it is difficult to switch on the positive destructive feedback described in par. 1.7.2.

2.1.1 Carbon nanotube synthesis and characterization

The complete management of carbon nanotube synthesis represents the most challenging task in nanotube experimental research. A very brief review of the state of the art on synthesis will be provided here, mainly to list the key points.

First of all, up to now, there is no synthesis technique capable of growing a single type of CNT but abundance, purity, orientation and selected positioning onto predefinite areas of the substrates are appreciated features.

A number of different synthesis techniques have been set up. They can be roughly described as non equilibrium processes in extreme conditions i.e. high temperature, gas discharges. Carbon is provided as a solid -i.e. graphite- or as a gaseous hydrocarbon. SWNT growth requires a metallic catalyst in form of clusters. The three main categories of nanotube syntheses, are

- laser ablation. The process consists of a laser-induced sublimation of a solid target with successive re-condensation of the material [68].
- Arc discharge. Two graphite electrodes in a low pressure of an inert gas are involved in an arc: evaporation from the cathode is followed by deposition of material on the anode [69].

- Thermal activated, hot filament or plasma enhanced Chemical Vapor Deposition (CVD). A carbonaceous gaseous phase is activated by heat/heated filament/plasma; products of the decomposition of the gases and of the consequent deposition are obtained on a substrate [66].

The first two methods, which are really simply to be implemented and usually get effective results quite easily, produce abundant but non localized, dusty deposits.

Especially for arc-discharge the needed set-up is really inexpensive and the search for the optimal experimental conditions not so difficult. The synthesis of SWNTs generally requires a metal catalyst inserted as clusters into the solid carbon feedstock. Relative high quantity and high crystallinity of the product make arc-discharge the most widespread synthesis technique for nanotube mass production; as a consequence, the cheapest commercial carbon nanotubes are grown by arc discharge.

As in all kinds of nanotube synthesis techniques, a fine adjustment of the experimental conditions may drive to a selected kind of product; in this regard, laser ablation distinguished itself as the most promising technique to get a small spread of nanotube diameters.

The role of CVD techniques in the history of carbon material is crucial, so it is worth deepening the argument with a more general discussion.

Over the years CVD methods have helped to unveil the fantastic diversity of carbon structures: a wide range of carbon structures can be grown (from diamond, diamond-like carbon to tetrahedral amorphous carbon - named ta-C - and graphitic nanostructures such as nanotubes) and the properties of the structures can be controlled over a large range.

CVD techniques require more complex and more expensive (especially plasma enhanced CVD) set-ups than arc-discharge or laser ablation set-ups, but produce localized deposits onto suitable substrates. The process is generally catalyzed by a metal pre-deposited onto the substrate as a thin film or simply casted as a solution: the most popular catalyst is Nickel, but Cobalt and Iron are also widespread. Product quantity is generally very little, but selected positioning of the tubes is possible by exploiting a some kind of substrate selectivity due to direct/indirect action of the substrate itself on the catalytic activity of the metal or by simply patterning the catalyst as a thin film. Orientation is generally achieved by means of an applied bias, so that CVD represents the most promising growth technique

for field emission applications. Temperature is the limiting parameter in the choice of the substrate; for example, glass is generally not a suitable substrate for most of the CVD processes.

It is worthwhile stressing that, due to the different set-ups, different gaseous reactants, different substrates, different catalyst -both in nature and in physical phase- each synthesis process is unique: the as-grown material has in general its own self-organization, structure, and as a consequence physical and chemical properties.

The optimization of synthesis parameters, the full understanding of the growth steps and the achievement of a fully reproducibility of the process with prototypal CVD apparatuses are generally very hard tasks to be fulfilled, so that experimental research on nanotubes is often limited by *impasses* of the synthesis process. Generally speaking, the challenge is threefold: to produce in a reproducible way “novel” carbon-based materials like nanotubes, to form self-supported or supported carbon-based thin films and finally to integrate directly carbon nanostructures into devices.

As for the differences among the cited CVD techniques, there is no place here to describe them in detail but a shortcut is provided in tab. 2.4.

<i>Material</i>	<i>Thermal CVD</i>	<i>HF-CVD</i>	<i>PE-CVD</i>
<i>Diamond</i>	<i>No</i>	<i>Yes</i>	<i>Yes</i>
<i>SWNTs</i>	<i>Yes, 950° C</i>	<i>Yes, 750 °C</i>	<i>Yes</i>
<i>MWNTs</i>	<i>Yes, 650° C</i>	<i>Yes, 550 °C</i>	<i>Yes, 500° C</i>
<i>a-C:H</i>	<i>No</i>	<i>Yes</i>	<i>Yes</i>
<i>Polymers</i>	<i>No</i>	<i>Yes</i>	<i>No</i>
<i>Advantages</i>	<i>Simple set-up</i> <i>Continuous growth</i>	<i>Simple set-up</i> <i>Continuous growth</i> <i>Very versatile</i> <i>Large areas</i>	<i>High quality diamond</i> <i>Highly aligned nanotubes</i> <i>Very large areas</i> <i>No contaminant</i>
<i>Disadvantages</i>	<i>High substrate temperature</i> <i>Atmosphere adjustment</i> <i>not flexible</i>	<i>Contamination with</i> <i>filament atoms</i> <i>High hydrogen content</i>	<i>Expensive set-up</i>

Table 2.4: Schematic comparison of the different CVD techniques. After [102]

After synthesis, direct imaging of the morphology and of the direct structure of the samples can be achieved by -in order of resolution- scanning electron microscopy (SEM), atomic force microscopy (AFM) and transmission electron microscopy (TEM). When dealing with the thinner SWNTs as in this work, the lower

resolution microscopy technique such as SEM allows only the viewing of bundles i. e. aggregations of SWNTs.

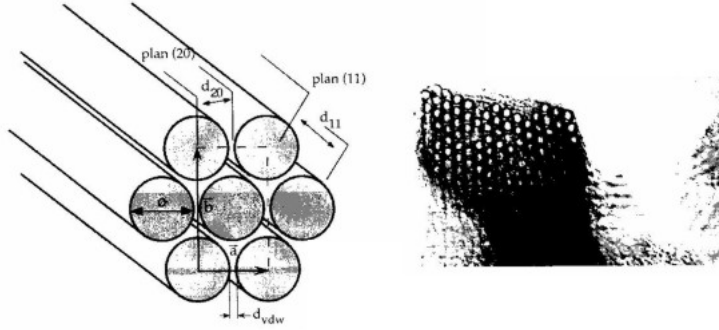


Figure 2.3: Scheme (left) and TEM image of a bundle of SWNTs (right).

Diffractive techniques (X-ray diffraction and electron diffraction techniques, RHEED among the many available) have been used less extensively. Structural information are given by Raman spectroscopy in the tangential mode ($1300 - 1700\text{cm}^{-1}$) and radial breathing mode region ($100 - 300\text{cm}^{-1}$). Scanning tunneling microscopy has been proved successful in confirming the unusual DOS in the energy space. As for this work, SEM, RHEED and Raman will be used to characterize the as-deposited material. Information about Raman characterization of CNT are provided in Ref. [45] while RHEED on CNTs is the subject of Ref. [67].

2.1.2 Field emission from carbon nanotubes

If one carries out a partial bibliographic research on <http://periodici.caspar.it/> (the search is limited only to Elsevier journals) with the following requirements

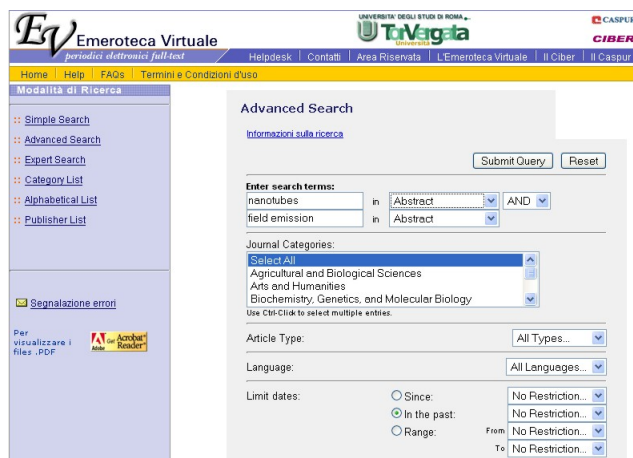


Figure 2.4: Webpage for bibliographic research of field emission from nanotube over Elsevier journals

one gets 338 records:

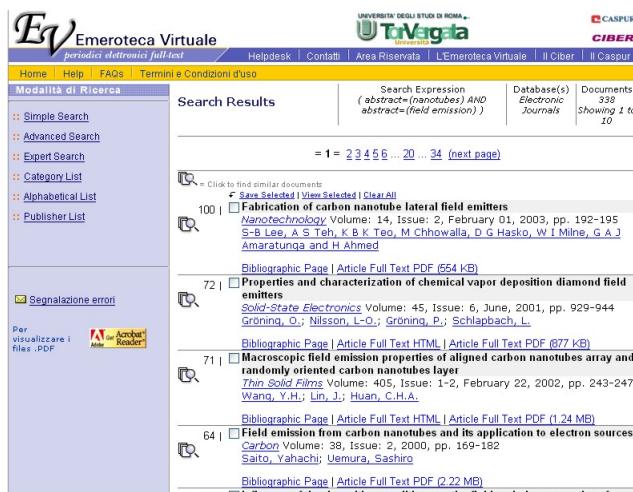


Figure 2.5: Bibliographic results for field emission from nanotubes over Elsevier journals

It is clearly impossible to give a complete review of literature on the argument, therefore, with the less ambitious goal of trying to point out only the most relevant points, a selection of results by a few leading research groups will be reported.

Experimental field emission studies have been carried out with a number of geometrically different set-ups. A great variety of nanotubes (as for nature, provenience, structures and self-assembly) has been used. They have been deposited onto different substrates by means of various techniques, what leads to very different morphological results. Keeping in mind these variables, it is not surprising to find in literature very different and often controversial data. The lack of a common framework for data analysis adds, at the end, a further reason of variety [70].

Beyond the numbers, the main questions about field emission from nanotubes can be listed as follows:

1. is CNT β enhancement factor as favorable as expected to decrease turn-on field up to few $V/\mu m$?
2. are CNTs able to supply stable high currents even in a medium vacuum level?
3. are CNTs metallic emitters?
4. are CNTs suitable for field emission devices?

2.1.2.1 Is CNT turn-on field more favorable than that of Spindt-type emitters?

The turn-on field of a Spindt FEA is 50-100 $V/\mu m$ [71], so the answer is undoubtedly “yes” even if it depends, obviously, on the definition of the turn-on field. There are discrepancies on this definition as well. Two of the most popular versions of turn-on field are the field needed to extract an integrated current density of $10\mu A/cm^2$ [70] or a current of $1nA$ [39]. Some authors considers only the threshold field, defined as the the field needed extract a current density of $10mA/cm^2$ [71] (the minimum required by a flat panel display [39]), while some others even confuse the threshold with the turn-on field [72].

2.1.2.2 Are CNTs able to provide stable high currents? Are they metallic emitters?

An emitter is generally considered metallic in character when its I-V curve follows the Fowler-Nordheim law (e.i. the corresponding FN plot is linear). However, Dyke and Dolan [26] recommended to explore an extended range of current to test the obedience to the Fowler-Nordheim law (they presented a current-voltage

curve involving 14 orders of magnitude). Unquestionable confirm comes from the measurement of FEED: if it is satisfactorily fitted by eq. 1.53, the emitter is metallic.

Some features of the observed I-V measurements on both single-CNT and macroscopic CNT-array samples opened the way to debates and discussions. Here are the main points:

1. emission from CNTs proves to be Fowler-Nordheim-like in the low current regime and negatively deviating in the high current regime [74, 75, 39, 73]. This saturation effect results in a knee of the FN plot;
2. I-V curves are noisy and not fully reproducible; at first current stability showed step-like behavior;
3. successive sweeps of voltage and/or heating of the sample improve reproducibility; after that, higher turn-on field may be observed;
4. when using a phosphor screen as anode [39], emission is seen as a spotty pattern. Individual spots appear and disappear as a unit, implying that they correspond to single emission sites. Because of the circular symmetry, emission seems to originate -as expected- from the end of the nanotubes rather than from the lateral walls.

All authors agree in explaining point no. 3 with the so called “conditioning effect” which is also known for conventional metallic emitters. Field emitted current, due to Joule effect, leads to self-heating. This helps to desorb adsorbed molecules or to drive them by diffusion into more stable configurations. The electric field has a role, as well, in the rearrangement of adsorbed molecules: it would drive them into conical structure -called Taylor cones- with a semi-vertical angle of $49,3^\circ$. Desorption, heat-driven diffusion and field-driven rearrangement lead all to a more stable configuration of the emitter surface resulting in a more stable emission. Moreover, it must be firmly kept in mind that, due to the exponential behaviour of the Fowler-Nordheim law, small differences in morphology or workfunction result in large differences in emitted current. CNTs are therefore not all equivalent as emitters: only the longest and thinnest of them will start to emit at low voltage; when increasing voltage others may start, and so on. It may happen that the best emitters reach their highest current regime and eventually fail when others are just

starting to emit. In such a way, a higher turn on field will be observed in further measurements.

As for the saturation effect (point no. 1), there is, in general, a number of possible reason for curved FN plot [81]:

1. adsorbed molecules (tunnel resonance emission, see par 1.6.1);
2. high electrical resistance of emitter substrate;
3. high electrical resistance of the interface between substrate and emitter;
4. voltage drop along the emitter;
5. structural modification of the emitter during emission;
6. space charge effect;
7. increase of temperature due to Joule heating;
8. electronic effect (free electron model not applicable to the system);
9. alignment of the emitter due to the applied field;
10. adsorption/desorption resulting in change of workfunction;
11. diffusion of adsorbed molecules;
12. degradation of the emitter.

The scientific community may have been looking for something new in field emission specifically related to the novel crystalline or electronic structure of nanotubes, however the view is now converging that the I-V curve and FEEDs from properly cleaned CNTs are governed to first order by the Fowler-Nordheim theory. However, to give some details on the complex and controversial argument of I-V saturation, some different views are here provided.

- Bonard [73] proposed that the observed negative deviation occurs because the electrons would come from localized states (hypothesized after finding very narrow energy spreads in their FEEDs) rather than from a continuum of states, so the emission would not be metallic. The hemispherical caps of CNTs were believed to generate such states.

- Altman [76] observed that even nanotubes with metallic character, due to the presence of defects along the walls, may exhibit semiconducting regions. A contact potential between the two different regions (e. i. Schottky barrier) could therefore exist thus constituting an energy barrier responsible of a threshold process (and therefore of a knee in the I-V curve).
- Zhu [39] invoked the space charge effect already described by Dike and Dolan [26]. The electron cloud, at high current regime, would be so dense that the applied field would be shielded by it, thus reducing the emitted current. Collins [75] deepened this argument by recalling that for conventional metallic emitters, switching for the not quite equivalent crystal facets may occur; in the case of nanotubes, at high current, some tips may preclude otherby, non equivalent tips from emitting until some instability leads to a reconfiguration of emitting sites. The first configuration of emitting tips is generally constituted by the best emitters (longest and thinnest), the successive configurations are generally less efficient, so the switching would result in an overall decrease of emitted current. This switch causes discrete jumps of current, when resolved in time. Moreover, when taking into account also the burning of the lowest-onset emitters and their replacement by other with higher onset-voltage, one realizes that the observed I-V characteristics is the effect of a complicated cooperative process in which each CNT emits, heats, saturates, turns off, cool down, emits again, eventually burns. This argument would explain points no. 2 and 4 as well.
- Dean [77] maintained that CNTs generally emit through stable adsorbate states even under ultrahigh vacuum conditions; these adsorbates states influence field emission current even by two or three orders of magnitude; change in adsorbate states might lead to a current saturation effect, too. He demonstrated that after suitably heating the sample, no deviation from Fowler-Nordheim law occurs. Semet et al. [74] showed also that repeated sweeps of the I-V curves could improve both reproducibility and obedience to Fowler-Nordheim law: self-heating due to emission would clean CNTs from adsorbates. Purcell et al. [42, 78] demonstrated that only through heating in ultrahigh vacuum conditions emitting CNTs get thoroughly cleaned from adsorbates. Their FEEDs measurements confirmed also that a linear FN plot is not enough to say that an emitter is metallic and doesn't emit through ad-

sorbate states. According to Purcell, only after a high temperature heating treatment under ultrahigh vacuum conditions, a CNT shows metallic character in field emission. In any case, the removal of adsorbates improves current stability as well, so that, within this framework, points no. 1-3 seem to be solved.

- Wei [79] and Kim [80] reported the alignment of CNTs under the action of applied field. This is a proof of the mobility of the tubes during field emission measurements: if the tensile strength of the field were able to align non-aligned tubes, an emitting CNT -with the help of its cloud of space charge- could affect the physical configuration of the nearby tubes. A dynamical picture of moving tubes could therefore be imagined. That would support the previously reported hypothesis of Collins [75] and fully explain point no. 4.

2.1.2.3 Potential for devices and prototypes

The use of CNTs as field emission electron sources is the basis of many of the closest-to-market applications for CNTs. In general these devices depend on the intrinsic CNT advantages of structural and chemical stability, high current carrying capacity, high aspect ratio, control and addressing of the synthesis process and, last but not least, low cost mass production.

As for heating resistance, Purcell [78] demonstrated that a single CNT heats up to 2000 K when emitting currents of about $1\mu A$. Stable high temperature of the emitter is an interesting point in field emission: CNT are the first example in literature of field-induced stable heating to any temperature above r.t.. This is believed to be due to two peculiar CNT features that differ from those of metal emitters which lead to current runaway and thus emitter breakdown. First, the electrical resistance of the MWNT utilized in the experiment was found to decrease with temperature, which gives a negative feedback to heating and, second, surface diffusion is much slower for covalent carbon which inhibits the field-driven sharpening (see par. 1.7.2).

Dean [83] investigated the environmental stability of field emission from carbon nanotubes which generally include resistance to oxidation and to sputtering. Considering that sputtering of typical refractory metals occurs in background gas pressures above $10^{-11} Torr$, *ad hoc* experiments were carried out exposing CNTs

to $10^{-7} - 10^{-6} Torr$ in controlled atmosphere of H_2 , H_2O , Ar , O_2 . O_2 resulted in the most evident effect on field emission current, with a rapid initial decrease; further long exposures (40 h) lead to substantial irreversible damage. Emission from unballasted CNTs for 100 h of dc biasing in $10^{-7} Torr$ of H_2O , however, showed negligible degradation for currents of about $1 nA$. Field emission displays generally operates with a 0,5% duty cycle; performing an extrapolation for CNTs, 100h of 100% duty cycle would result in 10000h at a 0,5% duty cycle.

Overall, CNT emitters were found much more stable in poor vacuum conditions than unballasted metal emitters; their environmental stability occurs to be among the best reported for any material, making them strong candidates for practical vacuum microelectronic device applications.

As for the required homogeneity of emission from macroscopic cold cathodes, the relation between morphology and field emission properties of the samples has been extensively investigated. It has been shown [82] that close packed arrays of CNTs are not ideal for field emission applications as the close packing of the tubes screens the applied field reducing the field enhancement of the high aspect ratio tubes. It has been calculated that it is necessary to have individual vertically aligned tubes spaced apart by twice their height to minimize field shielding effects and to optimize emitted current density. Moreover, dense and disordered samples are more prone to the switching process described in sec. 2.1.2.2 thus negatively affecting the necessary uniformity of emission. Density control during synthesis process has therefore become an urgent task achievable by refining the catalyst deposition techniques (in most cases sputtering combined with lithographic steps).

Being one of the promises of nanometric structures like nanotubes to open the way to miniaturization, the actual goal of device planning is to exploit the nanometric dimensions of CNTs and reduce of orders of magnitude the dimension of the devices. As a direct consequence, integration of CNTs into micrometric structures demands significant effort in reducing synthesis temperature and softening growth conditions.

However, a number of field emission devices making use of CNTs as cold cathodes has been proposed and realized in form of prototypes. These includes field emission displays (see for example [84]), lighting elements [85], high brightness electron microscopy sources [86], micro-cathode for parallel electron lithography and microscopy [87, 88], ionization vacuum gauges [89], gas discharge tubes [90], portable X-ray tubes and rf amplifiers. The latter two devices will be described in

detail elsewhere.

2.2 Diamond films

It was already classified as a cold cathode material for photocathodes in 1979 [92] but no one would consider obtaining also field emission from diamond until an inexpensive synthesis technique was set-up. Currently, although one-dimensional structures such as carbon nanotubes are generally considered better field emitters, a strong research interest in field emission from diamond and related films remains due to the unique properties of diamond. Compared to the micro/nanotip emitters discussed so far, the scenario of a thin film cathode is much different. Apart from the simpler device fabrication, the use a film instead of a tip would lead to some advantages:

- the emission current originates from a relatively large surface so that the current density is much smaller;
- due to the absence of highly focused and intense electric fields, the problem of sputter erosion and emitter contamination due to ion bombardment are largely reduced;
- as the fields are low, the capacitance of the emission cathode is low, thus enabling high frequency operation.

2.2.1 Properties

Diamond is the most appealing allotrope of carbon. It is formed by sp^3 , tetrahedrally bonded carbon atoms, so that, in its most common crystalline structure, a sphalerite-like crystalline structure is formed. A glance at any handbook of material data properties will prove that diamond is almost always “the biggest and the best”. Among other properties, diamond is the hardest known material, has the highest thermal conductivity at r.t., is transparent over a very wide wavelength range, is the stiffest material, the least compressible and it is inert to most chemical reagents. With such a wide range of exceptional properties, it is not surprising that diamond has sometimes been referred to as the “ultimate engineering material”. A selection of some of these properties is given in the following table.

Extreme mechanical hardness (ca. 90 GPa) and wear resistance
Highest bulk modulus ($1,2 \cdot 10^{12} N \cdot m^{-2}$)
Lowest compressibility ($8,3 \cdot 10^{-13} m^2 N^{-1}$)
Highest r.t. thermal conductivity ($2 \cdot 10^3 W K^{-1}$)
Very low thermal expansion coefficient at r.t. ($1 \cdot 10^{-6} K$)
Broad optical frequency from far UV to far IR
Highest sound propagation velocity ($17,5 Km/s$)
High electrical resistance (r.t. resistivity ca. $10^{13} \Omega cm$)
Very resistant to chemical corrosion
Biologically compatible

Table 2.5: Some of the outstanding properties of diamond

Unfortunately, in the past it has proved very difficult to exploit these properties, due both to the cost and scarcity of large natural diamonds, and the fact that diamond was only available in the form of stones or grit.

2.2.2 HFCVD synthesis

Although the standard enthalpies of diamond and graphite only differ by 2,9 kJ/mol, it is widely known that at room temperature and pressure a large activation barrier prevents interconversion between the two forms. Therefore, in order to synthesize diamond, researchers tried to look for the needed conditions where diamond is the more stable phase. The knowledge of the conditions under which natural diamond is formed deep underground suggested that diamond could be synthesized by heating carbon under extreme pressures: in such a way the so called high-pressure-high-temperature technique gained role. This method produces single crystal ranging in size from nanometers to millimeters but what is required by most potential applications aiming to exploit the superlative properties is often a thin film.

Rather than try to duplicate nature's method to create it, diamond could conceivably be produced if carbon atoms could be added one-at-a-time to an initial template, in such a way that a tetrahedrally bonded carbon network results. The idea of the thermal decomposition of carbon containing gases under reduced pressures paved the way to the common Hot Filament Chemical Vapor Deposition technique. By means of the only thermal decomposition, the growth onto on the surface of a natural diamond crystal occurs, but the growth rate is really low, since

graphite is co-deposited with diamond. A breakthrough came when it was discovered that the presence of hydrogen during the decomposition process leads to the preferential etching of graphite. Nowadays that all processes have been optimized, it can be summarized that diamond growth normally requires a carbon containing precursor gas (usually CH_4) diluted in excess of hydrogen in a typical mixing ratio of 1% vol. Also, the temperature of the substrate is usually higher than 700°C. In an Hot Filament system, atomic hydrogen, produced heterogeneously by thermal decomposition of H_2 on the hot filament surface, drives the whole chemical system. First, although the bulk of diamond is sp^3 bonded, at the surface there is effectively a dangling bond which needs to be terminated in some way in order to prevent cross-linkage and subsequent reconstruction of the surface to graphite: this surface termination, during growth, is performed by hydrogen. Second, atomic hydrogen etch graphite carbon many times faster than diamond-like carbon. Third, atomic hydrogen is an efficient scavenger of long-chained hydrocarbons thus preventing the build-up of polymers or large ring structures. Finally, atomic hydrogen reacts with neutral species such as CH_4 to create reactive radicals such as CH_3 which can then attach to suitable surface sites. By the simple expedient of changing the growth conditions, diamond films can be deposited with properties ranging from almost graphitic to those of natural diamond. For example, the surface morphology of the film depends critically upon the various process conditions, especially the gas mixing ratio. Generally, with increasing methane concentrations, the crystal sizes decrease, until above ca. 3% CH_4 in H_2 the crystalline morphology disappears altogether. Such a film is referred to as nanocrystalline or *ballas* diamond and may be considered an aggregate of diamond nanocrystals and disordered graphite.

2.2.3 Electronic structure

Diamond is an electrical insulator or, depending on the point of view, a wide bandgap semiconductor. In a bulk, single crystal, pure diamond, the conduction band minimum is about 5.5 eV apart from the valence band maximum. The energy difference between the vacuum level and the conduction band minimum is called the electron affinity and labelled as χ : it has been shown that pure diamond has an electron affinity of about 0.4 eV while a hydrogen covered diamond may have a negative electron affinity (NEA) [4]. That means that should an electron reach the conduction band minimum, it would be emitted without overcoming a barrier

(ballistic emission). For a diamond film synthesized by HFCVD, the surface will automatically be terminated with hydrogen. Cui et al. [91] attributed the NEA to the surface dipole formed by $C^- - H^+$ bond at the surface. The length of the dipole was estimated to be 1,1 Å[91] and an electron will see a potential drop in the dipole layer as large as 1,65 eV, which is equivalent -according to Cui, who attributes to NEA for (111) surface the value -1,27 eV- to the change in χ . This large value would be due to the high density of surface dipoles on account of the small lattice constant of diamond. However, the exact value of NEA of a diamond surface depends on the degree of coverage with hydrogen (which is generally studied with photoelectron spectroscopy): Cui experienced that when the surface is fully hydrogenated, its negative electron affinity was determined to be -1,27 eV for the (111) surface; this value can be gradually increased to a positive electron affinity equal to +0,38 eV by removing hydrogen step by step.

The idea of getting diamond more conductive has always been an appealing task: both p-type and n-type doping has been persecuted.

P-type doped diamond occurs naturally, p-type semiconducting properties being supplied by a certain quantity of B atoms. Its poor abundance and reproducibility in electronic properties makes it unuseful for the desired -electronic, optoelectronic- applications.

Diamond can be doped artificially by ion implantation but a further annealing step is needed to remove the structural damages due to the ion beam. Moreover, graphitization and amorphization may occur, what makes the technique of relative usefulness. CVD technique, where B-containing precursors or B_2H_6 are usually added to the gaseous mixture in the reactor, has proved so suitable for doping diamond that it is nowadays of industrial application. However, it has been shown experimentally that the bandgap of intrinsic diamond begins to decrease with a concentration of B atoms larger than $10^{19} atoms/cm^3$ [98]. For B concentration larger than $10^{20} atoms/cm^3$ diamond behaves as a semimetal with a resistivity of $0,001 \Omega/cm$ [98] (high doping levels are to be avoided if one needs a certain degree of crystallinity).

N-type doping of diamond is a more challenging task than p-type doping. The presence of a donor level near the conduction band minimum would make emission -whether field-induced or photostimulated- much easier; moreover, the availability of n-type diamond would pave the way to the realization of p-n junctions and therefore of a number of electronic devices. The search for donors must involve

atoms with the right features to fit in the diamond lattice; they are the alkaline metals such as Li and Na which can occupy interstitial sites, V-group and VI group elements destined to substitutional sites. Among these, the only guest atom which, so far, has given clear proof of doping diamond is P [99, 100], inserted by the use of P-containing molecules (PH_3) in CVD synthesis.

Last but not least, structural defects such as vacancies, impurities (the most common of which is constituted by H), grain boundaries, sp^2 hybridized C atoms may lead to the formation of defect-induced bands endowed with a donor character: they may be responsible of electron hopping processes which generally enhance conductivity. This is the reason why, when studying the electron transport in a nominally doped diamond, it is really difficult to separate the donor contribution from the defect contribution.

2.2.4 Field emission

Even if low threshold emission from diamond has been widely measured, the easy extraction of electrons from an insulator seems to be a mysterious process. Threshold fields ranging from 160 to 1,5 $V/\mu m$ [94, 4] have been reported, what enrolls diamond in the list of the best materials for field emission. However, this data are highly misleading when taken without further details: the word diamond nowadays vaguely defines an entire class of carbon materials with different sp^3/sp^2 ratios, different defectivities in both phases, different grain sizes, different impurity inclusions. Beside field emission data, careful characterization of the as-synthesized material must be provided, as well as details on the whole field emission behavior of the sample (and, of course, on the experimental field emission set-up and data extraction methods, see sec. 1.4). Overall, some trends have been recognized:

- high level of defectivity lowers the threshold field;
- up to a certain degree, the presence of a sp^2 phase lowers the threshold field;
- the emission pattern is spotty;
- it is sometimes necessary a sort activation process to get further good field emission.

Low threshold field emission from diamond has been at first explained in terms of NEA, but nowadays it becomes more and more clear that the link between NEA

and field emission is not so straightforward. A number of different mechanism have been invoked, but very few of them are supported by a FEED investigation after a careful cleaning treatment at high temperatures in ultrahigh vacuum conditions. It is worthwhile recalling that cold cathodes may not require such extreme conditions to operate, but, since the process depends critically on the state of the surface, very controlled conditions are a must when studying the emission mechanism. A short review of the most relevant mechanism hypotheses will follow, with a special attention paid to eventual thermal treatments of the sample and FEED investigation; some of them are clearly in contrast with each other, some others introduce elements susceptible of intervening in more than one proposed mechanism. From the review it can be extracted that the variables which have to be taken into account are very many and very few investigations are really complete.

- Schlessler [96] exalted the role of the metallic back contact that supplies electrons to compensates those emitted from the surface. The system made up by the substrate and the diamond film constitutes a Schottky barrier: depending on the relative value of the workfunction of the metal substrate and of the diamond film, band bending can be induced in the diamond film. Electrons from the metal substrate can therefore tunnel through the Schottky barrier, thermalize to the conduction band minimum of diamond and then, driven by a diffusive process, be emitted from the diamond surface (with or without a barrier depending on the sign of the electron affinity). Within this framework, the main barrier to be overcome would be not the one between diamond and vacuum but the one due to the metal/diamond interface. Measurements on commercial diamond powders deposited on a Mo tip were carried out: no heating of the sample was performed, but a series of FEED at different bias voltages were recorded. The spectra showed a single peak which may be ascribed to a metallic-type emission; the position of the peak decreased linearly with the increase of the applied voltage while for a simple, uncoated Mo tip no shift was observed. According to the authors, this can be explained by band bending: the higher the voltage, the lower in energy the conduction band minimum so, the lower the energy of the emitted electrons. According to the model, the emission would come from the very bulk of the material.
- Geis [96] proposed, for CVD diamond, a more complicated emission model which involves the triple junction sp^2 conductive carbon/diamond/vacuum.

The emission, in this case, would be a pure surface process.

- Cui [93] investigated *ad-hoc* hybrid systems of mixed graphite and hydrogenated diamond. According to his view, the electrons would be emitted from the conductive graphitic phase, but just outside the solid they would feel a lower energetic potential in front of the diamond phase (because of the negative electron affinity). From the constructed equipotential line, it can be argued that the electrons emitted from graphite are able to escape into vacuum without overcoming the 5 eV workfunction barrier of graphite, but actually feel the lower barrier of diamond. The range within which such effect would be effective is estimated to be 20 Å. The lateral extent of the high energy barrier of graphite would reduce as the size of the graphite grain shrinks. For grains of a few tens angstrom the barrier is expected to disappear and all electrons would have an emission threshold that varies with the workfunction of diamond. This scenario is expected to hold in polycrystalline diamond films where the graphitic phase is reduced to grain boundaries.
- Groening [97] examined CVD diamond samples with different features: highly crystalline and poorly crystalline, nanocrystalline diamond. He verified that high quality diamond undergoes a sort of activation before starting emission. Such activation process resulted to be an electrical discharge phenomenon creating a crater. Low threshold emission would be, therefore, due to the formation of a crater able to enhance the applied field and not to the intrinsic properties of diamond. Emission from poorly crystalline, nanostructured diamond (which is highly defective by definition) occurred to be good (threshold field lower than 10 V/ μm). FEED spectra showed a single metallic peak located within 0,1 eV from the Fermi level with a FWHM of about 250 meV. From the combined I-V and FEED measurement the authors extracted both workfunction Φ and field enhancement factor β : Φ occurred to be about 6 eV, while β more than 1000. Within this framework, low threshold emission from a CVD diamond film would be due to the classical Fowler-Nordheim tunneling through a barrier with the help of a geometrical field enhancement effect due to the nanometric structure of the surface.
- Zhu [39], after investigating CVD diamond films with different defect density (estimated by Raman scattering), concluded that the applied field required for emission can be significantly reduced in presence of a number of structural

defects. It would be likely that the broad types of defects present in the diamond structure create additional energy bands within the bandgap thus contributing to electron emission at low applied fields.

Apart from the thesis of Schlessler [96] (whose emission mechanism, however, can be integrated with the observations by Zhu [39]), only one thing seems to be sure: to be a good emitter diamond needs the presence of structural defects and impurities. The presence of localized defects and/or conductive channels due to the inclusion of a graphitic phase, together with a distribution of morphological protrusions may explain the discrete emission pattern which has been at first unexpected for an emitter in form of film.

Overall, it is difficult to prefer one of the presented emission mechanisms over the others since the differences in material structure, morphology and investigation techniques make the obtained results and the corresponding proposals quite misleading. It is to be noted, however, that no one performed the necessary careful annealing treatment with a subsequent FEED investigation, what could have put an end to this long-lasting question [101].

Chapter 3

Experimental: growth of CNT-based materials

3.1 HFCVD experimental set-up

The synthesis apparatus utilized in this work consists of a conventional HFCVD reaction chamber connected to a powder flowing system (Patent M. L. Terranova, M. Rossi, V. Sessa, S. Piccirillo MI98A001159 extended to PCT/E999/0347). A scheme of the apparatus is shown in Fig. 3.1.

The reactor is made up by a 26 cm wide and 27,5 cm high cylindrical stainless steel vacuum chamber. It is connected in series to a rotative pump (Trivac 150 CVS) -enabling, alone, a pressure of $10^{-3} Torr$ - and to a water-cooled turbomolecular pump (Turbovac 150 CVS), used to evacuate the reactor up to $10^{-5} Torr$. An *ensemble* of fluxmeters, valves and connections have been set up to exploit a number of different experimental conditions. Pressure inside the reactor is measured by means of three gauges, each of them purposely devoted to a different step of the process of evacuating the system and of establishing the desired conditions of pressure and atmosphere composition.

A 0,6 mm thick wire, rolled up into 20 coils to get a 1,5 mm long, rolled resistance, constitutes the Ta (Plansee, with a purity of 99,85 %) filament used to activate the gaseous phase.

The choice of Ta is typical in HFCVD set-up: it is an inert, high-melting metal

capable of reaching temperatures of more than 2000°C by Joule heating exposed to pressure of a few tens of Torr. The disadvantage in using a Ta filament -and HFCVD technique in general- is the slight but inevitable contamination of the product with atoms coming from the filament by sputtering.

In our set-up the filament is heated by a dc generator and kept under control by means of a pyrometer. The sampleholder is cut from a sintered 60 μm thick Mo slab (99,95% purity); its temperature is adjusted by means of a AC current generator while measured with a Pt/Pt-Ir thermocouple. Since it occurs to be one of the key parameters in the synthesis process, the distance between filament and sample holder is monitored by an external measurement system (it is possible to mechanically intervene during growth, too).

The powder cell is made up of a purposely realized glass reservoir connected to a gas flowing system. The used carrier gas is Ar. A metallic injector enables the gas-driven powders to reach the inside of the reactor; a Mo nozzle provide the powder delivery above the sample holder, just under the filament. The powder flux can be mechanically oriented from about 10° to about 80° with respect to the plane of the sample holder while the hydrogen flux is always perpendicular to the sampleholder.

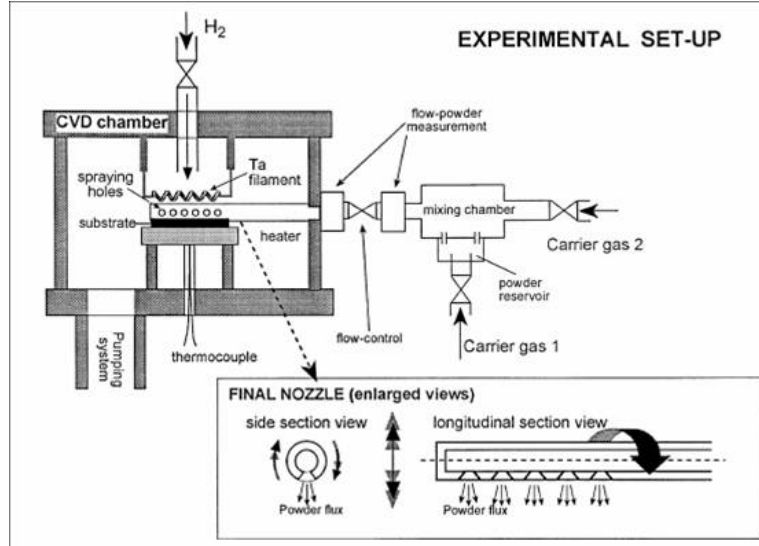


Figure 3.1: Scheme of our HFCVD apparatus

3.2 Characterization: experimental set-ups

Characterization step of the as-grown material has been carried out by means of a morphological technique (electron microscopy) and two structural techniques (Raman scattering and electron diffraction).

3.2.1 Field emission gun scanning electron microscope (FEG-SEM)

The first morphological characterization is carried out with a field emission gun-SEM (FEG-SEM). Our apparatus -Hitachi S-4000- enables a theoretical maximum magnification of 300000x when coupled to a theoretical, perfect regularity and crystallinity of the sample; lower magnifications (generally about 80000x with our typical samples). Extraction voltage is about 3-5 kV, accelerating voltage is fixed at 20 kV. A collector for secondary electrons is used. Digital image acquisition is carried out both by the use, in low resolution, of a common video card and by the use of a home-made high resolution image acquisition software (LabView).

3.2.2 Raman spectrometer

As for structural, Raman characterization, a home-assembled apparatus is used. The air-cooled, horizontal polarized Ar+ c.w. laser (maximum power 100 mW, tunable on the 3 different lines of Ar+ but utilized mainly with the fundamental one of 514,5 nm) after overcoming a plasma filter, two mirrors, a prism and a focusing lens is spot onto the sample, kept in vertical position by means of a sample holder. The measurement geometry is the backscattering one (typical for solid, opaque samples) so that, after a couple of focusing and a collimating lenses and a supernotch filter (Kaiser), the beam enters a monochromator (Oriel) with a 1200 gr/mm grating and 25 cm long optical path. A nitrogen-cooled, GPIB-controlled multichannel charge-coupling device (Jobin-Yvon) is used to collect the signal. Spectramax is used as acquisition software. After exporting the spectra files, Microcal Origin is used to analyze them.

3.2.3 Reflection High Energy Electron diffraction (RHEED)

RHEED analysis has been performed by Prof. Marco Rossi, Dept. of Energetics, University of Rome La Sapienza. His set up (AFI EM6G) is equipped with a 60 kV

working energy, high resolution diffractometer used in selected area configuration. A goniometer enables the optimization the grazing incidence angle of the electron beam with respect to the sample and to move the sample itself parallel to the electron beam (i.e. to scan over the sample).

3.3 Carbon nanotube growth

Though by definition CVD techniques make use of gaseous reactants, our peculiar set-up enables us to use a solid carbon feedstock in form of powders.

The already set-up process of carbon nanotube growth making use of carbon nanopowders (see following subsection) has been already interpreted as the succession of the following steps [112]:

- particle surface etching by atomic H
- formation of sp^2 -carbon clusters in gas phase
- self-aggregation into nanographenic sheets
- closing and wrapping of sheets on metal clusters surface
- growth of graphitic network by further addition of clusters



Figure 3.2: Schematic drawings of particle etching, formation of graphenic clusters in the gas phase and early stage of aggregation driven by metal clusters

Within an optimized procedure for SWNT growth [108, 109], this work is focused to:

1. CNT growth from the three different solid carbon feedstocks (carbon nanopowders, diesel soot, commercial graphite). SWNT growth from carbon nanopowders showing different morphologies to be tested in the field emission set up.

2. selected area growth
3. diamond-covered CNT growth

3.3.1 Carbon precursors

The main form of carbon powders used in this work were produced at the ENEA research center of Frascati by laser ($10,5\mu m$) pyrolysis of an ethylene/acetylene mixture [103]. At SEM analysis [104] they appear as spherical aggregates with an average diameter of 50 nm. A previous work [104], focused to the characterization of the molecular fraction of the material, evidenced the presence of hydrocarburic and aromatic compounds made up by more than 2 condensed benzenic rings. Larger C_n fragments, including C_{60} , were also evidenced.

The search for less expensive solid carbon precursors lead us to investigate the possible use of diesel soot and commercial micrometric graphite.

While laser-produced carbon nanopowders and graphite can be considered almost pure, as for diesel soot, one cannot ignore the presence of a number of impurities due to the complex phenomena taking place in the combustion chamber of the engine. A complete characterization of diesel soot is difficult due to the wide range of possible contaminants: some analytical studies, focused to its environmental impact, revealed the presence of oxygen containing heavy hydrocarbons, NO_x products, sulfates [110], while, if concerning metals, B, Ca, Cu, Fe, Mg, Zn have been found [111]. These data are to be intended only as indications of some possible impurities as soot composition may widely differ from one engine to another, and even for the same engine and fuel, further variations can be due to temperature, humidity etc... Therefore, the aim of these synthesis experiments is the preliminary exploration of different, widely spread and cheap carbon feedstocks in CNT synthesis. The full understanding of the growth mechanism is beyond the scope of this thesis as well as the investigation of the role of all metals and impurities possibly acting as catalyst in the process.

Extraction with organic solvents of a sample of graphite and diesel soot did not reveal any molecular aromatic fraction, so, though not innocuous, the powder constitutes a danger for human health due only to their breathability. Raman analysis has been carried out as a preliminary characterization step to roughly compare their structure with that of carbon nanopowders. Fig. 3.3 shows the Raman signals of the three different materials in the tangential mode region (i.e.

1200-1900 cm^{-1}).

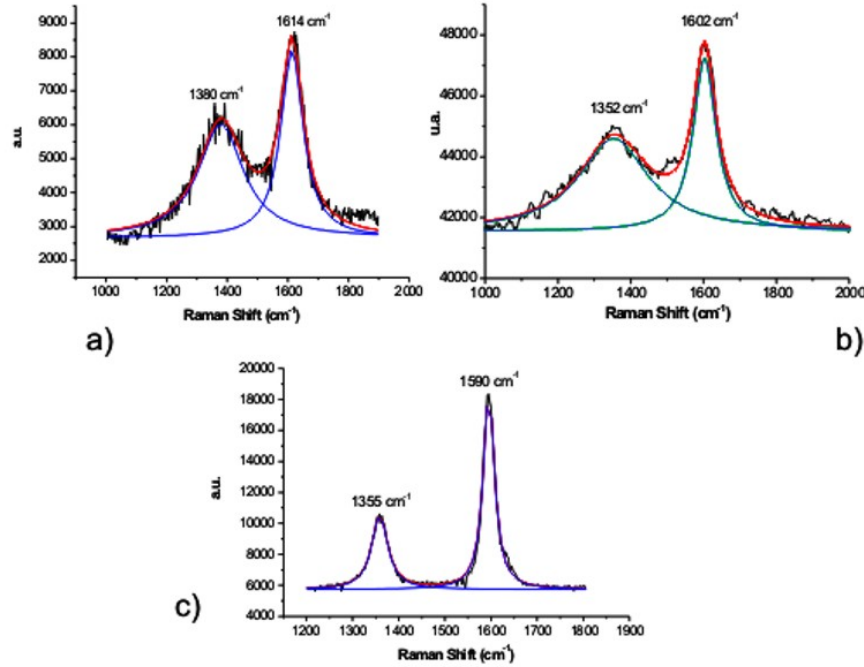


Figure 3.3: Raman spectra in the tangential mode region of a) carbon nanopowders obtained by laser pyrolysis; b) diesel soot; c) commercial, micrometric graphite (Aldrich)

All of them show the typical features ascribed to graphitic systems i.e. the so called D (1300-1400 cm^{-1}) and G (1580-1650 cm^{-1}) bands: that indicates the abundance of sp^2 over sp^3 C-C bond. Both nanopowders and diesel soot show broad bands with the D one overcoming in intensity the half of the G one; sharper peaks are, on the contrary, displayed by graphite. Moreover, significant differences in the position of the bands between nanopowders and diesel soot on one side and graphite on the other, can be observed.

Theoretical calculation on a perfect, infinite graphite lattice and experimental investigations on Highly Oriented Pyrolytic Graphite (HOPG) locate G band at 1582 cm^{-1} with a Full Width Half Maximum (FWHM) of few tens of cm^{-1} ; D band is not expected since its origin is ascribed to the limited extension of the lattice and

to structural defects [105]. The increasing D/G ratio (sometimes calculated as the intensity, sometimes as the area ratio) as well as the increase of the FWHM of both bands are sign of an increasing concentration of defects; moreover, the blue-shifting of the G band is interpreted as the shrink of the lattice to the nanometric domain [107]. Quantitatively, the $I(G)/I(D)$ ratio, after correction with a wavelength-dependent coefficient, gives an estimation of the average dimension of the crystals [106].

As for diesel soot and carbon nanopowders, the position of the G band confirms the nanometric nature of the systems; FWHM of both bands indicates the same degree of structural disorder; moreover, the $C(\lambda) \cdot I(G)/I(D)$ ratio, calculated according to Tunistra *et al.* [106], reveals the same average extension of graphitic domains of about 10 nm.

Significant structural differences must be ascribed to the commercial micrometric graphite, whose G band position is much closer to that of HOPG; the intensity of D band with respect to the G band is smaller than in the previous case thus indicating a more regular graphitic lattice. However, the above relation between the $I(G)/I(D)$ ratio and the dimension of the crystalline domain cannot be applied because of the micrometric structure of the material.

Overall, since the carbon nanopowders have already proved successful in SWNT growth [108], similar results with the same experimental conditions are to be expected by the use of diesel soot; as for graphite, more suitable synthesis conditions have to be searched for.

3.3.2 Experimental conditions of HFCVD synthesis of CNT and diamond-covered CNTs

Due to the low cost and large availability, (100), p-doped Si wafers cut in 1cm x 1 cm squared pieces have been used as substrate for nanotube synthesis. Though doped-Si melting point is lower than that of intrinsic Si, it is stable at the required high synthesis temperature and displays a non negligible robustness towards hydrogen etching.

CNT growth by means of CVD technique is always catalyzed by some transition metal: experimental conditions have been here optimized for Fe, either casted onto the substrate from an $10^{-5}M$ acetone solution of $Fe(NO_3)_3 \cdot 9H_2O$ or sputtered as thin metallic film. In the former case, particular care must be paid to the homo-

geneity of the catalyst dispersion on the substrate which is qualitative estimated by eye and sometimes by SEM; as for the latter methodology, strong adhesion of the Fe film onto the Si substrate is demanded from the sputtering process to resist to the aggressive synthesis conditions.

In both cases, a pre-growing step is needed. As for the substrate obtained by casting, since the active form of the catalyst is the metallic one, a chemical reduction of Fe^{3+} into Fe^0 must be performed; as for the sputtered layer, both a reduction of the superficial monolayers of oxide and a clustering of the film is required. The exposure of the substrate to reactive hydrogen atmosphere (switching on the H_2 flow and not the Ar one) constitutes an effective reduction treatment. Moreover, the aggressive nature of atomic H performs a some kind of bombardment, and thus of etching, leading to the clustering of the Fe film.

CNT selective growth in predefinite areas of the substrates has been achieved with two different approaches:

1. by the use of lithographically patterned $Si/1\mu m$ thick SiO_2 substrates onto which a continuous layer of $Fe(NO_3)_3 \cdot 9H_2O$ has been already casted;
2. by the use of lithographically patterned Fe-covered $Si/1\mu m$ thick SiO_2 substrates.

As for point no. 1, Orlanducci *et al.* [109] reported that, though the catalyst is casted all over the substrate, growth occurs only on the Si-exposed areas. This is attributed to the fact that the reduction step prior growth cannot be efficient onto oxidized surfaces, so that the catalyst cannot achieve its active form. The same effect was observed during this work for Nb_2O_5 surfaces.

Starting from $Si/1\mu m$ thick SiO_2 commercial wafers, all substrates described in the above points no. 1 and 2 have been purposely realized in the clean room of the Dept. of Physics, University of Rome Tor Vergata by Francesca Brunetti and Riccardo Riccitelli from the Dept. of Electronic Engineering, University of Rome Tor Vergata. They realized also multilayer patterned substrates constituted by $Si/SiO_2/Nb/Nb_2O_5$ to be tested for CNT growth.

As described in Ref. [108], abundant, reproducible growth of bundles (see Fig. 2.3) of CNTs is obtained with the following synthesis conditions:

- filament temperature $2100 \pm 50^\circ C$;

- substrate temperature $850 \pm 50^\circ C$;
- typical filament/substrate distance 6-12 mm (varying according to the experiments);
- H_2 flow 200 sccm;
- Ar flow 10-40 sccm (varying according to the experiments);
- working pressure 36 Torr;
- typical pre-growing step + growth time 3 + 5-15 min (varying according to the experiments);
- when not differently indicated, Fe catalyst is provided by a $Fe(NO_3)_3 \cdot 9H_2O$ acetone solution ($10^{-5} - 10^{-6} M$).

The above conditions constitute the framework around which all synthesis experiments were carried out. Some parameters (filament/substrate distance, Ar flow, growth time) are indicated as variable in a well defined ranges. The sense of this variability is explained in the following points.

- Variability in catalyst concentration is used to get different SWNT bundle density (being the deposition process already optimized for carbon nanopowders, they have been used for all experiments when not otherwise indicated).
- When using carbon nanopowders and diesel soot as feedstock, 40 sccm Ar stream is used; total synthesis time is 3 min pregrowing + 5 min growing step; the distance between filament and substrate is set to 12 mm.
- When using graphite as feedstock, the Ar stream is reduced to 10 sccm due to the much larger size of the particles; for the same reason the growing step is set to 10 minutes.
- By the use of carbon nanopowders, diamond-covered SWNT bundles have been obtained and a time study of such growth is performed by varying the growing time from 1 to 15 minutes with a reduced substrate/filament distance of 8 mm. In details: 3 different runs have been performed with each of the following growing time: 1, 2, 4, 6, 8, 10, 15 minutes.

3.3.3 CNT growth from different catalyst concentration and different solid carbon feedstocks: results and discussion

As for the samples got by the use of carbon nanopowders and the $Fe(NO_3)_3 \cdot 9H_2O$ acetone solution in a concentration range of $10^{-5} - 10^{-6} M$, three different morphologies have been obtained. SEM images are shown as representative of the three cases in Fig. 3.4. Though the magnification is a bit different (in the case of sample A the whole length of the scale at the left bottom corner is $7,50 \mu m$, for sample B it is $5,00 \mu m$, for sample C it is $6,67 \mu m$) it is possible to see that sample A shows sparse, curled, disordered SWNT bundles; sample B has more straight and shorter bundles, the density is more than in sample A; sample C is made up of ordered, aligned, densely packed SWNT bundles. As for the thickness of the bundles, from the thickest to the thinnest the order is: sample B, sample C, sample A.

As for the preliminary experience of the alternative carbon feedstocks, a more detailed characterization process is needed.

The overall morphological appearance of the each whole sample is first checked by our FEG-SEM at low magnifications; micron-scale and, when possible, nanometric scale arrangement are investigated.

Carbon nanopowders and diesel soot were found to lead to morphologically similar samples. When using plain Si substrate, aligned filamentous structures roughly self-assembled in a sort of lawn are generally seen all over the substrate. The direction of such alignment was found to depend on the orientation of the nozzle inside the HFCVD chamber [109]. Length and dimensions of these structures used to vary so widely that only a rough estimation can be given: lengths ranging from a few microns up to $50 \mu m$ have been observed; 20 and 200 nm is, on the other side, the observed diameter interval. The walls of these tubes appear to be regularly straight in some cases, irregular in others. This is not surprising since the sample, during growth, suffers from the above aggressive H atmosphere which provides a continuous etching. Abundance of very long and thin structures is generally seen at the substrate edges; here their orientation is a combination of the powder flux and the uneven cut surfaces of Si. At higher magnifications a certain degree of transparency of these structures to the electron beam has been observed even if the necessary resolution to directly see their inner structure resulted to

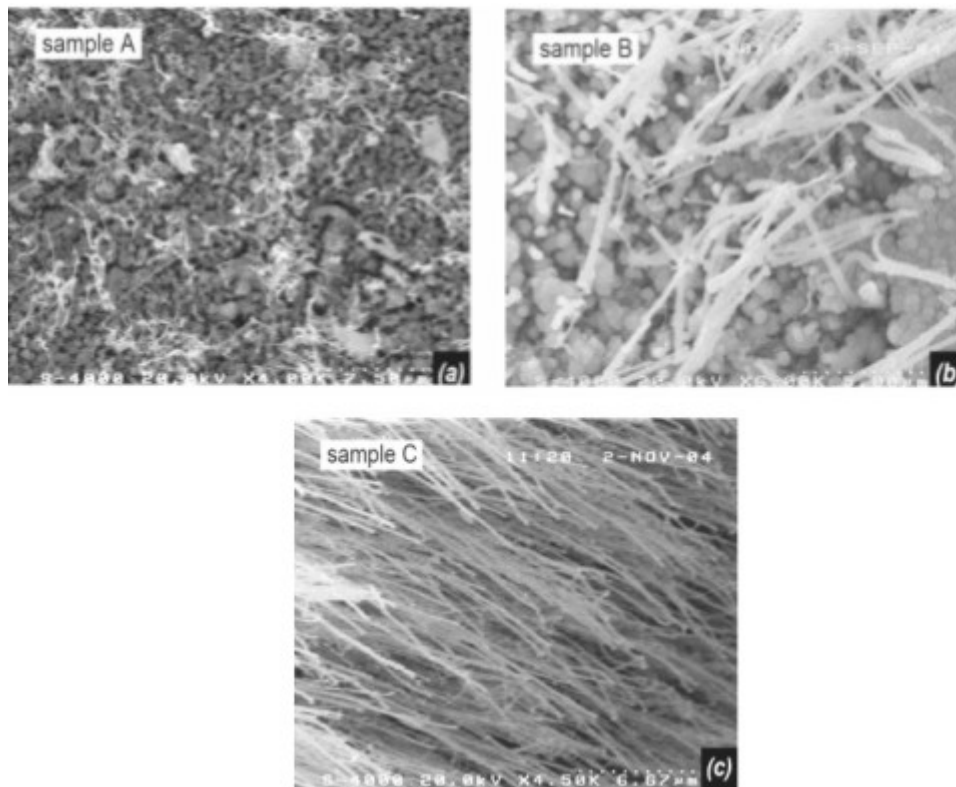


Figure 3.4: Three representative SEM images of sample A, B, C showing different morphologies.

be unattainable with our FEG-SEM. In the case of the diesel soot-grown samples, abundance of intriguing coiled structures can be observed possibly due to the action of metals and sulfur compounds [113].

As for the graphite-grown samples, SEM investigation revealed the presence of many micron-sized particles on the substrate and very few, sparse tubular structures with segmented walls. The above, large particles looked like graphite pieces because of their evident lamellar structure: this is a sign of the too large, micrometric dimensions of the powders which cannot be efficiently etched up to the formation of sp^2 -carbon clusters (see Fig. 3.2).

RHEED, Raman, high resolution TEM, STM investigations on nanopowder-grown samples [100, 108, 109, 112] have already demonstrated that the tubular

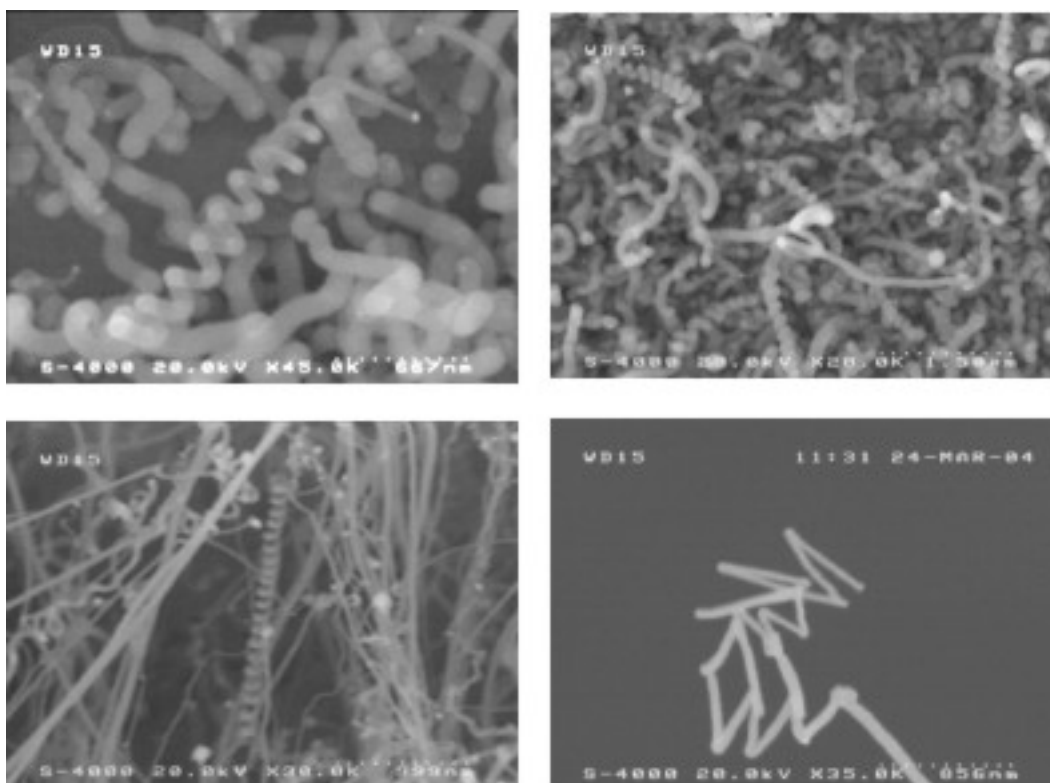


Figure 3.5: SEM images of soot grown (top left, top right, bottom left) CNT bundles. Bottom right images shows a graphite-grown CNT bundle.

structures evidenced by SEM are made up by individual SWNTs, self-assembled in bundles.

To make the following discussion clearer, a RHEED pattern got from a nanopowder-grown, SWNT sample is here reported and discussed.

Though theoretically the RHEED signal from a perfect SWNT is to appear as reflections streaked along directions perpendicular to the tube axis, when dealing with a macroscopic sample, even if roughly aligned, the overall diffraction signal generated by many, non perfectly aligned tubes is the superposition of the many individual signals thus resulting in the broadened rings of Fig. 3.6.

On the contrary, RHEED analysis on soot-grown samples shows sometimes the presence of broadened pattern due to SWNTs (Fig. 3.7, left), sometimes the pres-



Figure 3.6: RHEED pattern taken from the surface of as-deposited layers containing SWNTs.

ence of well defined, indexable rings (Fig. 3.7, right) corresponding to a graphitic structures. The same pattern as in Fig. 3.7 on the left has been obtained by graphite-grown samples.

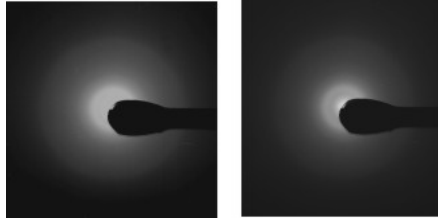


Figure 3.7: RHEED patterns taken from a diesel-grown and graphite-grown samples

This kind of signal may be attributed to any graphitic systems i.e. any structure presenting a superposition of planar graphene sheets so as to form, for example, graphite or MWNTs. In the case of soot-grown sample, being the wire-like structures the only kind of structure visible by SEM, we interpret the corresponding RHEED patterns as coming from a mixture of MWNT and SWNT arrays. In the case of graphite-grown sample, since the most abundant phase is the residual graphitic one, one cannot draw any conclusion about the SW or MW nature of the very few wire-like structures by RHEED or any kind of macroscopic characterization technique.

3.3.4 Diamond-covered SWNT bundles

As described in sec. 3.3.2, by using a reduced distance between filament and substrate (6-8 mm) and longer deposition times, a nice nanocrystalline diamond

phase on the walls of wire-like structures -SWNT bundles- was obtained. This is the first time that by a single synthesis run a hybrid material involving SWNT bundles and diamond is obtained. Deep morphological (FEG-SEM) and structural (Raman scattering, RHEED) characterization as well as careful interpretation of the obtained results has been carried out to identify without doubts the two phases and to investigate the growth mechanism [116].

3.3.4.1 Material characterization: results

By the SEM analysis of the samples (at least three for each kind) grown with different synthesis times, we could investigate the growth evolution of the nanostructures frame-to-frame. From Fig. 3.8 one observe the morphology of a series of deposits grown for 1, 2 and 6 minutes. The information gathered from this analysis highlights a number of interesting features.

First of all, it is evident that, under our experimental conditions, the process of nanotube synthesis is characterized by a very high growth rate. Fig. 3.8 reveals that, after only 1 min, nanotubes are already rather long (about $3\ \mu\text{m}$). Nanotubes are assembled in winding thin bundles (diameter $< 120\ \text{nm}$). Many unreacted carbon nanoparticles are still present at this stage.

After 2 minutes the substrate is covered by a denser deposit of assembled nanotubes, which have now reached a length of more than $10\ \mu\text{m}$. The bundles begin to align parallel each other and all evidences of residual carbon nanoparticles has gone. Fig. 3.8 shows also the smoothness of the nanotube walls and the absence of any crystalline form on them. The situation is very similar for synthesis time equals to 4 min.

After 6 minutes bundles begin to be vertically oriented and the SEM images taken at higher magnification reveal the presence of nanosized objects which, at this stage, are found preferentially on the surfaces of the larger bundles.

When the coverage is complete along the whole length of the bundles, the structures are almost all oriented at right angle with respect to the substrate. The thickness and external diameter of these tubes range approximately from 100 up to 800 nm. At higher magnifications one notes that the wires are coated by grains with dimension ranging between 20 and 100 nm, with well-defined facets.

Fig. 3.10 reports the Raman spectrum taken from one of the 15-minutes grown samples. The signal detected in the investigated low energy spectral region are associated with the radial breathing mode of SWNTs. This feature is known to

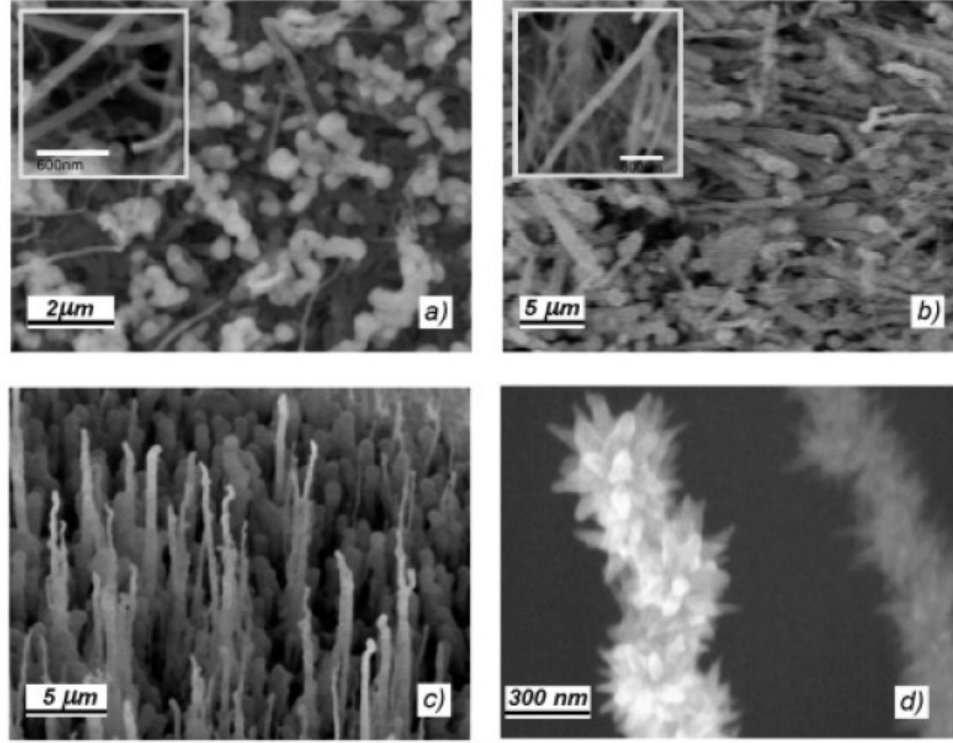


Figure 3.8: SEM images of the deposits grown for a series of deposition times: (a) 1 min; (b) 2 min. The insets of (a) and (b) show the presence, after 1- and 2-min depositions, of nanotube bundles with smooth external surfaces; (c) 6 min; (d) 6 min: a close view of a bundle coated by embryo crystallites.

represent the fingerprint of SWNTs since it is not observed in nanofiber and carbon nanowire samples.

It is also important to note that none of the spectra taken from all samples show the typical Raman signature of diamond at 1332 cm^{-1} . This is not unexpected because others have shown that a high degree of surface hydrogenation can drastically reduce Raman emission efficiency for the diamond phase [114]. Moreover, it must be considered that Raman signal is in part function of the volume of the sampled material: here the diamond volume is only a small fraction. Therefore, although Raman is invaluable in identifying the presence of SWNTs, alternative techniques have to be looked for the characterization of the outer, crystalline phase.

Since RHEED electron beam can be driven to interact with the sample at a

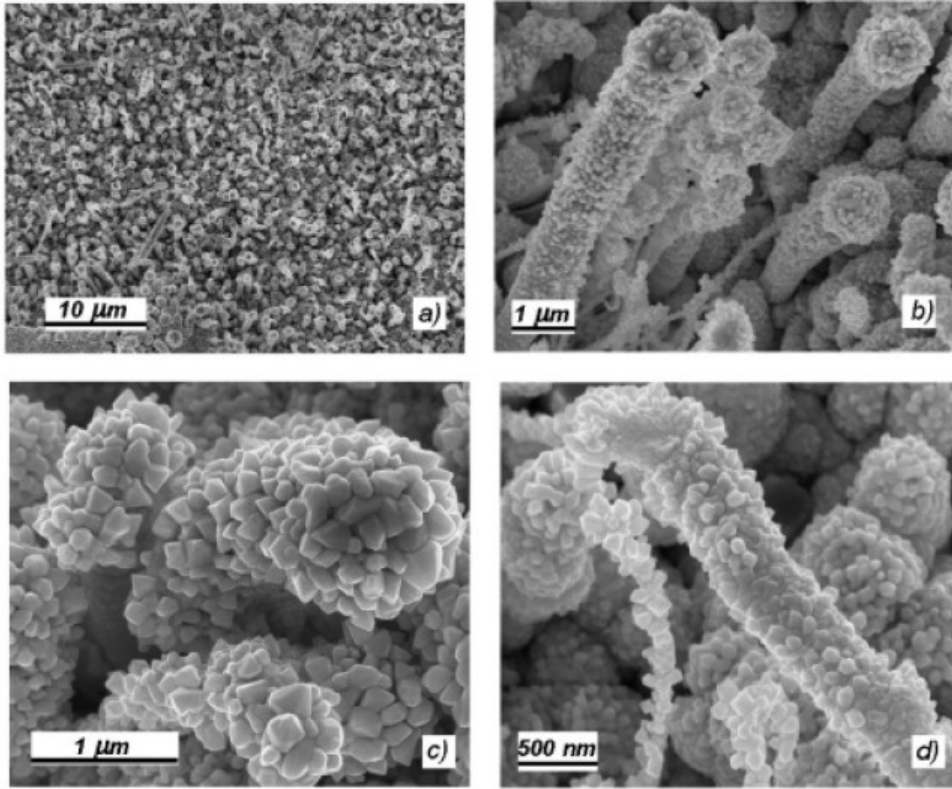


Figure 3.9: FE-SEM images showing: (a) the general view of a typical deposit; (b-d) the details of nanotube bundles covered by diamond nanocrystallites.

very glancing angle with the outermost part of the protruding deposit, RHEED patterns could provide us the desired information needed to identify the crystalline phase on the bundles walls with diamond. RHEED results have been obtained and interpreted by prof. Marco Rossi at the Dept. of Energetics, University of Rome La Sapienza.

In the case of the sample obtained with 1 minute synthesis time, the RHEED pattern was interpreted as the superposition of signals due both to randomly dispersed nanotubes and graphic nanoparticles (rings slightly elongated in the trasversal direction indicated by the arrows). On increasing deposition time to 2 minutes, the graphitic phase seems to disappear and only the signals due to the presence of SWNTs remain in the pattern. RHEED signals do not change appre-

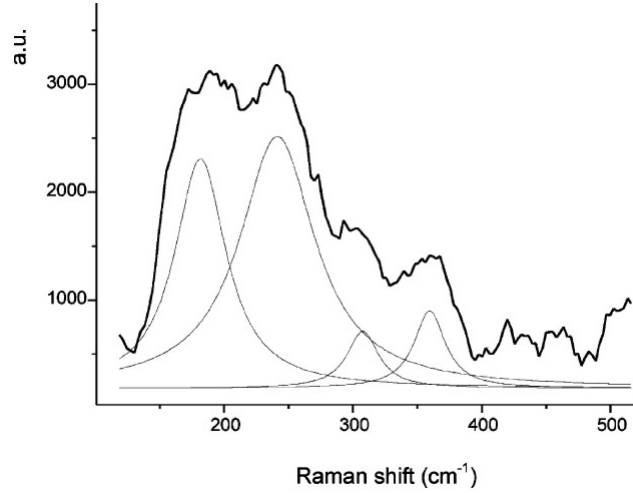


Figure 3.10: Raman spectrum in the low frequency region taken from the sample grown for 15 min. The dotted lines have been derived by curve fitting of the spectrum to Lorentzian lines.

ciably for the sample corresponding to 4 minute deposition time but an additional set of signals appear for the 6 minute deposition time sample. The net rings (it is to be noted the difference with the broad signal due to SWNTs) can be even indexed and attributed to the standard diamond lattice whereas the slight broadening can be ascribed to the nanostructured nature of the material. The features of the pattern remain unchanged for 8 and 10 minute-growing samples. Finally, for the sample grown for 15 minutes, the disappearance of SWNT feature is observed and the presence of well defined diffraction signals belonging to the polycrystalline diamond phase. The disappearance of the diffraction pattern ascribed to nanotubes as the outer phase increase in volume is due to the fact that the probed depth is expected to be within 10 nm, considerably less than the dimension of the diamond coverage estimated to be between 20 and 100 nm.

Overall, RHEED observations appear fully coherent with the information got by SEM analysis regarding the structural/morphological evolution of the hybrid system produced during the same synthesis run.

3.3.4.2 Proposal of a growth mechanism: discussion

Diamond growth onto graphitic substrates has been already reported for graphite [117] and graphite flakes [118] with proofs of a clear preference for defected regions [118] in abundance of atomic hydrogen. Keeping in mind these studies and the above results of the characterization step, we can draw a schematic process leading to the formation of these suggestive hybrid structures.

The process of nanotube growth in our synthesis conditions has been already described in sec. 3.3 as the succession of etching of the source of carbon, the self-assembly of sp^2 coordinated clusters into nanoscale graphitic flakes, followed by metal-catalyzed closing and wrapping of such nanoaggregates; as a consequence the tubular network keeps on growing by further addition of C clusters from the gas phase condensation thus making up the SWNT bundle arrays shown in Fig. At this stage the process can follow two different routes, depending on the relative abundance of atomic hydrogen. When it is -we say- low, like in normal SWNT growth experiments, the formation of nanotubes continues following the scheme described above. Otherwise the as-grown nanotubes begin to suffer from etching which cause defective sites on their walls. It has been already demonstrated that that sufficient atomic hydrogen impinging on graphitic surfaces forms C-H bonds thus locally disrupting the C-C sp^2 network and creating sp^3 defective sites that can act as nucleation sites for diamond growth [118]. A first principle study concerning the adsorption of hydrogen atoms on SWNT walls has been carried out by Barnard [119]; she illustrated that certain configurations of absorbed hydrogen may produce defects containing carbon dangling bonds and promote the formation of suitable sites for nucleation. Moreover, this site has been shown to be a low-energy adsorption sites for carbon adsorbates than for pristine sites away from the location H-induced defect. Therefore, the intriguing production of nanotube arrays coated by diamond nanograins can be rationalized if one considers that these experiments were carried out in abundance of atomic hydrogen (i.e. small distance between filament and substrate).

Moreover, SEM images show that nucleation of diamond does not occur simultaneously along the tubes, as demonstrated by by the relative dimensions of the grains at the top and at the bottom of the bundles. This difference also indicates that the H-induced defect formation process starts from the top of the nanotubes. This means that as soon as the first diamond crystallites are formed, further top-

growth of the nanotube itself is repressed and the diamond growth is the leading process. Another morphological feature to be pointed out is that the diamond nuclei do not coalesce to form a continuous film; on the contrary, diamond crystals remain hanging objects attached to their wire-like substrate via a reduced portion of their base. The orientation of diamond crystallites protruding from their substrate can be ascribed to a process of diamond nucleation that is preferentially located on the summit of relief structures generated by hydrogen etching of the nanotubes. The nucleation process is thus believed to start on prominent graphitic nodules whereas the opposite facet of the crystal is exposed to the feeding flux of carbon nanoparticles; in one observe that the gas exposed facets occur to grow faster than the less exposed bottom regions and also that the reduced radius of curvature of the nanotube acting as substrate, one can easily explain the observed morphology.

3.3.5 Selected area growth

3.3.5.1 CNT selected area growth on Fe sputtered films

As for the two methods of getting CNTs on predefined locations described in sec. 3.3.2, i.e.

1. by the use of lithographically patterned $Si/1\mu m$ thick SiO_2 substrates onto which a layer of $Fe(NO_3)_3 \cdot 9H_2O$ has been already casted;
2. by the use of lithographically patterned Fe-covered $Si/1\mu m$ thick SiO_2 substrates

being the former already optimized by Orlanducci *et al.* [109], much research work has been devoted to the setting up of the latter.

$Si/1\mu m$ thick SiO_2 commercial substrates have been photolithographically etched by F. Brunetti and R. Riccitelli from the Dept. of Electronic Engineering of University of Tor Vergata making use of the facilities in the Dept. of Physics (Tor Vergata); in the etched portions, Fe film of different thicknesses have been sputtered by M. Lucci at the Dept. of Physics (Tor Vergata). After the removal of the photoresist, the substrates have been subjected to the HFCVD synthesis with a pre-growing and growing time equals to $3 + 5$ min. Fe thicknesses of 100 nm, 50 nm 10 nm and 5 nm have been experimented. We preferred to fix synthesis conditions and vary catalyst thickness rather than the opposite because temperature,

time, distance between filament and substrate have already proved successful for all previous synthesis experiments.

100 and 50 nm thicknesses proved to be no prone to clustering. Large Fe islands with very few or no nanotubes were seen by means of FEG-SEM.

On the other side, 10 nm Fe thick substrates, after HFCVD synthesis, were reproducibly covered by dense and aligned CNTs.

5 nm Fe thickness proved to be too little: being Fe probably etched away by atomic H, almost no sign of it was seen after synthesis.

Attempt at the downscaling of the photolithographic processes for $Si/SiO_2/Fe$ multilayer realization have proven successful: features of the masks were transferred to the substrate with very good resolution and strong adhesion of the Fe film was achieved so that abundant, aligned CNT growth was observed in squares of 10 μm dimension minimum.

3.3.5.2 CNT selected area growth on a purpose-designed multilayer structure

Selected area growth of CNT constitutes the key task for CNT based device assembling so, within a close collaboration with the group of Prof. Aldo Di Carlo from Dept. of Electronic Engineering, in particular with F. Brunetti and R. Riccitelli, attempts at realizing a CNT-based triode-type device were made. Our task was to demonstrate the realizability of an integrated structure made up by predefinite cathodic areas with aligned arrays of CNT bundles, a dielectric layer, a gate and an insulating top; such device could be used as a field emission triode.

All lithographic steps are far easier to be carried out on entire wafers with smooth and clean surfaces, e.i. before HFCVD process which requires cut pieces of wafers and influences even the non-growing surfaces both in morphology and composition, so we soon realized that a complete multilayer structure had to be realized and subjected to synthesis. We decided to start from Si/SiO_2 commercial substrates and to use Nb as gate metal because of its high melting point, low diffusivity, slow carburization kinetics and the possibility of performing its surface electrochemical anodization. A $Si/SiO_2/Nb/Nb_2O_5$ patterned multilayer structure was to be therefore realized. Before designing an *ad hoc* mask, we checked the feasibility and the survival of such structure to HFCVD process. F. Brunetti and R. Riccitelli carried out and optimized the entire photolithographical process. For simplification's sake, the deposition of the Fe film was avoided, at first:

since no growth on Nb_2O_5 is expected (see sec. 3.3.2), $Fe(NO_3)_3 \cdot 9H_2O$ acetone solution was used as catalyst.

The key point in the survival of the entire multilayer structure proved to be the final cooling down: abrupt cooling used to wrinkle the upper Nb/Nb_2O_5 layers, even delamination was in some cases observed. By taking 30-40 min cooling, thermal damages were avoided.

Another difficulty was constituted by the depth of the patterned features: unfavourable orientation of the holes with respect to the nozzle lead to poor growth due to . Particular care had to be therefore paid in choosing the right configuration of the hole/holes, nozzle, filament.

However, very good results were obtained: abundant and aligned growth in the predefined locations was observed by FEG-SEM while survival of the multilayer structure was achieved.

3.3.5.3 Selected area growth of nanodiamond-covered CNTs

Sputtered Fe film having a thickness of 10 nm proved to perfectly replace $Fe(NO_3)_3 \cdot 9H_2O$ acetone solution casted onto the substrates, so it has been straightforward to use patterned $Si/SiO_2/Fe$ substrates to achieve selected area growth of diamond-covered CNTs (see sec. 3.3.2 and sec. 3.3.4).

By the setting up filament/substrate distance to 6 mm and pre-growing + growing times to 3 + 8 min, regularly spaced diamond-covered SWNT bundles of 500 nm diameter and up to 10 μm length have been obtained (see sec. 3.13).

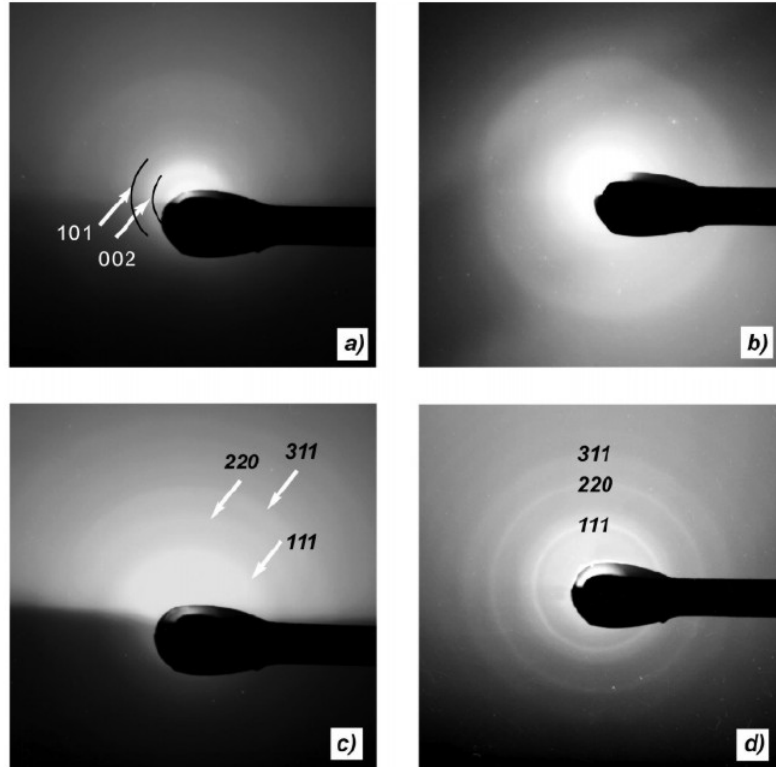


Figure 3.11: RHEED patterns of samples taken from the deposition processes lasting 1 min (a), 2 min (b), 6 min (c), and 15 min (d). The images have been taken in the typical configuration used for RHEED analysis. The white arrows indicate: in (a) the diffraction rings produced by the presence of graphitic nanoparticles; in (c) the diffraction signals belonging to the diamond lattice; the indexing for the observed Debye's rings is also reported.

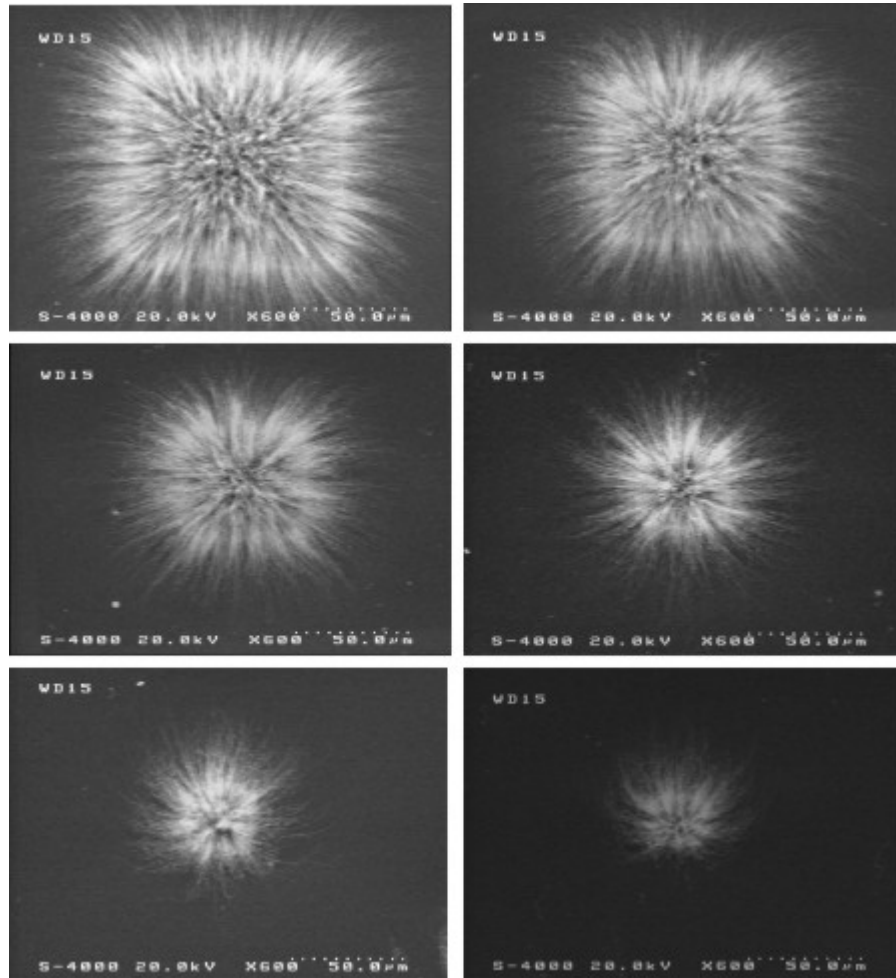


Figure 3.12: SEM images with the same scale (see all right bottom corners) showing some details of a selected area growth sample. The growth was obtained by means of a 10 nm sputtered Fe film onto a Si/SiO₂ substrate.

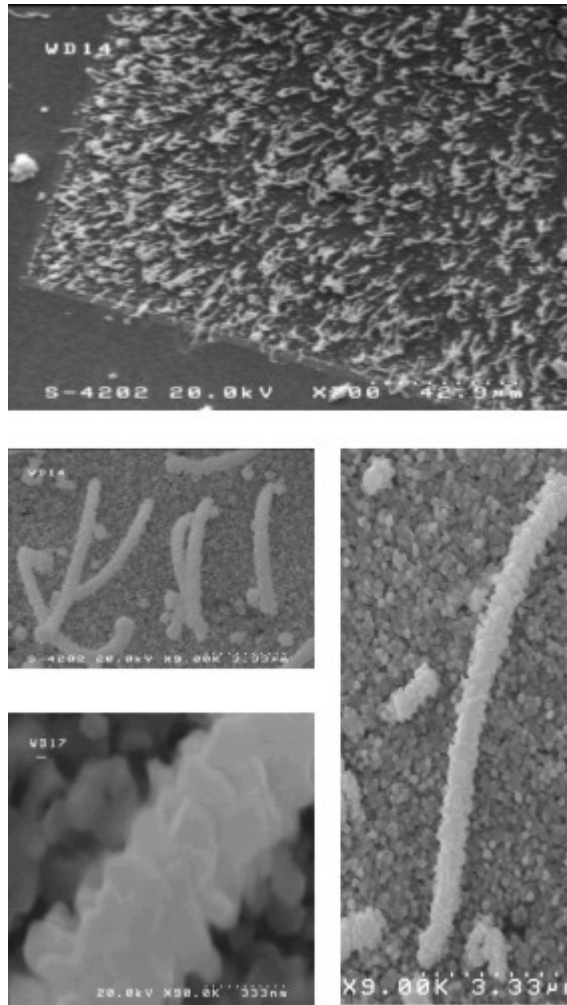


Figure 3.13: SEM images of diamond-covered SWNT sample grown on a patterned $Si/SiO_2/Fe$ substrate.

Chapter 4

Experimental: field emission I-V characterization

4.1 Field emission apparatus at Tor Vergata

The experimental work described in this thesis began from the test of a home-made field emission apparatus built at the Department of Chemical Sciences and Technologies by Dr. Vito Sessa with the collaboration of Ing. Alessandro Ciorba.

Roughly, field emission I-V investigation requires the measurement of a current between two counterfacing electrodes (the anode, here called probe, and the cathode, i.e. the investigated sample); though a simple set up can be imagined, the need for a good level vacuum and high voltage supply introduce some difficulties.

The measurement set up must satisfy two mandatory requirements:

- vacuum requirements: pumps, valves, gauges, connections;
- high voltage power supply and current measurement circuit.

Our set-up display an optional requirement:

- probe (z direction) and sample (x, y directions) micro-movement system.

The core of our system is a stainless steel chamber with a number of flanges to allow evacuation of air, measurement of pressure, electrical contacts, anode-cathode movement system. The chamber is evacuated by a turbo-molecular pump with a

rotative pump in series so that the lowest achievable pressure is of the order of 10^{-7} mbar.

The sample x, y micro-movement system is made up of two crossed linear translators, connected to the outside by two flexible shafts and driven by two knobs. The travel range is 18 mm, with a minimum incremental motion of 1 μm .

The probe (anode) consists of a steel ball, with diameter of 1.4 mm; and it can move along the axis by means of a high resolution linear actuator, endowed with a theoretical 0.059 μm resolution. The actuator is provided with a DC motor driven by a PC via RS-232 through a controller whose minimum incremental step is 0.1 μm .

The power supply and measurement system is composed of a high voltage source, a picoammeter and a protection resistor.

The high voltage source can deliver a maximum current of 3 mA, when the maximum output voltage is limited to 3 kV (1 mA up to 8 kV).

The picoammeter is a Keithley 6485, with $5\frac{1}{2}$ digits and current range from 1 nA -10 fA resolution- to 20 mA -100 nA resolution-. Picoammeter maximum input voltage is 220 V: in order to work with higher voltages, a series resistor is added to the circuit because, even if field emission measurements are carried out in a non contact mode, an accidental short or a discharge at higher voltages would lead to irreversible failure. First 500 $M\Omega$, then 100 $M\Omega$ protection resistor was inserted to allow us to supply up to 10000V (in the case of 500 $M\Omega$) or 2000 V (in the case of 100 $M\Omega$) and limit the short circuit current to 20 μA . Keithley picoammeter is driven by PC via RS-232, too.

The control of z motion and data acquisition has been made through a purpose realized software (LabVIEW) by Ing. Alessandro Ciorba.

A close collaboration with Ing. Alessandro Ciorba made it possible to optimize the data acquisition software through which it is possible both to keep constant voltage and vary anode-cathode distance and to keep distance fixed and vary voltage. Current as a function of time can be recorded as well.

The effective anode-cathode distance is determined via the measurement of the anode-cathode capacitance using a LCR-meter (Stanford Research SR715 model).

All fits are carried out by means of Microcal Origin 6.0.

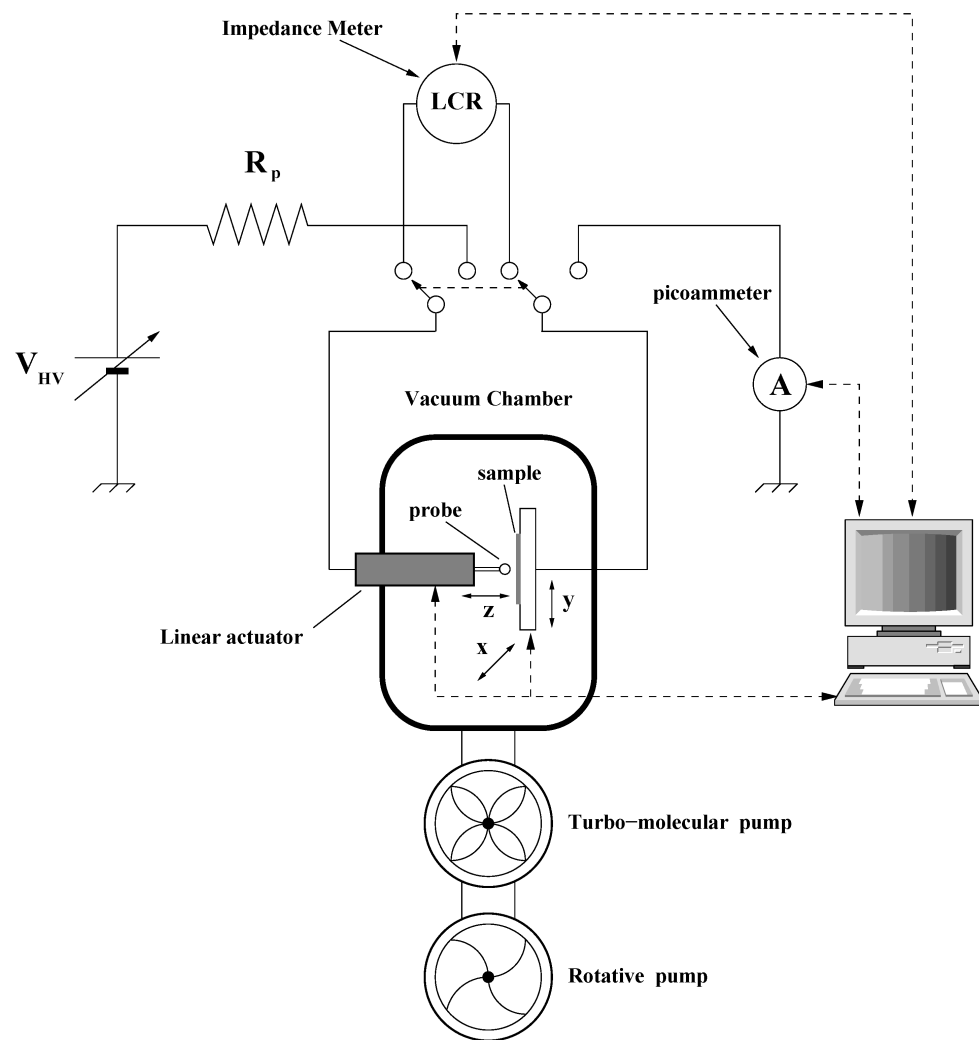


Figure 4.1: Scheme of the field emission set up at the Dept. of Chemical Sciences and Technologies, Univ. Tor Vergata

4.2 Setting up of a reliable measurement methodology

Though the experimental apparatus for field emission investigation is conceptually simple, the setting up of an accurate methodology for data analysis is not very straightforward (see sec.1.4). Extraction field (for a given current) and current density (for a given applied field) are the technological relevant parameters and those used to compare different samples. Their evaluation makes use of the precise measurement of anode-cathode distance and emitting area calculation.

4.2.1 Anode-Cathode distance evaluation

In order to measure the anode-cathode distance in a sphere-to-plane configuration, we propose here a capacitive method, allowing us to avoid any mechanical contact which could alter and eventually damage the cathode surface. We decided for the capacitive technique counting on its high sensitivity; it is to be noted, however, that this methodology cannot be used in a plane-to-plane geometry, because, in such configuration, capacitance diverges too fast as the electrodes approach. Moreover, in the range of inter-electrode distances currently used as separation in our field emission measurements (10-100 μm), such capacitive approach possesses the micrometric sensitivity necessary for the precise determination of the electric field E .

The capacitance between a sphere and a plane is described by [83]

$$C \propto 2\pi\epsilon R \left(\ln \frac{R}{d_0} + k \right) \quad (4.1)$$

where the radius R and the distance d_0 are defined in Fig. 4.2, and k is a constant, taking into account the surface roughness. This equation holds for $d_0 \ll R$.

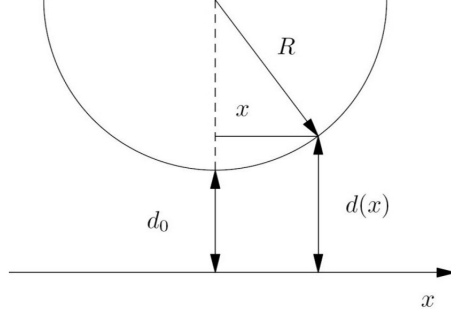


Figure 4.2: Scheme of the sphere-to-plane measurement set up with the definition of some useful variables

The capacitance variation corresponding to a distance variation results to be

$$\Delta C = \frac{\partial C}{\partial d_0} \Delta d = 2\pi\epsilon R \left(-\frac{1}{d_0} \right) \Delta d \quad (4.2)$$

With our instrumental parameters, at a distance of about $10 \mu m$, we got $\Delta C \approx 0,005 pF$, a value which is fully compatible with the accuracy of the instrument. For clarity sake, the process through which we set up the distance evaluation methodology is described in 3 steps.

1. First of all, we verified the validity of eq. 4.1 for our geometrical set-up. With this purpose, we used a mirror polished, flat metal plane. After finding $d_0 = 0$ by means of successive movements of the anode toward the cathode until the electric contact was achieved, we built the curve of capacitance vs. distance. As shown in Fig., given R the value of $750 \mu m$, eq. 4.1 fitted perfectly the experimental data up to the zero point. Several experiments, performed under the same conditions, proved that the curves were highly reproducible both in approaching the two electrodes than in getting them farther. However, we noted that after each turning off the instrument and/or recalibrating it (the capacitance-meter requires a calibration at each starting up), the curves translated rigidly up or down with respect to the y (capacitance) axis with an excursion of $0,2-0,4 pF$. That has been ascribed to an imperfect subtraction of the parasitic capacitance by the instrument when turning it on. This inconvenient prevented us to construct a kind of universal capacitance-distance curve i. e. a curve able to automatically give

us the distance at a given capacitance value. Anyway, we went on with our investigation.

2. Keeping in mind that our goal was to measure distance without contact and observing that the zero point is a discontinuity (asymptote) for $C(d_0)$, we verified that the fits were also good without those experimental points closer than $10 \mu m$ to the zero point. In Fig. 4.3 right it is shown the same curve as Fig. 4.3 left, without the first points closer than $10 \mu m$ to the electrical contact. The fit was satisfactory.
3. Third step was to forget about the real distance got by electrical contact and replace the x-axis in microns with the arbitrary unit (steps) -which we called x - given by the actuator. As a consequence we set

$$d_0 = x - x_0 \quad (4.3)$$

where x_0 is the unknown position of the zero point. The fit of the experimental data (C, x) with the function

$$C = 2\pi\epsilon R \left(\ln \frac{R}{d_0} + k \right) \quad (4.4)$$

where R was known ($750 \mu m$) and x_0 and k were treated as unknown parameters, was satisfactory (see Fig. 4.4).

After substituting the mirror polished metal plane with a SWNT-covered sample, we repeated point 1, 2, 3 and verified that also for highly rough surfaces eq. 4.4 can be applied. Fig. 4.6 reports a typical curve obtained for a medium-density SWNT sample. To resolve any doubts, after the fit with eq. 4.4 through which we extracted x_0 , we always checked the position of the surface with the electrical contact method. Discrepancies of no more than $10 \mu m$ were found.

This method can be also successfully used for those thin films of highly insulating materials on conducting substrate whose resistance makes it impossible to use the electrical contact method. An example of C - x curve with a fit for a CVD diamond film on a Ti substrate is shown in Fig. In this case, the distance evaluated by the method doesn't take into account the presence of a film of dielectric. The error is not that much, as it is explained in the following example.

Here, we'll consider the much simpler case of a plane capacitor where one of the two plates is covered by a thin (compared to the plate distance) film of insulating

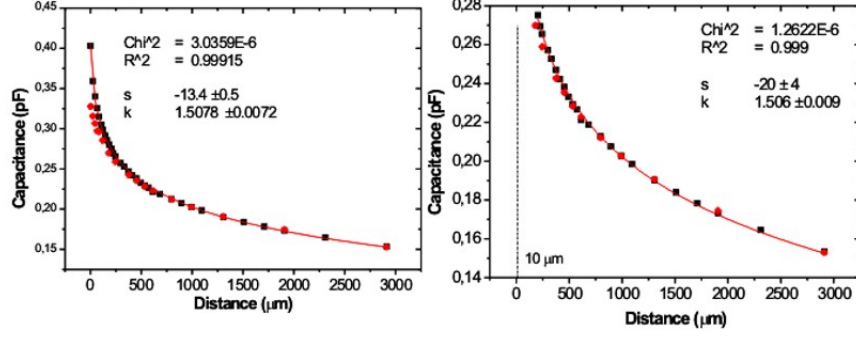


Figure 4.3: Two different capacitance vs. distance curves (only one of them is fitted) taken for a stainless steel plane as described in previous point no. 1 and no. 2: from electrical contact (left), removing the first points (right). The equation used into the fit was $C = 2\pi\epsilon R \left(\ln \frac{R}{d_0 + s} + k \right)$ where s has been introduced to take into account the uncertainty on the zero position. Each point is the average of ten successive measurements. Standard deviation is not shown because it is too little to be drawn.

material (see Fig. 4.7).

Requiring that capacitance for the above system is equal to the capacitance of a equivalent capacitor with only vacuum between its plates, it must be that

$$C(d_{12}) = \frac{S_1 \epsilon_2}{d_1 \epsilon_2 + d_2 \epsilon_1} = \frac{S \epsilon_0}{d} = C(d) \quad (4.5)$$

where d_1 and d_2 are illustrated by the above figure; ϵ_1 , ϵ_2 are, respectively, the relative dielectric constants of the *media* filling the regions indicated with d_1 and d_2 ; ϵ_0 is the vacuum permittivity; S is the surface area of both plates. Solving eq. 4.5 with respect to d lead to

$$d = \frac{d_1}{\epsilon_1} + \frac{d_2}{\epsilon_2} \quad (4.6)$$

If one considers $\epsilon_2 = 1$ as the vacuum relative permittivity; $\epsilon_1 = 5,5$ as diamond relative permittivity; $d_2 = 100\mu m$ and $d_1 = 5\mu m$, it results that the committed error in taking d as the actual distance between the two plates is of the order of 1%.

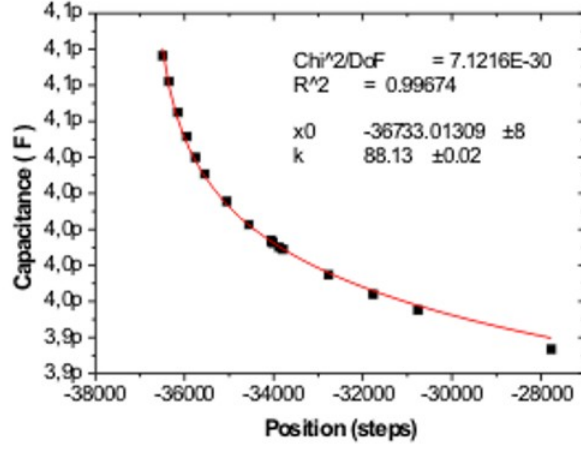


Figure 4.4: A typical capacitance vs. distance (in steps) curve taken on a stainless steel plane as described in point no. 3. Each point is the average of ten successive measurements. Eq. 4.4 was used in the fit.

4.2.2 Emitting area evaluation

We propose here a simple method which is, to our knowledge, the first analytical approach for the case of a sphere-to-plane anode-cathode configuration. It considers the total current coming out from the sample area where the applied electric field is quoted enough high to allow nanotube emission.

To better explain the following discussion, a scheme of the sphere-to-plane system is illustrated in Fig. 4.2.

Our plane-to-sphere geometry generates an electric field decreasing quickly with the distance x from the axis of the system, as shown by the field map in Fig. 4.8.

For convenience' sake we recall here the Fowler-Nordheim law:

$$J(F) = \frac{e^3}{8\pi\hbar} \frac{\beta^2 F^2}{\phi} \exp \left[-\frac{4\sqrt{2m_e}}{3e\hbar} \left(\frac{\phi^{3/2}}{\beta F} \right) \right] \quad (4.7)$$

where e and m_e are, respectively, the charge and the mass of the electron, \hbar the Planck constant, F the applied electric field, ϕ the workfunction and β the electric field-enhancement factor. The exponential dependence of current density

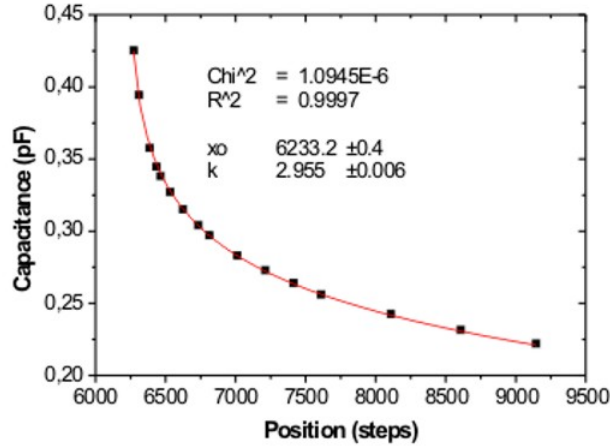


Figure 4.5: Capacitance vs. position curves taken on a SWNT sample as described in point no. 3. The electrical contact was set at 6071 steps, while the fit gives 6233 as the zero point: $8 \mu m$ is, in this case, the difference between the two methods.

upon electric field makes the current density significantly different from zero only in the nearby of the axis as it is shown in Fig. 4.9 where the lateral behaviour of the field and of the emitted current are compared (after normalization to 4 to make easier their comparison).

In order to evidence the dependence on x of the applied field, we re-wrote the Fowler-Nordheim law

$$J(x) = a_1 F^2(x) e^{-a_2/F(x)} \quad (4.8)$$

where a_1 and a_2 lump the characteristics of the material (workfunction and field enhancement factor).

The very fast decay of the current density with the distance x from the axis allows us to approximate the electric field $F(x)$ within that zone as the applied voltage V divided by the plane to sphere distance $d(x)$ (see Fig. 4.2).

Within such framework, we assume a negligible average roughness of our samples. This approximation is justified when the interelectrode distance is more than one order of magnitude larger than the sizes of the surface protrusions and, in our case, it is still acceptable up to an anode-cathode distance of $50 \mu m$. More-

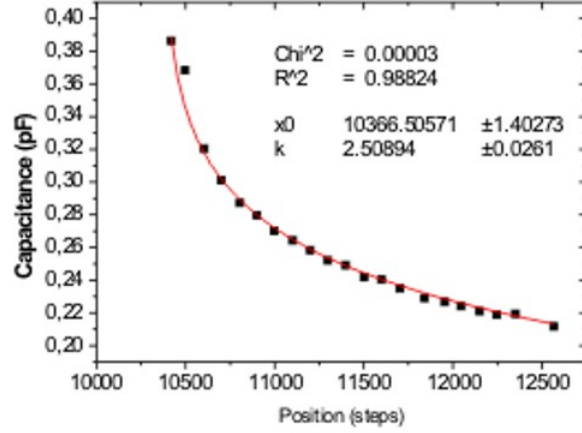


Figure 4.6: Capacitance vs. position curves taken on a HFCVD-grown diamond sample on Ti.

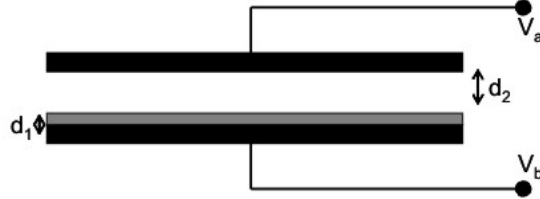


Figure 4.7: Scheme of a plane capacitor with a plate covered by a thin film of an insulator

over, we experimentally verified that the flat cathode approximation is valid when considering the system acting as a capacitor (see sec. 4.2.1).

Within the limit $x \ll R$, $d(x)$ can be approximated by:

$$d(x) \simeq d_0 + x^2/2R \quad (4.9)$$

so that the electric field becomes

$$F(x) \simeq \frac{V}{d_0 + \frac{x^2}{2R}} \quad (4.10)$$

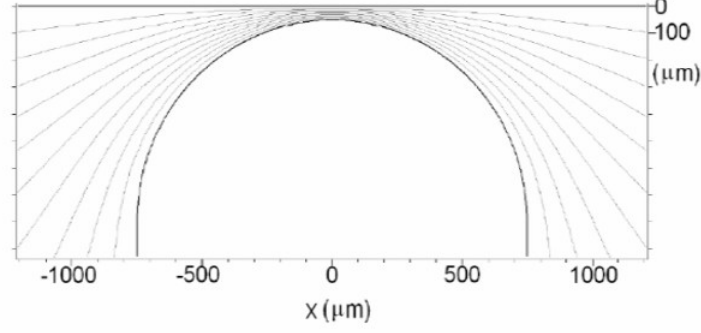


Figure 4.8: Simulation of the electric potential map within our system, obtained with POISSON 6

This expression occurs to match very well the exact expression [121] and the numerical result of our simulation in the nearby of the axis of the system. The combination of eq. 4.10 and eq. 4.8 leads to

$$J(x) = a_1 \frac{V^2}{\left(d_0 + \frac{x^2}{2R}\right)^2} e^{-\frac{a_2}{V} \left(d_0 + \frac{x^2}{2R}\right)} = a_1 \frac{V^2}{d_0^2} e^{-\frac{a_2 d_0}{V}} \left[\frac{1}{\left(1 + \frac{x^2}{2Rd_0}\right)^2} e^{\frac{a_2 x^2}{2RV}} \right] \quad (4.11)$$

The above equation shows clearly that the current density drops down away from the axis with a Gaussian tail whose variance is $\sigma = RV/a_2$.

To get the current I , now, the integration of eq. 4.11 over the whole plane is needed so that, considering the axial symmetry of the system, a simple calculation can be carried out

$$I = \int_0^\infty J(x) 2\pi x dx = a_1 \frac{V^2}{d_0^2} e^{-\frac{a_2 d_0}{V}} \left[\int_0^\infty \frac{1}{\left(1 + \frac{x^2}{2Rd_0}\right)^2} e^{\frac{a_2 x^2}{2RV}} 2\pi x dx \right] \quad (4.12)$$

The expression inside the square brackets can be indicated as the effective emitting area A_{eff} so that eq. 4.12 can be shortened as

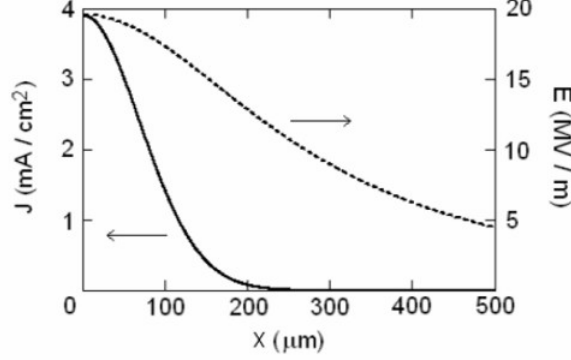


Figure 4.9: Lateral behavior of current density (left axis) and electric field (right axis).

$$I = J(0) \cdot A_{eff} \quad (4.13)$$

where $J(0)$ is the current density at $x = 0$ and A_{eff} the effective emitting area. This latter quantity can be calculated as follows.

For convenience' sake, we define A_2 -the β containing parameter- as

$$A_2 = d_0 a_2 \quad (4.14)$$

then, after substituting it into the relation for A_{eff} , we get

$$A_{eff} = \int_0^\infty \frac{1}{\left(1 + \frac{x^2}{2Rd_0}\right)^2} e^{\frac{A_2 x^2}{2RVd_0}} 2\pi x dx \cong \int_0^\infty \left(1 - \frac{x^2}{2Rd_0}\right) e^{\frac{A_2 x^2}{2RVd_0}} 2\pi x dx \quad (4.15)$$

where, for the term in brackets, a first-order Taylor expansion has been performed and an integration interval extended from the axis of the system (namely 0) and a very long lateral distance from it (namely ∞) is set up. By solving the integral, a simple formula for the effective area can be derived

$$A_{eff} = \pi \left(\frac{2d_0 RV}{A_2} \right) \left(1 - \frac{2V}{A_2} \right) \quad (4.16)$$

A_{eff} occurs, therefore, to increase with the experimental parameters d_0 and V (the field “illuminated” area increases as the electrodes get far away and/or the field increases) and to decrease as A_2 increases. A_2 parameter is directly linked to the β enhancement factor as it will be explained in the following.

Substitution of eq. 4.16 into eq. 4.13 lead to the expression of current as a function of voltage (the two experimentally measured variables)

$$I = J(0)\pi \left(\frac{2d_0RV}{A_2} \right) \left(1 - \frac{2V}{A_2} \right) = A_1 V^3 \left(1 - \frac{2V}{A_2} \right) e^{-A_2/V} \quad (4.17)$$

where A_1 has been defined as

$$A_1 = a_1 \pi \frac{2R}{d_0 A_2} \quad (4.18)$$

Practically, the emitting area evaluation can be carried out in the following simple steps:

1. measurement of I-V field emission characteristic;
2. measurement of d_0 with the capacitive method explained in sec. 4.2.1;
3. fit of the experimental curve with eq. 4.17 and extraction of A_1 and A_2 parameters;
4. choice of a voltage value and calculation of A_{eff} through eq. 4.16.

Extraction of β value can be easily carried out by means of eqs. 4.14 and 4.8. It results to be:

$$1/\beta = \frac{A_2}{\left(d_0 \frac{4\sqrt{2m\epsilon}}{3e\hbar} \phi^{3/2} \right)} = \frac{A_2}{d_0 \phi^{3/2} (6,83 \cdot 10^9 V \cdot m^{-1/2})} \quad (4.19)$$

As A_2 is directly proportional through d_0 to a_2 (see eq. 4.14), it inversely resembles the material β enhancement factor. To link eq. 4.16 with eq. 4.19, one can easily say that as β increases, A_{eff} increases too, because local field enhances. For high values of A_2 values, moreover, the term in brackets of eq. 4.17 can be approximated to 1 and, by taking the logarithm of the non-exponential term, eq. 4.17 can be rewritten as:

$$\ln \frac{I}{V^3} \propto \frac{A_2}{V} \quad (4.20)$$

That means that under the validity of the above approximations, the sphere-to-plane configuration leads to a modification of the conventional relation of the Fowler-Nordheim plot (see sec. 1.3 and eq. 1.26).

Since the emitting area evaluation is a critical and controversial matter (see sec. 1.4.3), some comments about the validity and limits of our calculations are needed.

First, it is to be noted that, when working with macroscopic samples (arrays of nanotubes), the observed I-V curve is the sum of many individual curves and the extracted data are statistically averaged parameters. In particular, the extracted β value is averaged among all emitting nanotube and suffers from 2 effects:

- since field emission is a tip effect, it is to be expected that even applying high voltage to a macroscopic SWNT sample, only the thinnest and most protruding tips will emit,
- screening effect due to field shielding of adjacent nanotubes (see sec. 1.4.1.2)

As a consequence, the *real* emitting area is restricted to a few thin, long and ideally unshielded nanotubes.

Secondly, among the different emitting area definitions presented in Chapter 1 (see sec. 1.4.3) and here recalled:

1. the area got by using the intercept of the Fowler-Nordheim equation called *FN emission area*;
2. the observed area of the emitter tip;
3. the area of the emitter at its base, called here area of the emission site;
4. the area of the entire cathode (in the parallel plane geometry),

the one evaluated by this method is more related to area no. 4 (referred to a sphere-to-plane geometry) than to the others. More explicitly, the area quoted by this approach is the one where the applied field is high enough to enable the present nanotubes -if endowed with the extracted (eq. 4.19) β value- to emit. It is a technological relevant parameter in the sense that it allows us to say that, at the doubling of the size of the spherical anode, the current should theoretically double.

4.3 Field emission I-V investigation on SWNT-based samples

Since there aren't standard samples in field emission, many SWNT and metallic samples (Cu, Nb, Pt) were investigated in the field emission set up to test the apparatus itself and the measurement conditions/methodology. Even a mirror-polished metal plane endowed with a known workfunction cannot be considered a field emission standard for two basic reason:

1. the needed field to start field emission from a metal is typically few V/nm: the lack of field enhancement protrusions requires the application of several kilovolts and/or the placement at a very short cathode-anode distance. These are the conditions of many kinds of vacuum discharges, above all at medium vacuum level;
2. atomically flat surfaces are, in this conditions, ideal abstractions: a nominally flat surface at medium vacuum level displays many protrusions due to gas adsorption. Actually no surface can show $\beta = 1$.

Moreover, field emission apparatuses are such that the obtained results depends strongly on the geometrical configuration, the vacuum level and quality, the pre-treatment of the sample, the protection resistance so that even the same sample can give different results when measured with different set-ups. Within this framework, comparisons among different set-ups are extremely difficult while comparison of different samples measured in the same conditions does have sense.

The first step in testing our field emission set up was, therefore, to acquire the needed sensitiveness to control the measurement process and recognize unforeseen, undesired events (see sec. 4.3.1) and then to characterize the critical experimental parameters (due to measurement conditions and/or features of the samples) affecting results (see sec. 4.3.2). Then a measurement procedure is set up (see sec. 4.3.3) so that a quantitative analysis is carried out.

4.3.1 Role of vacuum

It has been widely recognized in literature and then experimentally tested during this three-year work that I-V curves are theoretically smooth but experimentally noisy and non-reproducible at first, in a medium vacuum environment. It has been

experienced that a good level and good quality vacuum is needed to get reasonably smooth and reproducible I-V curves. Fig. 4.10 shows some really bad I-V curves taken at the low vacuum level of 10^{-5} mbar on a SWNT sample.

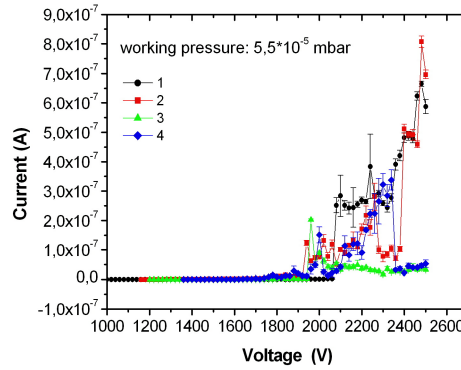


Figure 4.10: Typical I-V field emission curves from a SWNT sample grown on Si, exposed to a low vacuum level (protection resistance $500\text{ M}\Omega$).

Several phenomena are usually observed when increasing the voltage between two electrodes in poor vacuum conditions. Residual gas conduction lead to different kinds of discharges (see sec. 1.7.1) i.e. sparks characterized by high current density which cause morphological changes at the surface. Many times it is nearly impossible to detect these discharges except from measuring a higher emitted electron current. Such phenomena are helped by desorption of gas from the cathode or simply diffusion on the surface, removal of dusty impurities on the surface, detachment of small pieces of sample if not strongly adhering to the substrate. Better vacuum conditions then 10^{-5} mbar are therefore required as well as a particular cleanliness of the chamber.

4.3.2 Role of conditioning process

As for the improvement of the samples' performance, the choice has been focused to those samples whose surface did not evidence the presence of removable impurities. Our policy was to test macroscopical SWNT samples at medium vacuum level in order to possibly propose them as cathodes in a field emission device but, since adsorption is an unavoidable process in these conditions, a conditioning process

has been set up to limit adsorbate-driven current instabilities.

In accordance with literature (see sec. 2.1.2.2), it has been found that current stability and I-V reproducibility improve after repeatedly sweeping up and down voltage and/or keeping the sample at a fixed, high voltage -emitting current of about $1 \mu A$ - for a while (30 minutes-2 hours). Two proofs of such phenomena are given in the following graphs.

High non-reproducibility of sample response was at first observed in all cases (Figs 4.12 and 4.11 are only two examples). Fowler-Nordheim plots (in the insets) proved to be curved at high voltages. In going on with the sweepings, reproducibility strongly improves.

The net effect on extraction field of the so called conditioning process on the average field emission behavior of the samples is shown in Fig. 4.13, where the average of the previous I-V curves is taken.

Extraction field qualitatively increases and/or emission current decreases.

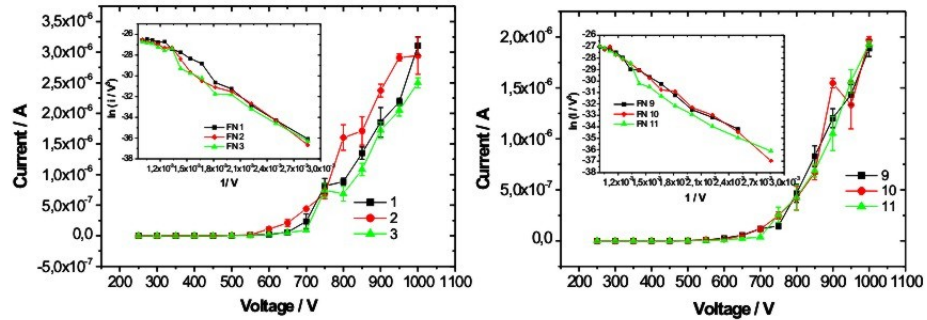


Figure 4.11: Successive I-V curves taken at the very beginning of the investigation (left) and after some other sweeps (right) from a SWNT sample grown on Si from carbon nanopowders (sample A). In the insets the corresponding FN plot (eq. 4.20) are shown. It is possible to see a significant improvement of reproducibility. Working pressure $4 \cdot 10^{-7}$ mbar.

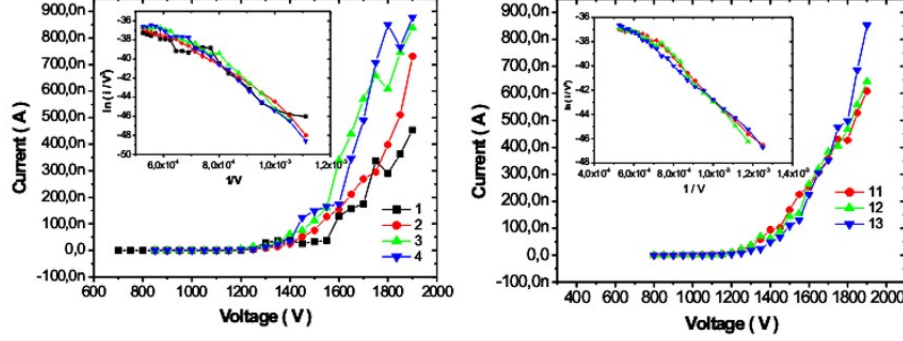


Figure 4.12: Very first I-V curves (left); successive I-V curves (right) from a SWNT sample (D) grown on Si from carbon nanopowders . In the insets the corresponding FN plot (eq. 4.20) are shown. Working pressure was $6,6 \cdot 10^{-8}$ mbar.

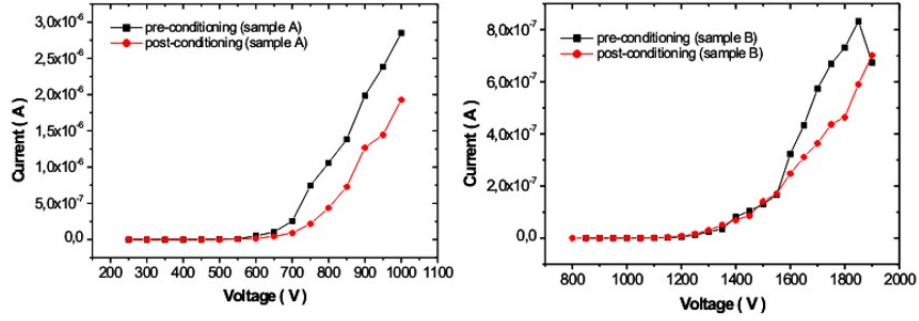


Figure 4.13: I-V curves taken from sample A (left) from the average of the previous curves: left of Fig. 4.11 corresponds to the squares (pre-conditioning), right of Fig. 4.11 corresponds to the circles (post-conditioning). On the right the corresponding, averaged I-V curved of sample D calculated from Fig. 4.12 are shown.

Occasions of non reproducibility of I-V curves, deviation from Fowler-Nordheim law and instabilities have been already described in sec. 1.6.1 and, for CNTs in particular, in sec. 2.1.2.2. Here those effects which can explain the above phenomena due to the conditioning process are recalled:

1. structural modification of the emitter due to Joule heating (irreversible mod-

ification of the sample response during the investigation session);

2. alignment of the emitter due to the applied field (irreversible/reversible improvement of emission performances: lower extraction field due to a higher β factor);
3. degradation of some emitters (irreversible worsening of emission performances);
4. adsorbed molecules -tunnel resonant emission- (reversible measurement of a curved Fowler-Nordheim plot);
5. adsorption/desorption resulting in change of the workfunction and morphology (reversible improvement/worsening of emission performances);
6. diffusion of the adsorption molecules (reversible occurring of current instabilities);

All these phenomena reasonably occur during field emission from a SWNT sample but, due to the complexity of the arrays of emitters and the competitive and often opposite effects, it is impossible to distinguish among each of them.

As for the modifications of morphological/structural features (above points no. 1-3), they must be significative and spatially extended to be detected by SEM. The emission-driven alignment of CNTs has been observed in field emission/SEM combined set-ups and has been defined both reversible and irreversible [79, 80], due to the experimental conditions. The degradation of the best emitters usually occurs because of a too large morphological difference with the others: they begin to emit alone at a very low voltage and, when their neighbours are just starting, they come up to disruption because current density has in the meanwhile become excessive. A more spatially homogeneous emission is achieved at the price of an increase of extraction voltage.

As for the effect of adsorbates (above points no. 4-6), it is well known that CNTs emit through stable adsorbate states even under ultrahigh vacuum conditions and that these adsorbate states enhance field emission current up to one order of magnitude [77].

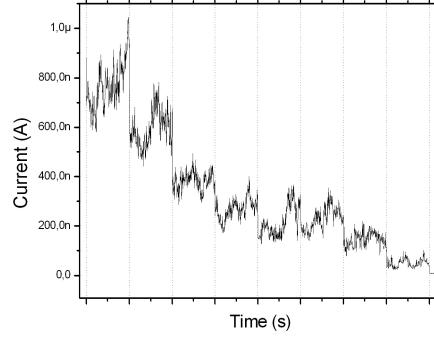


Figure 4.14: A typical downward sweep at early stage of the conditioning process (sample E). Each vertical line correspond to a -100 V step.

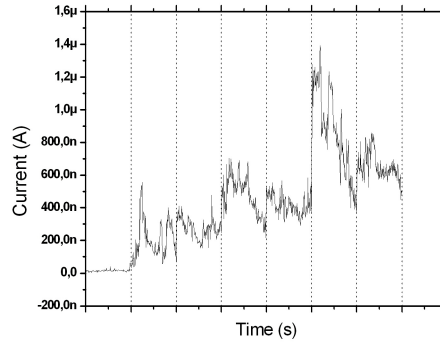


Figure 4.15: A typical upward sweep at early stage of the conditioning process (sample F). Each vertical line correspond to a +100 V step.

Loosely bound adsorbates are reversible removed by increasing voltage (i.e. increasing current, thus heating): the phenomenon can be followed by observing the time evolution of an I-V. During the up sweep (see Fig. 4.15), the current decreases over time between voltage steps; during the down sweep (see Fig. 4.14), as adsorbate reoccupy their configurations, electron tunneling enhances.

Most of these loosely bound adsorbates can be effectively removed by continuously sweeping up and down applied voltage. In this regard, we demonstrate that,

even if the reported I-V curves may be not completely due to the intrinsic properties of SWNTs, it is possible to achieve a satisfactory reproducibility and current stability through a careful conditioning step. Strongly bound adsorbates may be rearranged into the so-called Taylor cones (see sec. 2.1.2.2). Desorption, heat-driven diffusion and field-driven rearrangement lead all to a more stable configuration of the emitter surface resulting in a more stable emission.

The good current stability and response reproducibility achieved through the conditioning process is a must for the proposal of such materials as cathodes for a future field emission device. Last but not least, it is worthwhile noting that survival to these medium vacuum conditions is the first great advantage of CNT emitters over conventional metallic/semiconducting tips. The integrity of the samples was checked by SEM after each measurement session.

4.3.3 Measurement procedure

The full measurement procedure set up during this three-year work consists of the following steps.

1. After calibrating the capacitance meter, the position of the sample surface is found out through the method described in sec. 4.2.1.
2. The anode-cathode position is adjusted as to get a measurable current (1 nA) at 500-800 V. This enables us to measure a wide I-V curve in the voltage window of 0-2000 V without applying excessive applied field.
3. The conditioning process is performed. It consists of successive up and down sweeps (depending on the age of the sample and the presence of removable dusty impurities on the sample surface, it usually took from two hours to more than 2 working days) is performed.
4. Once achieved a satisfactory reproducibility of sample response, a series of successive I-Vs (at least three) are taken so as to calculate an averaged I-V curve. The Fowler Nordheim plot is calculated to roughly check the obedience to Fowler Nordheim law.
5. The fit of the averaged curve with eq. 4.17 is performed in order to extract A_1 and A_2 parameters. Emitting area can be now evaluated. These quantita-

tive parameters are then listed: extraction field (for 1 nA current), current density at a given field, value of the β enhancement factor.

6. Investigation on different sample's points is carried out to see if field emission behavior is homogenous or not.
7. Current stability as a function of time is occasionally measured.

4.3.4 Morphologically different SWNT samples: results and discussion

Field emission investigation on morphologically different samples has been carried out to link morphology and emission performance. Results got from three significantly different samples will be here presented.

Fig. 4.16 is shown as an example of the achieved reproducibility of field emission performance from sample B after conditioning.

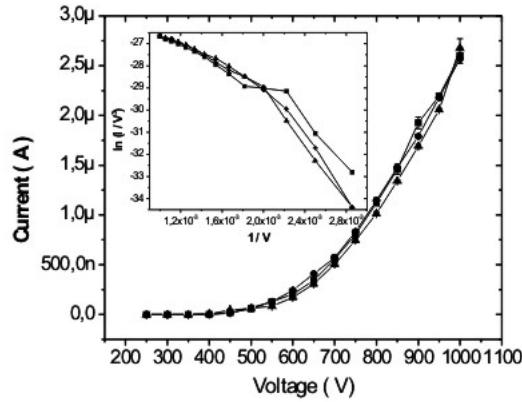


Figure 4.16: Three successive I-V curves from sample B after conditioning. The Fowler-Nordheim plot is shown in the inset.

Once got at least three successive I-V curves from sample A, sample B, sample C (whose morphology has been already shown in Fig. 3.4), the average with its relative standard deviation is taken. The fit with eq. 4.17 is then carried out. Results are shown in Fig. 4.17.

Experimental and fit-extracted data are displayed in Tab. 4.2.

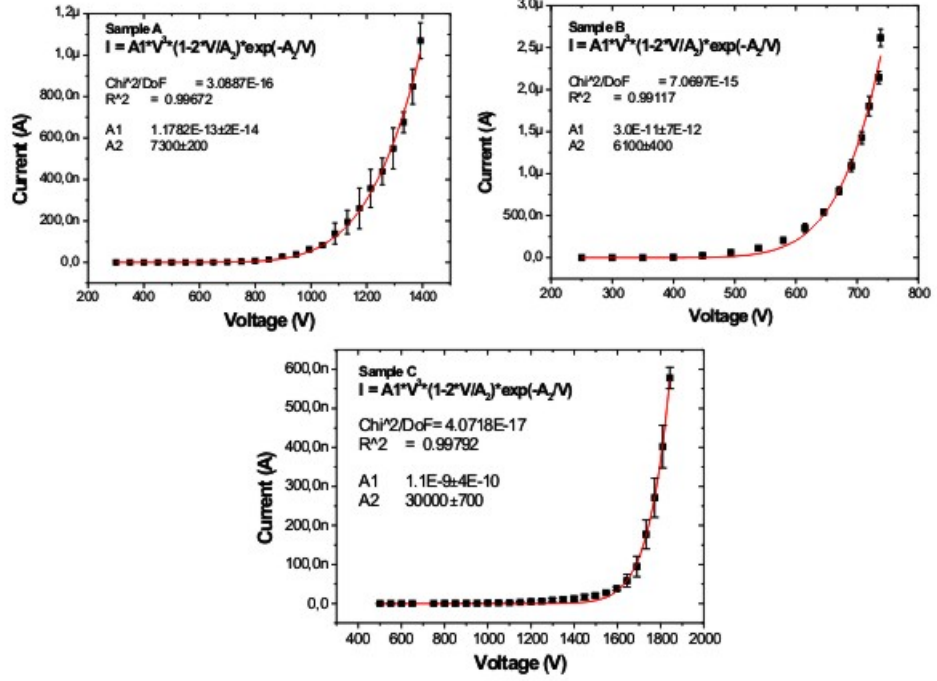


Figure 4.17: Averaged I-V curves for sample A, B, C fitted by eq. 4.17. The data of the fits are also shown.

Extraction fields are of the same order of magnitude as literature values, even if comparisons among different set-ups is not reliable. Lower extraction fields are observed for thinner emitters (single MWNTs, single or very thin bundles of SWNTs). Current densities of the order of some mA/cm^2 can be considered as a good starting point to open the way to the development of a field emission device.

The samples are named A, B, C following their increasing density of bundles (see sec. 3.3.3). As for bundle thickness, it can be roughly said that A has the thinnest bundles, while B has thicker bundles than C. C has the highest extraction field, following respectively B and A; looking at the β values, it is easy to see that the ability to enhance the applied field decreases as the density increases. Required field to allow 1 μA increases as the density increases, as well, but current density in the same conditions poses an opposite behavior.

	sample A	sample B	sample C
A_1	$1, 2 \cdot 10^{-13}$	$3, 0 \cdot 10^{-11}$	$1, 1 \cdot 10^{-9}$
A_2	7300	6100	30000
d_0 (μm)	55	15	25
V_{max} (V)	1393	738	1842
F_{max} ($V/\mu m$)	25	49	74
$F_{ext}(i = 1nA)$ ($V/\mu m$)	13	27	40
β	575	187	64
$A_{eff}(F = 25 V/\mu m)$ (cm^2)	10^{-4}	10^{-5}	$2 \cdot 10^{-5}$
$i(F = 25 V/\mu m)$ (A)	10^{-6}	$3 \cdot 10^{-9}$	-
$J(F = 25 V/\mu m)$ (mA/cm^2)	10	0,3	-
$F(i = 1\mu A)$ ($V/\mu m$)	25	47	76 (extrapolated)
$A_{eff}(i = 1\mu A)$ (cm^2)	10^{-4}	$2 \cdot 10^{-5}$	$3 \cdot 10^{-5}$
$J(1 \mu m)$ (mA/cm^2)	10	40	55

Table 4.1: Experimental and fit-extracted data for I-Vs shown in Fig. 4.17

The above obtained results can be explained as follows. The effect of the bundle density prevails over the different bundle thicknesses in influencing β values: the denser the bundles, the lower the overall β enhancement factor because of the field screening effect of the adjacent emitters, as it is expected (see sec. 1.4.1.2). When looking at the high current regime ($i = 1\mu A$), the highest current density is displayed by sample C (the most dense) at the expense of a very high estimated field. This results perfectly fits the picture of a low- β sample which requires high field but shows a more homogeneous emission.

Though sample A and B seems to lead to linear Fowler Nordheim plot (see Fig. 4.18), sample C response displays a large positive deviation in the high field region. Since a careful conditioning process has been carried out until reproducibility is achieved and since the showed curves are average ones (the standard deviation is shown in the error bars), this behaviour must be considered reproducible and not transient. At the level of I-V investigation in a moderate vacuum level, nothing can be said except that it may be explained by invoking tunnel resonant emission through very stable adsorbate states (see sec. 1.6.1).

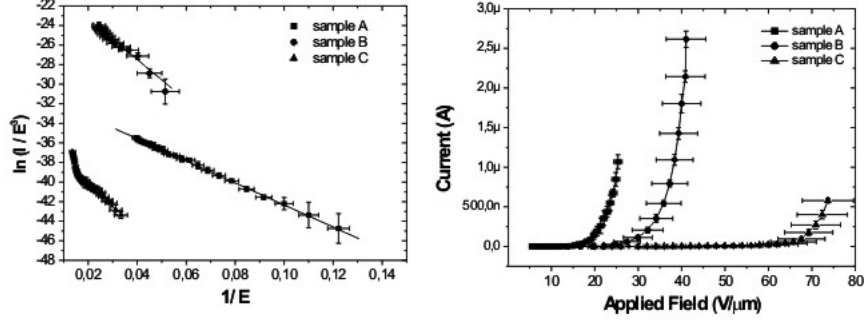


Figure 4.18: Comparison among sample A, B, C. Right: current-field curves. Left: corresponding Fowler Nordheim plots expressed in terms of field instead of voltage to make comparison meaningful (measurements were carried out at different anode-cathode distances).

4.3.5 I-V characterization of diamond-covered SWNT bundles

An I-V field emission characterization was performed on some diamond-covered SWNT bundle samples. The one carried out on the sample whose SEM images are shown in Fig. 3.9 will be here reported.

Following the measurement procedure explained in sec. 4.3.3, a careful conditioning treatment was performed.

As in the case of SWNT bundles samples, higher current, lower extraction voltage, instability and non reproducibility characterized the very first I-V scans. After the conditioning process, a good reproducibility was obtained. The average I-V curve with the corresponding fit is shown in Fig. 4.19, right.

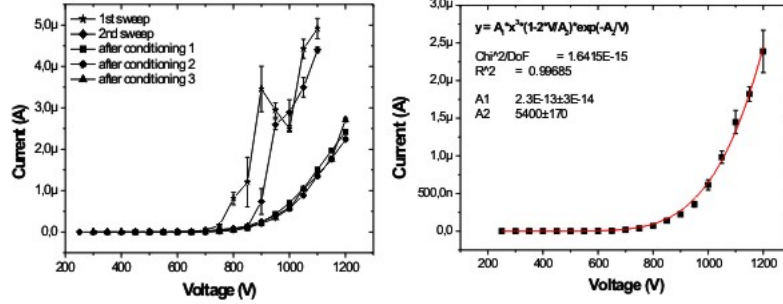


Figure 4.19: I-V curves on a diamond covered SWNT sample. Left: the very first I-Vs and three post-conditioning I-Vs are shown. Right: average I-V curve with the standard deviation as y error. The curve is fitted with eq. 4.17, the results of the fit are shown in the inset.

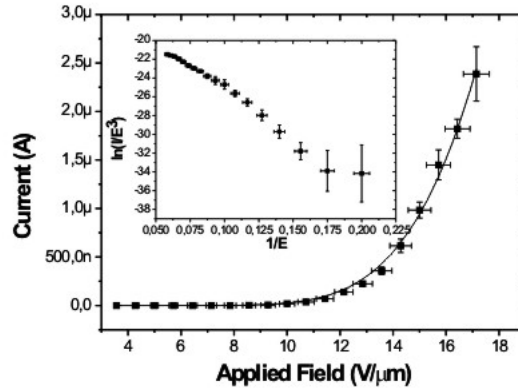


Figure 4.20: Current-field average curve corresponding to the average I-V shown in Fig. 4.19. The applied field is obtained via eq. 4.10. $F(1\text{nA}) = 7,7 \text{ V}/\mu\text{m}$. The Fowler Nordheim plot is shown in the inset.

However, emission of high currents ($> 2 \mu\text{A}$) lead to a new period of instability which could not be resolved by means of a new conditioning process.

A second, different point on the same sample was investigated. Field emission behavior resulted to be similar as shown in Fig. 4.21.

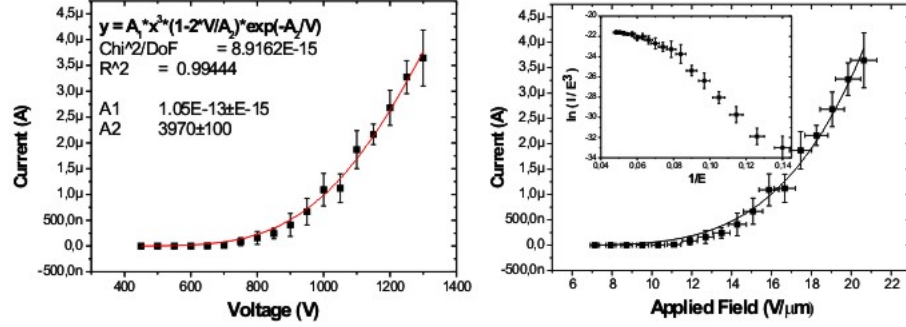


Figure 4.21: Average I-V (left) and average I-field (right) curves got from a second point of the same investigated diamond covered SWNT bundles sample in Fig. 4.19.

Experimental and fit-extracted data are shown in Tab. 4.2.

Extraction field occurred to be lower than $10 \mu\text{m}$ for both points of the same sample (overall the two points revealed similar field emission features thus indicating a good homogeneity of the sample). Moreover, current density of about $10 \text{ mA}/\text{cm}^2$ at the low value of $15 \text{ V}/\mu\text{m}$ applied field can be considered a really good result. Better field emission properties than our HFCVD-synthesized SWNTs can be therefore attributed to this hybrid material even if from the reported Fowler-Norheim plots of the averaged current-field curves (see Figs 4.21 and 4.19) the emission appear to be not metallic in both cases. It has been already said that a non-linear Fowler Nordheim plot is not enough (see sec. 2.1.2.2) to draw significative conclusions, so in order to decide the character of the emitter, further and deeper investigations are required. Since this material is completely new, the question is much more important than for nanotubes whose metallic character in field emission has been definitely assessed [77, 78].

diamond covered SWNT bundles	1st point	2nd point
A_1	$2 \cdot 10^{-13}$	$1 \cdot 10^{-13}$
A_2	5400	4000
d_0 (μm)	50	60
$\beta(^{\circ})$	707	954
$V_{max}(V)$	1200	1300
$F_{max}(V/\mu m)$	17	21
$F_{ext}(i = 1nA)(V/\mu m)$	7,7	9,8
$A_{eff}(F = 15 V/\mu m)(cm^2)$	$7,5 \cdot 10^{-5}$	$1 \cdot 10^{-4}$
$i(F = 15 V/\mu m)(A)$	10^{-6}	$6,7 \cdot 10^{-7}$
$J(F = 15 V/\mu m)(mA/cm^2)$	11	7

Table 4.2: Experimental and fit-extracted data for I-Vs shown in Figs. 4.20 and 4.21.

To reliably calculate β enhancement factor an estimation of workfunction is needed (see eq. 4.19). Workfunction for diamond covered SWNT bundles is not known, but since bulk diamond workfunction is 5,5 eV and estimated SWNT workfunction is 5 eV, a 5 eV workfunction is here used.

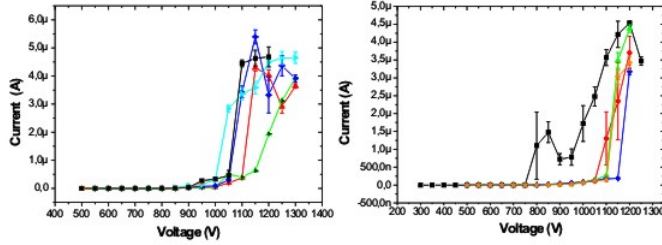


Figure 4.22: Instable I-Vs after the stability period represented respectively in Figs 4.21 (left graph) and 4.19 (right graph) from the diamond-covered SWNT sample.

Again, a neverending series of instabilities and discharges occurred. The successive SEM investigation did not reveal any surface damage but, since it is difficult even to locate the field emission investigated areas unless affected by extended and visible (therefor big) damages, this does not mean that no degradation at all scales occurred.

Even without any experimental proof, it is believed that some irreversible accident happened (for example the disruption of some of the best emitters, which can lead to the sputtering of the cathode material).

Chapter 5

Field emission energy distribution from diamond-covered SWNT bundles

I-V investigation provides the needed information for technological application of the proposed material (extraction field, current response as a function of voltage, stability, reproducibility) and can be regarded as a good starting point. The only way to go deeper into the emission mechanism is to measure the field emission energy distribution (FEED see sec. 1.5): the character of the emitter (metallic, semiconducting, insulating) can be in this way unambiguously determined. Moreover, tunnel-resonant emission due to undesired adsorbed gases (see sec. 1.6.1) can be recognised. In particular cases, through FEED, even resistance and emission temperature can be measured [78].

As a result of the I-V investigation carried out at the University of Tor Vergata in medium vacuum environment without heating treatment, we know that diamond-covered SWNT bundles have overall good field emission properties. Because of

- the novelty of our material,

- the exotic biphasical sp^2/ sp^3 hybrid constitution,
- the interest raised by both diamond and nanotubes in field emission,
- the long-term discrepancies and hypotheses on field emission from diamond (see sec. 2.2.4),

we decided to carry out a deeper, FEED investigation on it.

This experimental work was carried out in the Laboratoire de Physique de la Matière Condensée et Nanostructures at the University of Lyon 1, Lyon (France) under the supervision (and with the most fruitful help) of prof. Stephen Purcell and his group (Anthony Ayari, Pascal Vincent, Catherine Journet, Jean-Michel Benoit, Sorin Perisanu, May Choueib).

5.1 Experimental set-up

When dealing with the investigation of the very intrinsic field emission features and the emission mechanism of a sample, it is worthwhile stressing the importance of

- getting rid of the adsorbed gas molecules (therefore the importance of strong heating treatments);
- keeping the surface as clean as possible (by the use of ultrahigh vacuum);
- getting really sure that the detected electrons are not secondary and come from the emitters and not from occasional grains of dust or some edges of the sample and/or of the experimental set -up -i. e. winding wires- (in this regard the direct view of the emission pattern is the only guarantee).

The experimental set-up, home-built by prof. Purcell (schematized in Fig. 5.1), is a complicated system working in ultra high vacuum conditions which enables:

- simple I-V characterization (negative voltage supply to the sample and/or positive voltage supply to the anode, Keithley electrometer or current amplifier + ammeter);
- field emission pattern detection (microchannel plate to amplify current, phosphor screen, camera and image recording system);

- Joule-heating of the sample (independent heating circuit involving the sample; it is possible to heat and in the meanwhile do field emission; sample temperature is measured by means of an optical pyrometer through a window from which it is possible to check the integrity of the sample as well);
- electron-bombardment of the sample (degassing/heating loop);
- field emission energy distribution measurement (XPS-ESCA type electron energy analyzer: the entrance of the analyzer is made up of a little probe hole which enables the measurement of the electron beam coming from a small part of the sample and to avoid secondary electrons);
- field ion imaging (gas inlets - H_2 , N_2 , Ar-);
- supplying of a contemporary DC/AC signal (AC generator connected to the sample).

The sample consisted of a 1cm x 1 cm *Si* wafer with two squared 1 mm x 1 mm selected area deposition layers (see sec. 3.3.5.3). From Fig. it is possible to see a great number of emitters with roughly the same geometrical features.

The sample was mounted onto a purpose-realized Mo sample holder with a Ni TEM grid at a distance of about 150 μm distance (see Fig. 5.2). The grid (round, with a diameter of 1 mm) was centered onto one of the squares. Even if only one square will be involved in the measurements, the recorded emission will be due to more than one emitter.

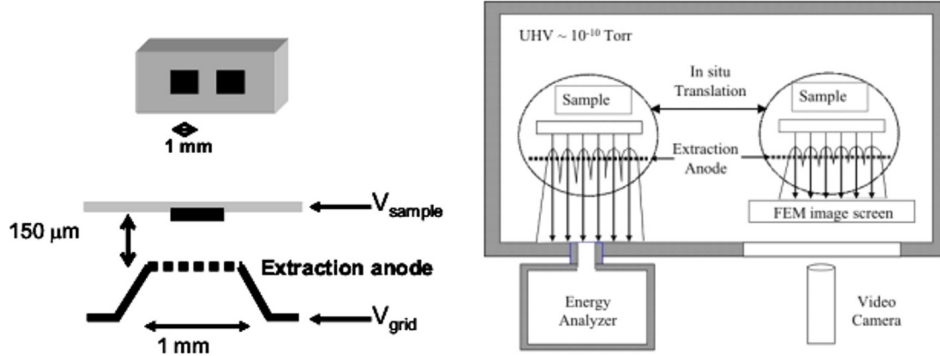


Figure 5.2: Schematized image of the sample (top left), the sample and sample holder system (bottom left) and the geometrical arrangement of the measurement set-up with the planar sample (right). The sample-grid distance was estimated with an optical microscope.

5.2 Preliminaries and experimental conditions

Working pressure was $3,1 \cdot 10^{-10} \text{ mbar}$.

The viewing of the emission pattern was carried out as a first check of the integrity and position of the emitters at each turning on of the system: with the maximum sensitivity set for the microchannelplate, grid voltage was usually slowly increased until a signal on the screen was seen.

After the first emission signs ($V_{\text{sample}} = -1900\text{V}$), we used to increase voltage more slowly until a defined emission pattern could be seen. The increase in voltage is expected to produce an increase in light intensity. The very first spots represent the best emitters; some others may appear when increasing voltage.

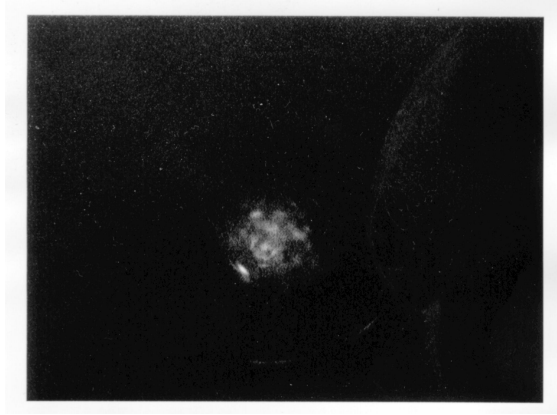


Figure 5.3: First field emission pattern recorded at $V_{\text{sample}} = -2500$ V. The circular symmetry of the image resemble the shape of the grid. Some brighter spots can be hardly distinguished as well as a diffuse brightness due to an undefined number of less efficient emitters. The intensity of light and shape of the pattern proved to be very stable.

Due to the circular shape of the extraction anode grid, a full circular emission pattern was seen: this is a clear sign that the sample has homogeneous emitting properties. Fig. 5.3 shows one of the very first complete emission patterns. Once obtained the pattern, we used to observe whether the pattern changed in shape or in intensity with time: it proved to be really stable.

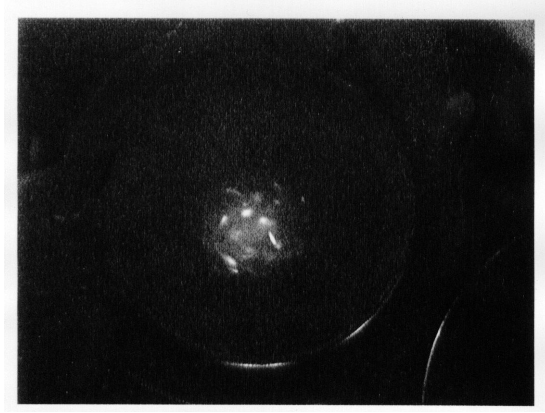


Figure 5.4: FE pattern recorded in the same experimental conditions of Fig. 5.3 after the heating treatment. At least 5 brighter emitters can be seen in the diffuse brightness.

A Joule-heating treatment of the sample was performed by letting a DC current pass through the sample. Due to the semiconducting nature of the substrate, the observed increase of current intensity with increasing applied voltage was not linear. We measured a maximum current of 0,4 A at a voltage of 11 V. As the sample got a little red, an increase of pressure up to 10^{-7} mbar was observed; this is the effect of a strong sample degassing process. The treatment lasted no more than 5 minutes. Unfortunately, it was not possible to measure sample temperature. After the heating treatment a brighter emission pattern was obtained (see Fig. 5.4) showing more defined spots.

After the above preliminary operations, the investigation involved measurements of

1. $I(V)$ characteristic: with null grid voltage, sample voltage ranged from -2900 V to -1000 V (corresponding to an applied field ranging from 6,6 to $20 \text{ V}/\mu\text{m}$) with voltage steps of 50 V. A delay of 10 s was set at each voltage step before recording emission current. In one case grid voltage was set to + 1000 V and sample voltage ranged from -1900 V to -100 V (that corresponds to the same field range as before). The handling of such high voltages obliged us to use the current amplifier + ammeter system to measure current; since it was not possible to calibrate the amplifier, we could not give reliable current values. This lack was not considered a serious drawback because the

aim of the work was to study emission mechanism (i.e. linearity of Fowler Nordheim plot). Quantitative emission measurements, though in a much less clean environment, have been already carried out in Rome and reported in sec. 4.3.5. Results and discussion of $I(V)$ characterization are reported in sec. 5.3.

2. $I(t)$ i.e. current stability: voltage grid was set to + 1000 V and sample voltage to -1200 V (which corresponds to an applied field of about $15 \text{ V}/\mu\text{m}$), time interval was set to 2 s. The corresponding results and discussion are reported in sec. 5.3, too.
3. $i(V, \varepsilon)$ i.e. the FEED as a function of voltage: $V_{\text{sample}} = -1000 \text{ V}$ (the Fermi level is therefore positioned at 1000 eV), grid voltage ranged from 300 V to 1300 V with 50 V steps. The applied field ranged therefore from 8,7 to $15 \text{ V}/\mu\text{m}$. As for the energy analyzer, energy step was set to 0.3 eV. Sample position was adjusted so as to maximize the intensity of -200 eV peak. Results and discussion are reported in sec. 5.4.
4. $i(x, \varepsilon)$ i.e. FEED as a function of the sample position with respect to the probe hole (independent variable x): $V_{\text{sample}} = -1000 \text{ V}$, $V_{\text{grid}} = 1300 \text{ V}$, which corresponds to an applied field of about $15 \text{ V}/\mu\text{m}$. Energy step was set to 0.3 eV. Sample position was first adjusted so as to maximize the intensity of -200 eV peak, then stepped movement of the sample with respect to the probe hole were carried out by rotating two different handles. It was not possible to exactly relate the single stepped movement to the real displacement of the sample but, according to a reasonable estimation, a single rotating movement should correspond to a linear μm -scale movement of the sample. The corresponding results and discussion are reported in sec. 5.5.

5.3 $I(V)$ and $I(t)$ characterization

The highly reproducible I-V curves shown in Fig. 5.5 were obtained without any conditioning step.

The performed heating treatment caused a big desorption effect (which was directly observed as a sudden increase of pressure of 3 orders of magnitude); furthermore, ultrahigh vacuum conditions assure that the cleaned surfaces remain thoroughly clean.

This demonstrates that in the so called conditioning process described in sec. 4.3.2, the main performance-enhancement effect is gas desorbing.

The Fowler-Nordheim plot shown in the inset of Fig. 5.5 has an overall linear behaviour except for the high voltage region where a significant positive deviation from linearity is observed.

A similar behavior was observed in a SWNT sample in medium vacuum environment (see sec. 4.3.4) but in that case the presence of adsorbates prevented us from proposing any explanation.

This is a very different case since no residual gas is believed to remain adsorbed to the surface of the emitters. Apart from adsorbate effects, positive deviation from Fowler Nordheim law at high voltages (and therefore high currents) is expected (and observed) in presence of self-heating of the emitters [77]. In this regard, the more resistive the sample, the more intense the Joule effect during emission.

It cannot be excluded, however, that such high voltages can act on the thin TEM grid used as the extraction anode grid by bending it. A grid bending would result in an applied field higher than what it is expected, therefore in a higher emission current.

Since of both effects may reasonably occur, we take the sum of the two as the explanation the observed deviation.

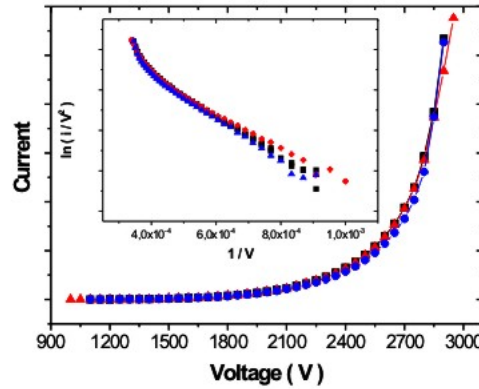


Figure 5.5: I-V measurements with the corresponding Fowler Nordheim plot in the inset.

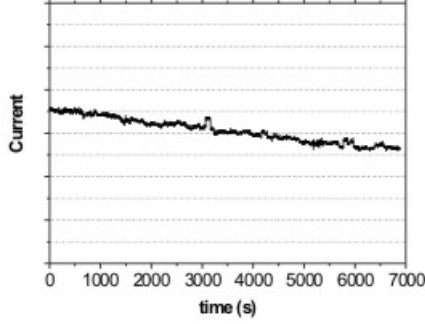


Figure 5.6: $i(t)$ measurement at an applied field of about $15 \text{ V}/\mu\text{m}$.

Current stability proved to be qualitatively good. Quantification is difficult because we were unable to give reliable current values (therefore y axis of Fig. 5.6 is mute). As a rule of thumb, each minor tick can be considered as 1 nA: therefore after almost 2 hours continuous emission, a decrease of a bit more than 25% is observed. No spikes were observed.

5.4 $i(V, \varepsilon)$ characterization

A unexpected (see sec. 1.5) FEED consisting of a multipeak pattern over a very wide energy range from Fermi level downwards was observed (see Fig. 5.7). Change in almost all experimental settings of the analyzer (energy step, energy pass, diaphragm) and sample position did not change the appearance of the spectra.

Multipeak appearance of FEED is generally observed for tunnel-resonant emission due to adsorbates [42, ?] but the spectrum changes from time to time due to surface diffusion/desorption/readsorption [42] and peaks are generally located within 10-20 eV from Fermi level.

Peaks in our spectra proved to be perfectly reproducible and located up to 500 eV away from the Fermi level. The lowest energy peak at highest applied voltage is located at -508 eV, the highest energy peak at -24 eV away from Fermi level. Average FWHM of peaks is 4 eV.

In order to study the influence of voltage onto the appearance of the spectra, we acquired a series of spectra keeping constant sample voltage (therefore the position

of the Fermi level) and varying grid voltage (see Fig. 5.8). An overall decreasing of peak intensity due to the decrease of applied field was observed together with a shift of peak position towards higher energies. At the lowest applied field ($V_{\text{grid}} = 300$ V) all peaks are located within 100 eV away from Fermi level.

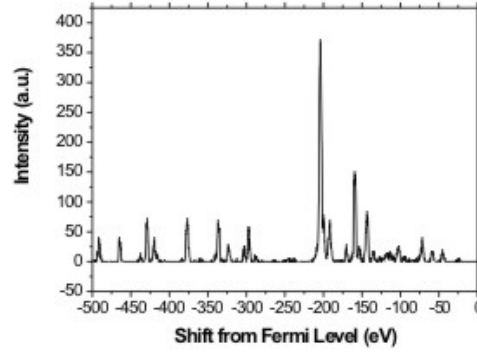


Figure 5.7: FEED obtained with the following experimental parameters: $V_{\text{sample}} = -1000$ V; $300 \leq V_{\text{grid}} \leq 1300$ V ; energy step 0.3 eV.

Most peak positions were plotted against grid voltage in the following figure.

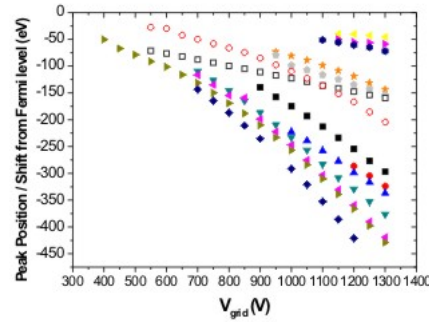


Figure 5.9: Peak position vs. grid voltage.

Behaviour of peak position vs. grid voltage is roughly linear in the high voltage range but deviates negatively in the low voltage range. Moreover, the region near

the Fermi level becomes more and more crowded as voltage lowers, therefore it is more difficult to follow peak positions (there are peak superpositions and inversion of peak positions). Overall, each peak shifts independently from the other and the farther the peak from the Fermi level, the higher the slope of the curve.

It was not possible to fit and integrate such narrow peaks to get total current and plot peak position vs. emitted current. It was not possible even to follow the behaviour of each peak position vs. its intensity because peaks, by moving independently, undergo frequent superpositions. Therefore we performed the sum of all counts for each spectra and assumed that this sum resembles the total emitted charge detected by the analyzer. Further step was to plot peak position against Count-Sum.

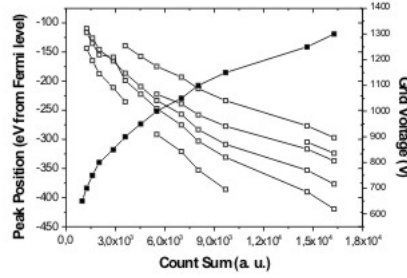


Figure 5.10: Some peak positions plotted vs. Count Sum (left y axis). A plot of grid voltage vs. Count Sum is also shown (right y axis).

Peak position vs. Count-Sum has a roughly linear behaviour except for a slight positive deviation at low Count-Sum. It must be taken into account that at low applied voltage and therefore low emission current the instrument noise is not negligible and the error attributed to those points is significantly higher. The contemporary plot of Count-Sum vs. grid voltage helps confirming that the assumption that Count-Sum is directly proportional to the emission current: the behavior is qualitatively exponential, as expected.

Reproducible peak shift at the low energy side of Fermi level can be attributed to

1. field penetration
2. resistive drop along the emitter.

Both phenomena are typical of resistive materials, therefore we have to conclude the electrons do come out from the outer diamond phase of our material and not from the underlying graphitic phase through diamond grain boundaries. On the contrary, some literature field emission experiments on diamond films reported that the electrons were coming from the region in between the crystalline grains which represent depressions instead of protrusions (see sec. 2.2.4): those experiments, therefore, couldn't be strictly regarded as field emission measurements on diamond. Since diamond grains are the very protruding objects in our material, their β field enhancement factor helps them preventing emission from other phases endowed with more favourable emission properties.

Moreover, as for field penetration, the expected behavior of peak position vs. applied voltage is linear [96]; as for resistive drop, peak shift should be linear in current, therefore exponential in voltage [42].

Our case is not purely linear in voltage nor in current, therefore we cannot refer to a single explanation: a combination of the two effects is to be invoked.

Such huge peak shifts have never been reported in diamond literature and, in general, field emission literature except for highly resistive Ge emitters in the 60s [122]. It is to be noted, however, that no FEED investigation on diamond was carried out after a severe heating treatment focused to the removal of all interfering surface gases (see sec.2.2.4).

Last but not least, the independence of peak shift vs. voltage suggests that each peak can be related to an emitter with its one resistance value. Different thicknesses of the outer diamond coverage and/or different emitter lengths can be reasonably invoked for explanation.

5.5 $i(x, \varepsilon)$ characterization

In order to verify if each peak is physically related to an emitting site/sites, we took advantage of the possibility of performing local FEED investigation and carried a measurement of FEEDs at different positions of the sample with respect to the analyzer entering probe hole. We expected that if the observed peaks were due to specific emitting sites, the movement of the sample would result in a variation of peak intensity. Within this framework, an emitter perfectly aligned with the probe hole will be responsible of one of the most intense peak; as its position is varied and some misalignment is introduced, the intensity of its peak will decrease. When

the displacement is such that the emitter goes out of the investigated region, its peak will vanish.

Typical results are shown in the following figure.

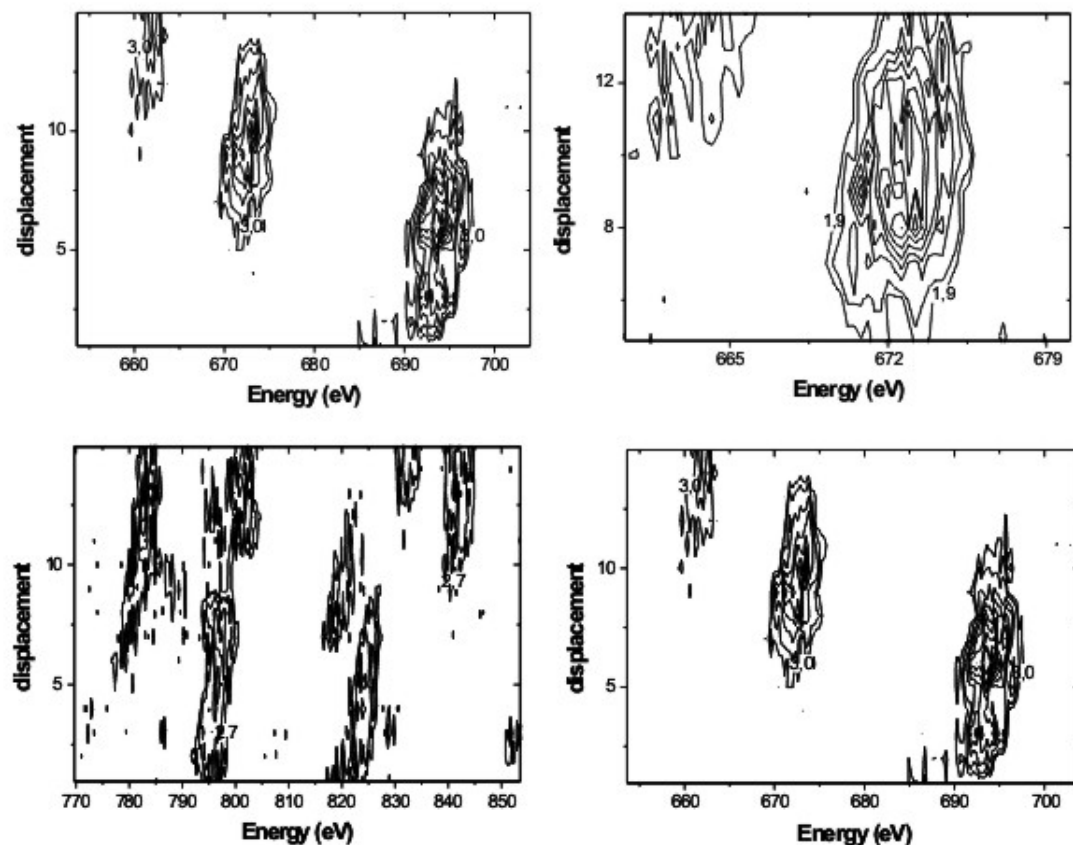


Figure 5.11: Some maps of FEED intensity vs. energy (x axis) and displacement (y axis). The elongation of the pattern in the y direction is exaggerated by the software (Microcal Origin).

By taking the third dimension (counts of the energy analyzer) as the altitude, it is easy to see in the level curves reported in the maps, isolated “mountains”. Taking into account the exaggerated elongation of the map in the y direction performed by

the software, it is not difficult to recognise circular shaped objects. The reported results, therefore, confirm all the exposed hypotheses on the origin of so many peaks in FEEDs.

5.6 Conclusions

Two points assure us to have studied true field emission from the diamond phase:

1. the complete diamond coverage of very protruding objects such as nanotube bundles (localization of emission has been directly viewed in the emission pattern);
2. the careful removal of any adsorbates through the performed heating treatment.

In this view, the information drawn from FEED investigation gave us the following information:

1. Emission current was very stable in the tens of nA range.
2. The highly reproducible I-V curves demonstrated a roughly Fowler-Nordheim behaviour in the investigated field range.
3. The presence of many peaks strongly shifted with from the Fermi level is a proof of the highly insulating nature of the emitting material. The shift is due to field- induced band bending and resistive drop. This is the first experimental evidence of a resistive loss of energy of the electrons being field-emitted from a diamond.
4. Since each peak move independently from the others as the grid voltage changes, it can be related to a single, independent emitting site.
5. By moving the sample with respect to the probe hole of the analyzer, it was possible to draw a map of the emitting sites.

Therefore the existence of multiple peak pattern can be explained in term of different resistances (different lenghts of the wire-like structure, different thicknesses of diamond coverage).

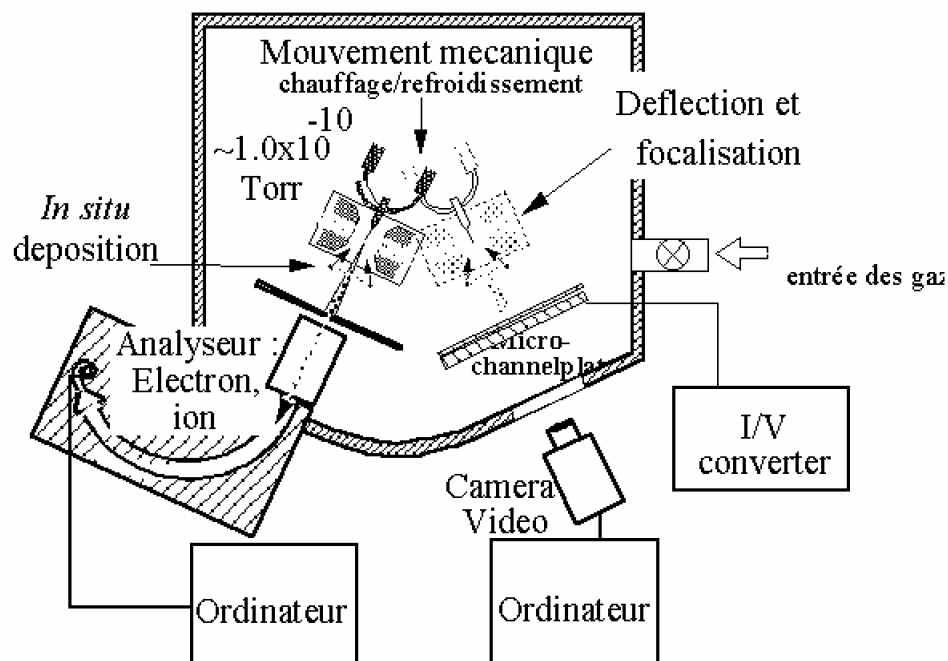


Figure 5.1: Schematic picture of the field emission system in the lab of prof. Stephen Purcell, Laboratoire de Physique de la Matière Condensée et Nanostructures in the University of Lyon 1, Lyon (France). In this picture the sample is a tip (the so called “head” of the system, at the center of the image). The sample holder can be mechanically moved from one position (microchannelplate, phosphor screen and camera to view field emission pattern and/or I-V) to another (energy analyzer). The analyzer has a probe hole to exclude the secondary electrons and to carry out local investigations. There is a deflection and focalisation system made up of 2 couples of electrodes connected to the head of the system (and therefore the sample holder). A system of rotative, turbomolecular and ionic pumps enable a working pressure of $10^{-10} - 10^{-11}$ Torr.

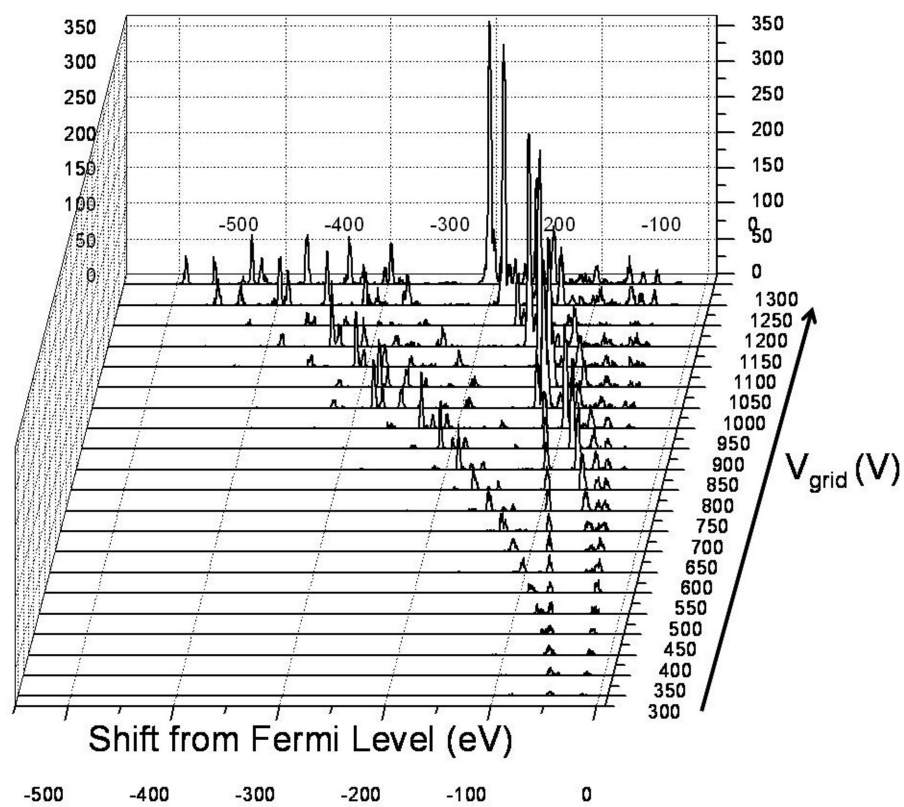


Figure 5.8: Series of FEEDs taken at decreasing grid voltages. $V_{\text{sample}} = -1000\text{V}$

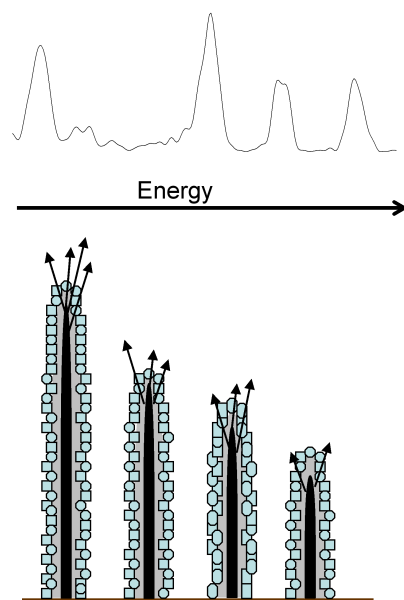


Figure 5.12: Scheme of the possible effect of lenght on the FEED from diamond-covered single wall carbon nanotubes.

Chapter 6

Proposal of two SWNT-based field emission devices

A field emission triode based and an X-ray tube are proposed as possible field emission devices taking advantage of the the promising properties of carbon nanotubes. The two prototypal devices will be described by means of two proceedings:

- V.Sessa, A.Ciorba, A.Fiori, M.Lucci, S.Orlanducci, M.L.Terranova, G.Cappuccio, D.Hampai, S.Cialdi and M.Rossi: “Carbon nanotube cold cathodes for miniature X-ray tubes” - SPIE Channeling 2006 (in press)
- F.Brunetti, P.Lugli, R. Riccitelli, E.Petrolati, L.Von Neumann, A. Reale, C.Paoloni, A. Di Carlo, A. Fiori, S. Orlanducci, E.Tamburri, A. Ciorba, M. L. Terranova, V.Sessa, M. Cirillo, V.Merlo: “Realization of carbon nanotube-based triode” 6th IEEE Conference on Nanotechnology Cincinnati (Ohio) July 2006

Chapter 7

Conclusions

This three year work dealt with the synthesis and field emission characterization of plain and diamond-covered single wall nanotubes.

The synthesis step took advantage of a hot filament chemical vapor deposition set up modified by the introduction of a powder flowing system: a range of unusual solid carbon precursors can thus be exploited. After an optimized methodology for the deposition of single wall carbon nanotubes using carbon nanopowders obtained by laser pyrolysis as feedstock, by means of a fine tuning of experimental conditions, samples with different morphologies have been obtained whose study has an interest in field emission. Selected area growth and growth into predefined locations on multilayer substrates were achieved as well, thus paving the way to the realization of prototype-field emission based devices. Moreover, the versatility of the synthesis apparatus has been demonstrated by means of the successful use of different feedstocks: carbon nanopowders, diesel soot and commercial graphite.

Moreover, in exploring the wide possibilities offered by our set-up, a new hybrid carbon material has been synthesized and characterized: diamond-covered single wall carbon nanotubes. On the base of a time study, a growth mechanism has been also proposed. The coupling of graphitic wire-like and diamond phases represents a very interesting hybrid system for field emission.

As for field emission characterization, a newly built, home-made set-up with sphere-to-plane measurement configuration has been tested on our materials. Survival of our carbon films have been always observed in medium vacuum environment, which constitutes a prohibitive environment for conventional metallic and

semiconducting emitters. The annoying effect of adsorbates on the smoothness and reproducibility of current-voltage curves has been recognized and minimized with the setting up of a suitable conditioning step.

On reflection about the lack of a common methodology for data analysis in field emission current-voltage investigations, I started my quantitative study from two critical questions: applied field and emitting area evaluation. Their criticality comes from the fact that the two basic parameters characterizing an emitting material are the extraction field (i. e. the applied field necessary for the extraction of 1 nA current) and current density (emitted current normalized by the emitting area). A capacitive approach for anode-cathode distance measurement -hence field estimation- has been successfully set-up and tested on plane metallic, highly rough (nanotube film) and insulating surfaces. Moreover, a simple analytical method for emitting area evaluation has been developed. By means of these two parameters, the basic field emission features of the investigated samples can be drawn and fruitfully compared.

The proposed new methodologies have been applied to the investigation of single wall nanotube samples significantly differing in morphology. Quantitative comparisons have been made: due to the field screening effect, as the density of emitters increase, the extraction field has been found to increase. A current density of the order of some mA/cm^2 at applied fields of 10-70 $\text{V}/\mu\text{m}$ has been estimated: such values (in particular the lower one), together with the survival and the reproducibility of response at medium vacuum level (called also “industrial vacuum”) represent a good starting point for the realization of a field emission device.

Current-voltage investigation proved that diamond-covered single wall carbon nanotubes possess promising field emission properties as well.

Due to their exotic structure, a deeper field emission investigation has been carried out. Field emission energy distribution measurements have been performed in the laboratory of Prof. S. T. Purcell in Lyon. Well aware of the subtle, disturbing effect of adsorbates in field emission investigations, we carried out a careful heating treatment and carried out the measurements in ultra high vacuum conditions. The obtained energy spectrum of the emitted electrons showed a surprising multipeak pattern ranging from the Fermi level downwards. The peaks proved to be firmly reproducible and to shift toward the Fermi level as the voltage decrease. Moreover, by performing a local measurements and a scan over the sample, it has been

concluded that each peak correspond to an emitter or group of emitters. Since the carbon nanotubes represent the most protruding objects and that they are covered by small diamond crystal, emission should be surely ascribed to diamond. The shift of the emission peaks from the Fermi level is therefore believed to be due to the high insulating nature of diamond: field penetration and resistive drop must account for the observed effects. The existence of multiple peak pattern can be explained in term of different resistances (different lengths of the wire-like structure, different thicknesses of diamond coverage). This is the first time such field emission energy distribution appears: it is to be noted that this is the first study of this kind from diamond after a severe heating treatment, so from a thoroughly cleaned surface.

This work has been carried out within the multidisciplinary approach of MINAS Lab. MINAS Lab is formed of several working groups, belonging to different Departments and Faculties, which share a common interest about the design, development and characterization of micro and nanostructured systems:

- MINIMA @ Department of Chemical Science and Technology headed by prof. Maria Letizia Terranova;
- OPTOLAB @ Department of Electronics Engineering headed by prof. Aldo Di Carlo;
- NEMO @ Department of Physics headed by prof. M. Casalboni and Prof. Matteo Cirillo.

The availability of so many and different contributions lead to the proposal of two single wall carbon nanotube devices: a field emission triode and a X-ray tube.

Chapter 8

List of publications

Papers

- I. Boscolo, S. Cialdi, A. Fiori, S. Orlanducci, V. Sessa, M. L. Terranova, A. Ciorba, M. Rossi: "Capacitive and analytical approaches for the analysis of field emission from carbon nanotubes in a sphere-to-plane diode" J. Vacuum Science and Technol. (submitted)
- D. Passeri, A. Bettucci, M. Germano, M. Rossi, A. Alippi, V. Sessa, A. Fiori, E. Tamburri, and M. L. Terranova: "Local indentation modulus characterization of diamond-like carbon films by atomic force acoustic microscopy two contact resonance frequencies imaging technique? Appl. Phys. Lett. 88, 121910
- S. Orlanducci, A. Fiori, E. Tamburri, V. Sessa, M. L. Terranova and M. Rossi: "Nanocrystalline non-planar carbons: growth of carbon nanotubes and curled nanostructures" Crystal Research and Technology 928-931 (2005)
- M. L. Terranova, S. Orlanducci, A. Fiori, E. Tamburri, V. Sessa, M. Rossi, A. S. Barnard: "Controlled Evolution of Carbon Nanotubes Coated by Nanodiamond: the Realization of a New Class of Hybrid Nanomaterials" Chem. Mater. 17 3214-3220 (2005)
- M. Abbas, Z. Y. Wu, J. Zhong, K. Ibrahim, A. Fiori, S. Orlanducci, V. Sessa, M. L. Terranova, Ivan Davoli: "X-ray absorption and photoelectron

spectroscopy studies on graphite and single-walled carbon nanotubes: Oxygen effect" *Applied Physics Letters* 87 051923-1 051923-3 (2005)

- S. Botti, R. Ciardi, L. Asilyan, L. De Dominicis, F. Fabbri, S. Orlanducci, A. Fiori: "Carbon nanotubes grown by laser-annealing of SiC nano-particles" *Chem. Phys. Lett.* 400 264-267 (2004)

Proceedings

- M. Lucci, A. Reale, A. Di Carlo, E. Tamburri, A. Fiori, V. Sessa, S. Orlanducci, F. Toschi, M. L. Terranova "Celle Solari basate su Materiali Nanostrutturati" III° Simposio sulle Tecnologie Avanzate: utilizzo e applicazione delle nanotecnologie per la difesa nei settori Strutturale, Elettronico, Biotecnologico - Roma 2006
- M. Lucci, A. Reale, A. Di Carlo, E. Tamburri, A. Fiori, S. Orlanducci, V. Sessa, M. L. Terranova, A. Ciorba, M. Rossi, C. Falessi "Prototipo di sensore di gas basato su nanotubi di Carbonio allineati" III° Simposio sulle Tecnologie Avanzate: utilizzo e applicazione delle nanotecnologie per la difesa nei settori Strutturale, Elettronico, Biotecnologico - Roma 2006
- I. Boscolo, S. Cialdi, L. Cultrera, D. Cipriani, V. Sessa, S. Orlanducci, A. Fiori, M. L. Terranova: "Tests on diamond films as current amplifiers for photocathodes" - SPIE Channeling 2006 (in stampa)
- V. Sessa, A. Ciorba, A. Fiori, M. Lucci, S. Orlanducci, M. L. Terranova, G. Cappuccio, D. Hampai, S. Cialdi and M. Rossi: "Carbon nanotube cold cathodes for miniature X-ray tubes" - SPIE Channeling 2006 (in stampa)
- M. L. Terranova, V. Sessa, A. Fiori, S. Orlanducci, E. Tamburri, P. Di Stefano, A. Ciorba, M. Rossi "Field Emission properties of Nanodiamonds, Nanotubes and Hybrid Nanocarbon Materials grown by CVD" *Nanocarbon and Nanodiamond*, St. Petersburg 2006, 36
- V. Sessa, M. Lucci, A. Fiori, S. Orlanducci, F. Toschi, E. Tamburri, M. L. Terranova, G. Cappuccio, D. Hampai, A. Ciorba, M. Rossi "cold cathodes assembled with carbon nanotubes for miniature x-ray tubes" *Nanophase Materials*, Rome 2006

- F. Brunetti, P.Lugli, R. Riccitelli, E.Petrolati, L.Von Neumann, A. Reale, C.Paoloni, A. Di Carlo, A. Fiori, S. Orlanducci, E.Tamburri, A. Ciorba, M. L. Terranova, V.Sessa, M. Cirillo, V.Merlo: "Realization of carbon nanotube-based triode" 6th IEEE Conference on Nanotechnology Cincinnati (Ohio) July 2006
- M. L.Terranova, A.Fiori, S.Orlanducci, E.Tamburri, F.Toschi, V.Sessa, M.Rossi "Vapour growth of nanocrystalline diamond and tubular nanographites" Atti Accademia dei Lincei (in stampa)
- F. Brunetti, A.Di Carlo, R.Riccitelli, A.Reale, P.Regoliosi, M.Lucci, A.Fiori, M.L.Terranova, S.Orlanducci, V.Sessa, A.Ciorba, M.Rossi, M.Cirillo, V.Merlo, P.Lugli and C.Falessi "Towards the realization of multielectrode field emission device: controlled growth of single walled carbon nanotube arrays" Nanotechnology II ed. P. Lugli, L.B. Kish, J. Mateos - SPIE 2005, vol. 5838 154-161
- V.Sessa, S.Orlanducci, A.Fiori, M.L.Terranova, F.Tazzioli, C.Vicario, I.Boscolo, S.Cialdi, and M.Rossi "Photoemission from nano-structured a-C/diamond layers irradiated by intense Nd:YAG laser harmonics" Nanotechnology II ed. P. Lugli, L.B. Kish, J. Mateos - SPIE 2005, vol. 5838 216-223
- A.Di Carlo, A.Reale, F.Brunetti, R.Riccitelli, E.Petrolati, M.L.Terranova, S.Orlanducci, A.Fiori, V.Sessa, A.Ciorba, M.Rossi, M.Cirillo, V.Merlo, C.Falessi, A.M.Fiorello, M.Varasi "Nanovalvole" II Simposio sulle Tecnologie avanzate : applicazione delle nanotecnologie per la difesa nei settori Strutturale, Elettronico, Biotecnologico - Roma 2005
- A.Di Carlo, A.Reale, F.Brunetti, R.Riccitelli, E.Petrolati, M.L.Terranova, S.Orlanducci, A.Fiori, V.Sessa, A.Ciorba, M.Rossi, M.Cirillo, V.Merlo, C.Falessi, A.M.Fiorello, M.Varasi "Nanovalvole" II Simposio sulle Tecnologie avanzate : applicazione delle nanotecnologie per la difesa nei settori Strutturale, Elettronico, Biotecnologico - Roma 2005
- M.L.Terranova, A.Fiori, S.Orlanducci, V.Sessa, E.Tamburri, and M.Rossi "Strategies towards the assembling of carbon nanotube systems for particle and electromagnetic beam handling" SPIE Channeling 2004. ed. by Sultan Dabagov 2005 5974

- M.L.Terranova, V.Sessa, S.Orlanducci, A.Fiori, E.Tamburri and M.Rossi "Growth of nanosized carbon structures with predefined architectures" Proceedings EUROCVT-15 eds. A.Devi, H.Parala, M.L.Hitchman R.A.Fisher, M.D.Allendorf, 2005-09, 340-347 (ECS, NJ, 2005)
- V. Sessa, A. Fiori, S. Orlanducci, E. Tamburri, M. L. Terranova, F. Toschi, M. Rossi "New route in carbon nanotubes synthesis by means of a modified Hot Filament Chemical Vapor Deposition technique" Syntheses and methodologies in inorganic chemistry
- F.Brunetti, E.Tamburri, A.Reale, A.Di Carlo, P.Lugli, S.Orlanducci, M.L.Terranova and A. Fiori "Carbon nanotube/conducting polymer composites for electronic applications: materials preparation and devices assembling" IEEE-NANO 2004 WE-P11
- F.Brunetti, P.Regoliosi, A.Reale, A.Di Carlo, M.L.Terranova, S.Orlanducci, A.Fiori, E.Tamburri, V.Sessa, A.Ciorba, M.Rossi, M.Cirillo and V.Merlo "Controlled growth of ordered SWCNTs for the realization of multielectrode field emitter devices" IEEE-NANO 2004 WE-P12
- A Fiori, S.Orlanducci, E.Tamburri and M.L.Terranova "Introduction to Carbon nanotubes: fabrication and properties" EMC Europe 2004, 244-250 (T.U. Eindhoven 2004) (Tutorial)

Acknowledgments

Semplicemente, Andrea. Per tutto. Che pazienza ci vuole, eh?

I compagni di avventura (direi quasi di vita): Silvia, Emanuela, Francesco.

Indiscutibilmente la prof., sponsor e promoter di tutti noi (posso ancora dire “noi”, vero?).

Gli ingegneri (croce e delizia): Ric, Francesca, Max, Pietro e i nuovi ingegneri Luca “Frau” e Fabrizio. In particolare quelli che hanno scontato la pena della loro “ingegneritudine” con il temporaneo internamento a Chimica. Qualcuno è anche rimasto.

I boss degli ingegneri: Aldo e Andrea. Anche per l’animazione alle feste.

Direi allora tutto il festaiolo gruppo di Aldo, per lo spirito di squadra e l’entusiasmo.

Marco Rossi e Daniele “Passerotto” a La Sapienza.

“Gli analitici”, squisiti vicini di casa nonchè gentili fornitori di cavatappi (e quant’altro) per i numerosi festeggiamenti.

Fuori categoria, Nora e Arcanino. Per saecula saeculorum.

I tornimpartesi storici: Marianna, Pasqui, Stefano. Per via del mio strano lavoro, hanno sempre perdonato le mie lunghe assenze. L’enfant prodige: Giusti.

I lionesi: Domenica, Valentina, Giulia, Davide, Raluca, Anthony, May. Anche Pascal. Steve, perchè quando parla di field emission schiude universi paralleli.

I “sestrini”: Scalisi, Nello, Salvo, Peddis.

Mamma, papà, Lorenzo, perchè avere in casa qualcuno che scrive una tesi di dottorato è come abitare accanto ad un reattore nucleare sempre al limite della fusione del nocciolo.

Tutti i sostenitori consapevoli e non (FCV: Ufficio Sicurezza e ambiente, Reparto Depurazione acque) che in questo momento di frenesia isterica mi sono sfuggiti. Sento che sono tanti e che dovrò produrmi in scuse infinite per la loro dimenti-

canza.

Bibliography

- [1] C. A. Spindt *J. Appl. Phys.* 39 (1968) 3504.
- [2] C. A. Spindt, I. Brodie, L. Humphrey, E. R. Westberg *J. Appl. Phys.* 47 (1976) 5248
- [3] I. Brodie, C. A. Spindt “Vacuum microelectronics” *Adv. Electron Electron. Phys.* 83 (1992) 1
- [4] N. S. Xu, S. E. Huq *Materials Science and Engineering* R48 (2005) 47
- [5] A. Einstein *Annalen der Physik* 17 (1905) 132
- [6] O. W. Richardson *Phil. Mag.* 28 (1914) 633
- [7] Millikan, Lauritsen *Proc. Nat. Acad. Sci.* 17 (1928) 15
- [8] W. Schottky *Z. Physik* 131 (1923) 63
- [9] R. J. Oppenheimer *Phys. Rev.* 31 (1928) 66
- [10] R. H. Fowler, L. W. Nordheim *Proc. Soc. London A* 119 (1928) 173
- [11] L. W. Nordheim *Proc. Soc. London A* 121 (1928) 626
- [12] R. A. Millikan, C. C. Lauritsen *Phys. Rev.* 33 (1929) 598
- [13] V. Houston *Phys. Rev.* 33 (1929) 361
- [14] A. J. Ahearn *Phys. Rev.* 44 (1933) 277
- [15] E. L. Murphy, R. H. Good Jr. *Phys. Rev.* 102 (1956) 1464

- [16] E. W. Muller *Z. Physik* 106 (1937) 541
- [17] E. W. Muller *Naturwiss.* (1941) 533
- [18] E. W. Muller *Z. Physik* 131 (1951) 136
- [19] R. Gomer "Field Emission and Field Ionization" Harvard University Press, Cambridge Massachussets 1961
- [20] L. I. Schiff "Quantum mechanics" 3^oEd. McGraw-Hill International Editions 1968
- [21] A. Modinos " Field, thermionic and secondary emission spectroscopy" Plenum Publishing Corporating, N. Y. 2001
- [22] E. L. Murphy, R. H. Good *Phys. Rev.* 102 (1956) 1464
- [23] R. Forbes *Ultramicroscopy* 79 (1999) 11
- [24] J. W. Gadzuk, E. W. Plummer *Rev. Mod. Phys.* 43 (1973) 487
- [25] J.-M. Bonard, M. Croci, I. Arfaoui, O. Noury, D. Sarangi, A. Chatelain *Diamond and Related Materials* 11 (2002) 763
- [26] W. P. Dyke W. W. Dolan *Adv. Electron. Electron Phys.* 8 (1956) 89
- [27] R. G. Forbes, C. Edgcombe, U. Valdrè *Ultramicroscopy* 95 (2003) 57 (2003)
- [28] C. Edgcombe and U. Valdrè *J. Microscopy* 203 (2001) 188
- [29] L. Nilsson, O. Groening, C. Emmenegger, O. Kuüttel, E. Schaller, L. Schlapbach, H. Kind, J.-M. Bonard, K. Kern *Appl. Phys. Lett.* 76 (2000) 2071
- [30] J.-M. Bonard, N. Weiss, H. Kind, T. Stöckli, L. Forrò, K. Kern, A. Chatelain *Adv. Mater.* 13 (2001) 184
- [31] L. Nilsson, O. Groening, P. Groening, O. Kuettel, L. Schlapbach *J. Appl. Phys.* 90 (2001) 768
- [32] K. B. K. Teo, M. Chhowalla, G. A. J. Amaratunga, W. I. Milne, G. Pirio, P. Legagneux, F. Wyczisk, D. Pribat, D. G. Hasko *Appl. Phys. Lett.* 80 (2002) 2011

- [33] N. W. Ashcroft, N. D. Mermin “Solid State Physics” Harcourt College Publishers 1976, Orlando (FL), USA
- [34] O. Groening, O. M. Kuettel, C. Emmenegger, P. Groening, L. Schlapbach *J. Vac. Sci. Technol. B* 18 (2000) 665
- [35] V. V. Zhirnov, C. Lizzul-Rinne, G. J. Wojak, R. C. Sanwald, J. J. Hren *J. Vac. Sci. Technol. B* 19 (2001) 87
- [36] F. M. Charbonnier, E. E. Martin *J. Appl. Phys.* 33 (1962) 1897
- [37] C. A. Spindt, I. Brodie, L. Humphrey, E. R. Westberg *J. Appl. Phys.* 47 (1976) 5248
- [38] R. G. Forbes *J. Vac. Sci. Technol. B* 17 (1999) 526
- [39] W. Zhu, C. Bower, O. Zhou, G. Kochanski, S. Jin *Appl. Phys. Lett.* 75 (1999) 873
- [40] V. P. Mammana, O. R. Monteiro, L. R. C. Fonseca *J. Vac. Sci. Technol. B* 22 (2004) 715
- [41] L. W. Swanson, L. C. Crouser *Surf. Sci.* 23 (1970) 1
- [42] P. Vincent “Synthèse, caractérisation et étude des propriétés d’émission de champ de nanotubes de carbone” PhD thesis présentée devant l’Université Claude Bernard-Lyon 1 soutenue le 20 Septembre 2002
- [43] W. P. Dyke, W. W. Dolan *Adv. Elect. Electron Phys.* 8 (1956) 89
- [44] L. W. Swanson, A. E. Bell “Recent advances in Field Electron Microscopy of Metals” *Adv. Electron. Electron Phys.* 32 (1975) 193
- [45] M. S. Dresselhaus, G. Dresselhaus, R. Saito “Physical properties of carbon nanotubes” Imperial College Press, London (1998)
- [46] J. W. Mintmire, C. T. White in Carbon Nanotubes edited by M. Endo, S. Iijima and M. S. Dresselhaus, Pergamon, 1st edition, 1996
- [47] J. W. G. Wildoer, L. C. Venema, A. G. Rinzler, R. E. Smalley, C. Dekker *Nature* 391 (1998) 59

- [48] L. Forrò, C. Schnoinenberger, in Carbon Nanotubes edited by M. S. Dresselhaus, G. Dresselhaus, Ph. Avouris, Springer 2001
- [49] A. Thess, R. Lee, P. Nikolaev, H. J. Dai, P. Petit, J. Robert, C. H. Xu, Y. H. Lee, S. G. Kim, A. G. Rinzler, D. T. Colbert, G. E. Scuseria, D. Tomanek, J. E. Fischer, R. E. Smalley *Science* 273 (1996) 483
- [50] S. Frank, P. Poncharal, Z. L. Wang, W. A. de Heer *Science* 280 (1998) 1744
- [51] C. Schnonenberger, A. Bachtold, C. Strunk, J.-P. Salvetat, L. Forrò *Appl. Phys. A* 69 (1999) 283
- [52] W. A. de Heer, R. Martel *Physics World* June 2000, 49
- [53] J. Hone, M. Withney, C. Piskoti, A. Zettl *Phys. Rev. B* 59 (1999) 2514
- [54] W. Yi, L. Lu, Zhang Dian-Li, Z. W. Pan, S. Xie *Phys. Rev. B* 59 (1999) 9015
- [55] J.-P. Salvetat, A. J. Kulik, J.-M. Bonard, G. A. D. Briggs, T. Stoeckli, K. Metenier, S. Bonnamy, F. Beguin, N. A. Burnham, L. Forrò *Adv. Mat.* 11 (1999) 161
- [56] M.-F. Yu, B. S. Files, S. Arepalli, R. S. Ruoff, *Phys. Rev. Lett.* 84 (2000) 5552
- [57] S. Tans, A. Verschueren, C. Dekker *Nature* 49 (1998) 49
- [58] W. A. de Heer, A. Chatelain, D. Ugarte *Science* 294 (1995) 1179
- [59] H. Dai, J. H. Hafner, A. G. Rinzler, D. T. Colber, R. E. Smalley *Nature* 384 (1996) 147
- [60] K. H. An, W. S. Kim, Y. S. Park, Y. C. Choi, S. M. Lee, D. C. Chung, D. J. Bae, S. C. Lim, Y. H. Lee *Adv. Mat.* 13 (2001) 497
- [61] P. Kim, C. M. Lieber *Science* 286 (1999) 2148
- [62] D. Ugarte, A. Zettl *Science* 289 (2000) 602
- [63] K. Tsukagoshi, B. W. Alphenaar, H. Ago *Nature* 274 (1996) 1897
- [64] J. Kong *Science* 287 (2000) 622

- [65] R. Haggemuller, H. H. Gommans, A. G. Rinzler, J. E. Fischer, K. I. Winey *Chem. Phys. Lett.* 330 (2000) 219
- [66] M. L. Terranova, V. Sessa, M. Rossi *Chem. Vap. Deposition* 12 (2006) 315
- [67] Jason T. Drotar, B. Q. Wei, Y.-P. Zhao, G. Ramanath, P. M. Ajayan, T.-M. Lu, G.-C. Wang *Phys. Rev. B* 64 (2001) 125417
- [68] A. Thess *Science* 273 (1996) 483
- [69] S. Iijima, *Nature* 354 (1991) 56
- [70] J.-M. Bonard, H. Kind, T. Stockli, L.-O. Nilsson *Solid-State Electronics* 45 (2001) 893
- [71] Y. Cheng, O. Zhou, *C. R. Physique* 4 (2003) 1021
- [72] Bo Gao, Z. Guozhen, Z. Yue, Qi Qiu, Y. Cheng, Hideo Shimoda, Les Fleming, O. Zhou *Adv. Mat.* 13 (2001) 1770
- [73] J.-M. Bonard, J.-P. Salvetat, T. Stoeckli, L. Forrò, A. Chatelain *Appl. Phys. A* 69 (1999) 245
- [74] V. Semet, Vu Thien Binh, P. Vincent, G. Guillot, K. B. K. Teo, M. Chhowalla, G. A. J. Amaratunga, W. I. Milne, P. Legagneux, D. Pribat *Appl. Phys. Lett.* 81 (2002) 343
- [75] P. G. Collins, A. Zettl *Phys. Rev. B* 55 (1997) 9391
- [76] I. S. Altman, P. V. Pikhitsa, M. Choi *Appl. Phys. Lett.* 84 (2004) 1126
- [77] K. A. Dean, B. R. Chalamala *Appl. Phys. Lett.* 76 (2000) 375
- [78] S. T. Purcell, P. Vincent, C. Journet, Vu Thien Binh *Phys. Rev. Lett.* 88 (2002) 105502
- [79] Y. Wei, C. Xie, K. A. Dean, B. Coli *Appl. Phys. Lett.* 79 (2001) 4527
- [80] Y. C. Kim, K. H. Son, Y. M. Cho, E. H. Yoo *Appl. Phys. Lett.* 84 (2004) 5350
- [81] S. T. Purcell, private communication
- [82] J.-M. Bonard, N. Weiss, H. Kind, T. Stoeckli, L. Forrò, K. Kern, A. Chatelain *Adv. Mat.* 13 (2001) 184
- [83] K. A. Dean, B. Chalamala *Appl. Phys. Lett.* 75 (1999) 3017

- [84] D.-S. Chung, S. Park, H. Lee, J. Choi, S. Cha, J. Kim, J. Jang, K. Min, S. Cho, M. Yoon *Appl. Phys. Lett.* 80 (2002) 4045
- [85] M. Croci, I. Arfaoui, T. Stoeckli, A. Chatelain, J.-M. Bonard *Microelectronic Journal* 35 (2004) 329
- [86] N. de Jonge, Y. Lamy, K. Schoots, T. H. Oosterkamp *Nature* 420 (2002) 393
- [87] G. Pirio, P. Legagneux, D. Pribat, K. B. K. Teo, M. Chhowalla, G. A. J. Amaratunga, W. Milne *Nanotechnology* 13 (2002) 1
- [88] M. Guillorn, M. Hale, V. Merkulov, M. Simpson, G. Eres, H. Cui, A. Puret-zky, D. Geohegan *Appl. Phys. Lett.* 81 (2002) 2860
- [89] C. Dong, G. Myneni *Appl. Phys. Lett.* 84 (2004) 5443
- [90] R. Rose, W. Simendinger, C. Debbault, H. Shimoda, L. Fleming, B. Stoner, O. Zhou *Appl. Phys. Lett.* 76 (2000) 1668
- [91] J. B. Cui, J. Ristein, L. Ley *Phys. Rev. Lett.* 81 (1998) 429
- [92] F. J. V. Himpel, J. A. V. Knapp, J. A. van Vechten, D. E. Eastman, *Phys. Rev. B* 20 (1979) 624
- [93] J. B. Cui, M. Stammer, J. Ristein, L. Ley *J. Appl. Phys.* 88 (2000) 3667
- [94] W. Zhu, G. P. Kochanski, S. Jin *Science* 282 (1998) 1471
- [95] M. W. Geis, N. N. Efremov, K. E. Khron, J. C. Twichell, T. M. Lyszczarz, R. Kalish *Nature* 393 (1998) 431
- [96] R. Schlessler, M. T. McClure, B. L. McCarson, Z. Sitar *J. Appl. Phys.* 82 (1997) 5764
- [97] O. Groening, L.-O. Nilsson, P. Groening, L. Schlapbach *Solid State Electron-ics* 45 (2001) 929
- [98] M. Werener, R. Locher *Rep. Prog. Phys.* 61 (1998) 1665
- [99] S. Koizumi, M. Kamo, Y. Sato, M. Mita, A. Sawabe, A. Reznick, S. Uzan-Saguy, R. Kalish *Diamond Relat. Mat.* 7 (1998) 540

- [100] S. Orlanducci “Materiali compositi e nanostrutturati a base carbonio: sintesi, caratterizzazione ed applicazioni” PhD Thesis (Dottorato in Scienze Chimiche XVI ciclo) University of Rome Tor Vergata
- [101] S. T. Purcell, private communication
- [102] J.-M. Bonard *Thin Solid Films* 501 (2006) 510
- [103] S. Botti, R. Coppola, F. Gorilleau, R. Rizk *J. Appl. Phys.* 88 (2000) 339
- [104] S. Orlanducci, F. Valentini, S. Piccirillo, M.L. Terranova, S. Botti, R. Ciardi, M. Rossi, G. Palleschi *Mat. Chem. and Phys.* 87 (2004) 1905
- [105] M. S. Dresselhaus, G. Dresselhaus, A. Jorio, A. G. SouzaFilho, R. Saito *Carbon* 40 (2002) 2043
- [106] F. Tunistra, J. L. Koenig, *J. Chem. Phys.* 53 (1970) 1126
- [107] A. C. Ferrari, J. Robertson *Phys. Rev. B* 61 (2000) 14095
- [108] M. L. Terranova, S. Piccirillo, V. Sessa, P. Sbornicchia, M. Rossi, S. Botti, D. Manno *Chem. Phys. Lett.* 324 (2000) 284
- [109] S. Orlanducci, V. Sessa, M.L. Terranova, M. Rossi, D. Manno *Chem. Phys. Lett.* 367 (2003) 109
- [110] U. Kirchner, R. Vogt, C. Natzeck, J. Goschnik *Aerosol Science* 34 (2003) 1323
- [111] K. Lombaert, S. Morel, L. Le Moyne, P. Adam, J. Tardieu, de Maleissye, J. Amoroux *Plasma Chemistry and Plasma Processing* 24 (2004) 41
- [112] S. Orlanducci, A. Fiori, E. Tamburri, V. Sessa, M. L. Terranova, M. Rossi *Cryst. Res. Technol.* 40 (2005) 928
- [113] Xiuqin Che, Seji Motojima *Carbon* 37 (1999) 1817
- [114] E. Maillard-Schaller, O. M. Kuettel, L. Diederich, L. Schlapbach, V. V. Zhirnov, P.I. Belobrov *Diamond Relat. Mater.* 8 (1999) 805
- [115] Zhirnov, V. V.; Belobrov, P. I. *Diamond Relat. Mater.* 1999, 8, 805.

- [116] M. L. Terranova, S. Orlanducci, A. Fiori, E. Tamburri, V. Sessa, M. Rossi, A. S. Barnard *Chem. Mater.* 17 (2005) 3214
- [117] S. P. Mehandru, A. B. Anderson, J. C. Angus *J. Phys. Chem.* 96 (1992) 10978
- [118] T. Suzuki, M. Yagi, K. Shibuki, M. Hasemi *Appl. Phys. Lett.* 65 (1994) 540
- [119] A. S. Barnard, M. L. Terranova, M. Rossi, *Chem. Mater.* 17 (2005) 527
- [120] L. Boyer, F. Houzè, A. Tonck, J.-L. Loubett, J. -M- Gorge, *J. Phys. D: Appl. Phys* 27 (1994) 1504
- [121] Vu Thien Binh, V. Semet, J. P. Dupin, D. Guillot, *J. Vac. Sci. Technol. B* 19 (2001) 1044
- [122] S. T. Purcell, private communication